



Alharbi, Ahmad Odah A (2024) *Properties and variations of Mg II h&k lines over the solar cycle*. PhD thesis.

<http://theses.gla.ac.uk/84263/>

Copyright and moral rights for this work are retained by the author

A copy can be downloaded for personal non-commercial research or study, without prior permission or charge

This work cannot be reproduced or quoted extensively from without first obtaining permission in writing from the author

The content must not be changed in any way or sold commercially in any format or medium without the formal permission of the author

When referring to this work, full bibliographic details including the author, title, awarding institution and date of the thesis must be given

Enlighten: Theses

<https://theses.gla.ac.uk/>
research-enlighten@glasgow.ac.uk

Properties and Variations of Mg II h&k Lines Over the Solar Cycle

Ahmad Odah A Alharbi

Submitted in fulfilment of the requirements for the
Degree of Doctor of Philosophy

Astronomy and Astrophysics Group
School of Physics and Astronomy
University of Glasgow



University
of Glasgow

September 2023

Abstract

Over the years, the study of Mg II h&k lines has transformed our approach to unraveling the intricate structures and dynamics of the solar chromosphere. Since the middle of the last century until space missions, our understanding has grown exponentially. The Interface Region Imaging Spectrograph (IRIS) spacecraft is one of these missions that provided us with data that allowed us to observe these lines. In this thesis, the focus is to investigate the temporal and spatial variations of Mg II h&k lines in the solar atmosphere. Additionally, we present a novel approach for automatically determining the positions of the outer minima in the red and blue wings, line emission peaks in the red and blue sides, and the central absorption cores in the spectroscopic observations obtained by IRIS.

In Chapter 1, we offer a brief literature review of the multifaceted aspects of the Sun's atmospheric layers. The diverse structures of the chromosphere across the quiet sun, active regions, coronal holes, and prominences and filaments are described. The narrative progresses through a historical trajectory detailing the observations and research of Mg II h&k lines, highlighting their formation, intrinsic properties, and significance as diagnostic tools for the chromosphere. The Chapter concludes with an overview of the modelling of the Mg II h&k lines.

In Chapter 2, we delve into the properties of Mg II h&k lines within the Quiet Sun at the disc centre. The emphasis is placed on comprehensive observations and data analysis, leveraging the capabilities of the Interface Region Imaging Spectrograph (IRIS). Integral to the research is the introduction of a novel algorithm for the automatic identification of Mg II h&k spectral features, which is used throughout the thesis. This algorithm is meticulously described, with insights into its prerequisites, a comparison with pre-existing methods, and an assessment of the data quality it yields using synthetic data.

In Chapter 3, we use the quiet Sun rasters at disc center spanning from 2015 to 2022 obtained from IRIS. This research delves into the automatic examination of Mg II features, unraveling both consistent correlations and temporal fluctuations within these complex line profiles. The study's driving aim is to discern the nuanced interplay among radiation temperatures, integrated intensities, line widths, and the intensities of specific spectral features, all within the solar chro-

mosphere. We aim to investigate the temporal variation of the averaged flux for all Mg II h&k (2803.53 and 2796.35 Å, respectively) features over time (the end of the 24th and the beginning of the 25th solar cycles). We seek to derive information on the spectral features of the Mg II h&k lines in the solar atmosphere. We find that the intensity in k_{2v} has a strong correlation with k_3 and k_{2r} intensities, and that the total line integrated intensity has a good correlation with feature intensities for k_{2v} , k_3 , and k_{2r} . The relationship between the line width and the intensities at k_{2v} , k_3 , and k_{2r} is inverse. We also find that the average intensities in all five spectral features of the k line at Sun centre remained roughly constant between the end of the 24th solar cycle and the beginning of the 25th solar cycle. Similarly, we find that the k/h line intensity ratio remains constant over the same time period.

In Chapter 4, we use a high-resolution, single IRIS full-Sun mosaic of the Mg II k line on February 24, 2019. The solar disc is divided into 20 concentric annuli. By averaging the pixel values within each annulus, we streamline the data, mitigate local variances and facilitate an analysis. This method results in 20 average line profiles, which form the cornerstone of our final analytical endeavors. The study shows the relationships between μ (the viewing angle on the solar disc) and various solar atmospheric properties. A robust correlation is observed between μ and properties like feature intensities of spectral features, total integrated intensities, and temperatures at the k_{1v} , and k_{2v} , coupled with the intensity ratio k_2 . All these parameters decreased as μ approached the solar limb. Conversely, parameters like line width, k_1 separation, k_2 separation, velocities at k_2 separation, and depth at k_3 exhibited an increase as the viewing angle edged towards the limb.

Chapter 5 presents the conclusions, gives a summary of our findings, and discusses possible plans for future work.

Contents

Abstract	i
Acknowledgements	x
1 Introduction	1
1.1 The Sun's Atmosphere	2
1.1.1 The Photosphere	3
1.1.2 The Chromosphere	4
1.1.3 The Transition Region	5
1.1.4 The Corona	6
1.2 The Quiet Sun	8
1.3 The Solar Chromosphere	9
1.3.1 Structure of the Solar Chromosphere in Quiet Sun Regions	10
1.3.2 Structure of the Solar Chromosphere in Active Regions	10
1.3.3 Structure of the Solar Chromosphere in Coronal Holes	11
1.3.4 Structure of the Solar Chromosphere in Prominences and Filaments	12
1.4 Mg II h&k Lines	13
1.4.1 Overview	13
1.4.2 Formation and Properties of Mg II h&k Lines	15
1.4.3 Mg II h&k Lines as Chromospheric Diagnostics	18
1.5 Modelling Mg II h&k lines	19
1.6 Previous Methods	22
1.7 Conclusions	22
2 Properties of Mg II h&k lines in the Quiet Sun	23
2.1 Formation of Mg II h&k Lines	24
2.2 Observations and Data Analysis	26
2.2.1 The Interface Region Imaging Spectrograph (IRIS)	26
2.2.2 IRIS Observations	27
2.2.3 Radiometric Calibration	30

2.2.4	Savitzky-Golay Filter	31
2.3	Algorithm for Automatic Identification of Mg II h&k Spectral Features	32
2.3.1	Description of the Algorithm	32
2.3.2	Algorithm Requirements	40
2.4	Data Quality Assessment	43
2.4.1	Applying Code to Synthetic Data	43
2.4.2	Building Synthetic Data	43
2.4.3	Assessing Code Performance on Synthetic Data	44
2.4.4	Comparison with IRIS IDL Code	50
2.5	Results: Histograms	58
2.6	Conclusion	59
3	Variation over the Solar Cycle	63
3.1	Overview of Solar Cycle and Its Influence on Chromospheric Activity	64
3.2	Analysis of Mg II h&k Line Variations over the Solar Cycle	65
3.3	Data Reduction	65
3.4	Description of the Algorithm	66
3.5	Mg II h&k Lines Diagnostics	67
3.5.1	Temperatures	68
3.5.2	Total Integrated Intensities	70
3.5.3	Cumulative Sum of the Intensity	71
3.5.4	Line Widths	72
3.5.5	Temporal Variations	74
3.6	Discussion	76
3.7	Summary and Conclusions	79
4	Mosaic Observations	80
4.1	Introduction to Centre-to-Limb Variation	81
4.1.1	Importance of Centre-to-Limb Observations	82
4.1.2	Previous Studies and Findings Methods	82
4.2	The Temperature Minimum Region of the Solar Atmosphere	83
4.3	Formation Heights of Mg II Lines for Spectral Feature k_1	84
4.4	Data	84
4.4.1	IRIS Full-Disc Mosaic	84
4.4.2	Data Selection and Data Reduction	85
4.5	Mg II k Line Profiles for 20 Annuli	85
4.6	Centre-to-Limb Variation of Mg II h&k Lines	88
4.6.1	Feature Intensities for All Spectral Features	92
4.6.2	Line Width	93

4.6.3	Total Integrated Intensities	94
4.6.4	Temperatures	95
4.6.5	Velocities	96
4.6.6	Depth k_3	97
4.7	Discussion	98
4.8	Summary and Conclusions	100
5	Conclusion	102
5.1	Conclusion	102
5.2	Perspectives	104

List of Tables

2.1	Primary characteristics of IRIS (Taken form De Pontieu et al. [2014]).	27
2.2	Turning points and non-turning points with sign.	33
2.3	Number and percentage of excluded line profiles for nine raster files	36
2.4	Table comparing various window lengths and polynomial orders	38
2.5	Comparison of relative error between the smoothing parameters (5, 0) and (9, 2)	40
2.6	Comparison of the number and percentage of excluded profiles among the synthetic profiles in Fig. 2.13.	47
2.7	Velocities among the synthetic profiles in Fig. 2.13.	48
2.8	The original seven profiles' wavelength and intensity values.	49
4.1	A compilation of the inner and outer radii (in arcseconds) for the 20 annuli . . .	88

List of Figures

1.1	Variations in temperature and density across the solar atmosphere	3
1.2	Left: A comprehensive portrayal of the entire solar disc	13
1.3	The top panel: the IRIS mosaic for the Mg II k line centre captured on October 20, 2019, with superimposed circles marking 10 equally divided areas and plotted against solar X and Y coordinates in arcseconds. The bottom panel: the Mg II k line’s reference profiles from zones a–j, where the x-axis measures the wavelength deviation ($\Delta\lambda$) in Ångströms, centered on the Mg II k line, and the y-axis displays the specific intensity in $\text{W m}^{-2}\text{sr}^{-1}\text{Å}^{-1}$. This panel visibly demonstrates a gradual decline in intensities from the central disc a to the limb j, showcasing how the Mg II k profiles’ shape changes with proximity to the disc’s centre (Gunár et al. [2021]).	16
2.1	IRIS spectrum of Mg II h&k lines at 2796 and 2803 Å at the Sun’s centre.	26
2.2	Slit-jaw image taken by IRIS (1400 Å); the dark line represents the slit position (Adapted from Zhang et al. [2019]).	28
2.3	A spectrum in Mg II h&k lines at 2803 and 2796 Å	29
2.4	Intensity maps for the Mg II h&k lines at 2803 and 2796 Å	29
2.5	Spectrum measured at discrete points (blue line with dots).	31
2.6	The k_1 and h_1 , k_2 and h_2 , and k_3 and h_3 as shown on Mg II h&k line (Gošić et al. [2018]).	33
2.7	The Mg II h&k spectra for pixel location	34
2.8	The spectra of the Mg II h&k of the pixel position	35
2.9	Mg II h line at pixel location (2, 37) using 0.4 as the first parameter and 1.45 as the second.	37
2.10	Mg II h line at pixel location (2, 37)	39
2.11	Examples of Mg II h&k lines for original and smoothed data at four different pixel locations.	41
2.12	As for Fig. 2.11 with smoothing parameters 5 and 0, respectively.	42
2.13	Seven double peak profiles panels using a nine-parameter double Gaussian model.	45
2.14	Original profiles in panels a, d and e (see Fig. 2.13) after adding noise.	46

2.15	Profiles as in Fig. 2.14 smoothing only the wings.	46
2.16	Histograms of wavelength and intensity for the h parameters.	51
2.17	As with Fig. 2.16, but for original profile (b) from Fig. 2.13.	52
2.18	As for Fig. 2.16, but for original profile (c) in Fig. 2.13.	53
2.19	As for Fig. 2.16, but for original profile (d) in Fig. 2.13.	54
2.20	As for Fig. 2.16, but for original profile (e) in Fig. 2.13.	55
2.21	As for Fig. 2.16, but for original profile (f) in Fig. 2.13.	56
2.22	As for Fig. 2.16, but for original profile (g) in Fig. 2.13.	57
2.23	Wavelength histograms for profile features of Mg II h&k lines	60
2.24	Intensity histograms for the profile features of Mg II h&k lines	61
3.1	An SDO/AIA image of the sun shows a detailed view of the sun's surface on January 11, 2022, with a highlighted blue box indicating the targeted area for the slit jaw raster image. Accompanying information includes observational details, raster data, dimension of raster, step cadence, and the FOV.	66
3.2	Scatter plots of the relationship between the temperature for k_{2v} peak intensity (K) and intensities at all spectral features ($\text{erg s}^{-1} \text{cm}^{-2} \text{\AA}^{-1} \text{sr}^{-1}$).	69
3.3	The variation of the middle chromosphere's radiation temperature for the period 2015-03-01 to 2022-09-08.	70
3.4	Scatter plots of the relationship between the total integrated intensity and the intensity of each spectral feature.	71
3.5	An example of a cumulative intensity distribution for the k line intensity.	73
3.6	A theoretical Gaussian profile	74
3.7	Scatter plots of the relationship between the line width and all spectral features in intensity.	75
3.8	The variation of intensities for all Mg II k features for the period 2015-03-01 to 2022-09-08.	77
3.9	Scatter plot of the relation between the ratio of the h and k total intensity for the period 2015-03-01 to 2022-09-08.	78
4.1	The IRIS full-disc mosaic captured on February 24, 2019	86
4.2	The IRIS full-disc mosaic obtained on February 24, 2019, divided into a set of circles	87
4.3	Averaged profiles of the Mg II k line for each of the annuli labelled 'a' to 't'	89
4.4	As Fig. 4.3.	90
4.5	Plots demonstrating how the feature intensities for all spectral features are influenced by viewing angle	93
4.6	Variation in line width across different positions on the sun's disc	94
4.7	As Fig. 4.6	95

4.8	As Fig. 4.6 for total integrated intensities.	96
4.9	As Fig. 4.6, but representing temperatures for k_{1v} , and k_{2v}	96
4.10	As in Fig. 4.6	97
4.11	As Fig. 4.6, based on the average reversal depth of the k_3 core	98

Acknowledgements

Throughout my PhD journey, which began before the COVID-19 pandemic and witnessed many challenges, I finally reached the end of the journey. My heartfelt gratitude goes to the exceptional individuals who consistently stood by me, offering support and guidance throughout this arduous journey.

First and foremost, I would like to extend my heartfelt thanks to Dr. Nicolas Labrosse. His pivotal role and continuous support have been key to my success over the past four years. His firm and compassionate guidance has been instrumental in my academic development, sharpening my arguments, and improving my academic writing. He was kind and patient with me during this long period of work, research, and investigation. So, I am very grateful to him for the contributions, guidance, and encouragement I received.

I would also like to express my thanks to all researchers in the Astronomy Department for their cooperation and for always welcoming scientific questions and inquiries. I thank Professor Lyndsay Fletcher, the second supervisor, for all the support in my journey through suggestions and evaluation.

To my fellow PhD students, I always appreciate your constant support and assistance. A very special thanks and gratitude to Aaron Peat, who helped me a lot with the coding in Python. I benefited greatly from his experience in this field. He played a big role in my understanding of how to deal with it.

I would like to extend my heartfelt thanks to my father for his unwavering support and wise counsel. Though I deeply wish my mother could be here to share in this accomplishment, I take solace in believing she is in a better place. To my little family, who shared my long journey with me, words fall short to convey my gratitude. My wife, Ebtessam, I thank you deeply for everything you have done for me. My daughter, Wreef, you have grown during this journey, learned a lot, and will keep beautiful memories. My daughter, Eleen, you were born during this journey. I hope you keep some nice memories in your little mind. My little family, this PhD is dedicated to you.

Chapter 1

Introduction

The Sun, as the closest star to the Earth, serves as a natural, comparatively accessible, laboratory for the development of understanding of the myriad complexities of stellar atmospheres more broadly across the universe. One of the most challenging and intriguing aspects of solar physics is the study of the chromosphere, the layer of the sun's atmosphere confined between the photosphere and the corona. The chromosphere is a realm of intense energy and magnetic activity, and understanding its magnetic structure and thermodynamics is thus pivotal to understanding the solar atmosphere. A significant stride in chromospheric studies has been made through the investigation of the Mg II h&k lines, which are situated at wavelengths of 2803.5 Å and 2796.4 Å, respectively (e.g., [Leenaarts et al. \[2013a,b\]](#), [Pereira et al. \[2013\]](#)), and which are among the most vital radiators in the chromosphere. They are noted for their sensitivity to various chromospheric parameters, making them instrumental to developing a deeper understanding of this solar layer.

Historically, the examination of the visible spectrum has offered a window into the chromosphere, while notable lines such as H α and Ca II H&K have been invaluable in terms of ground-based observatories gaining information on the structure and dynamics of this layer. Examining these lines has therefore offered insights into temperature distributions, magnetic fields, and other intrinsic properties of the chromosphere. However, despite advances, the comprehensive picture of the chromosphere remains mysterious.

Exploration of the Mg II h&k lines dates back to the middle of the 20th century. Some of the earliest documented measurements of these lines were accomplished by means of a rocket-borne spectrograph in a pioneering venture led by [Durand et al. \[1949\]](#). However, although this marked the beginning of such exploration, it was the work of [Lemaire and Skumanich \[1973\]](#) that truly illuminated the potential of these lines. Their groundbreaking study derived variations in the profiles of the Mg II lines that paved the way for more nuanced understandings of the chromosphere's structure. The study of these lines was further supported by various space missions over the ensuing years. The OSO-8 and Skylab missions of the 1970s were revolutionary in this regard, providing the first orbital datasets for Mg II h&k lines ([Artzner et al. \[1977\]](#); [Doschek](#)

and Feldman [1977]), which expanded the horizons of such study by offering observations free from any impediments caused by Earth's atmosphere. Another notable milestone was the Solar Maximum Mission, which made pioneering polarization measurements of the Mg line profiles, adding another layer of depth to understandings of chromospheric dynamics (Henze and Stenflo [1987]).

However, despite these advances in knowledge, measurement of the Mg II h&k lines remained sparse until the launch of the Interface Region Imaging Spectrograph (IRIS) as detailed by De Pontieu et al. [2014]. IRIS, with its enhanced observational capabilities, reinvigorated interest in these lines, offering an unparalleled dataset with the promise of access to the various enigmas of the chromosphere.

This chapter discusses the intricacies of the Sun's atmosphere, particularly the solar chromosphere structure under various conditions, to emphasise the significance of Mg II h&k lines. It then outlines the study of these from historical observations to their current role as crucial chromospheric diagnostics and the subsequent modelling based on this. In the subsequent chapter, comprehensive overviews of solar observations are then given, with a focus on the Mg II h&k lines, alongside details of the instruments used; the meticulous data analysis and calibration processes required; the foundational algorithms pivotal to the current work; and an in-depth study of these lines' properties in the Quiet Sun area found at the disc centre. Chapter 3 then investigates the variation over the solar cycle of the h and k lines at the quiet sun centre before the examination of these areas deepens in Chapter 4, which focuses on using mosaic observations to analyse centre-to-limb changes in spectral line features. The final chapter, Chapter 5, then concludes with a summary of the thesis overall and recommendations for future work.

1.1 The Sun's Atmosphere

The Sun is the star that has been most carefully studied over the centuries, yet it continues to fascinate and intrigue astronomers and physicists alike. The Sun's atmosphere, the region extending from the visible surface or photosphere to the outermost layer known as the corona, has long been the object of intense study due to its complexity and dynamic nature, and this study, also known as solar physics, has important implications for understanding the Sun's magnetic field, solar flares, coronal mass ejections, and the impact of all such phenomena on the Earth's climate and solar-driven space weather.

The Sun's atmosphere is a layered structure, with each layer exhibiting unique physical characteristics and behaviours. These layers can be broadly divided into four regions, which are the photosphere, the chromosphere, the transition region, and the corona, as shown in Figure 1.1.

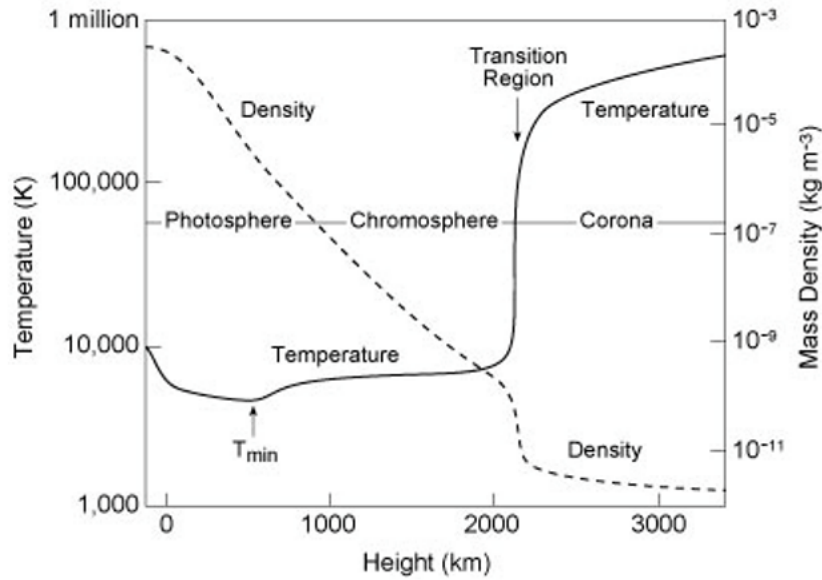


Figure 1.1: Variations in temperature and density across the solar atmosphere, sourced from a static, semi-empirical, 1D model of the quiet Sun, are adapted from [Vernazza et al. \[1981\]](#).

1.1.1 The Photosphere

The photosphere, the visible surface of the Sun, and it is a part of the sun’s atmosphere where is most of the Sun’s visible emissions, and the majority of solar radiation, originate. It thus serves as a crucial boundary in the transition from the Sun’s opaque interior to its more permeable outer layers. The base of the Sun’s photosphere is occasionally defined as being situated 100 kilometers under the level at which the optical depth at $\tau_{500} = 1$ ([Carroll and Ostlie \[2017\]](#)). The thickness of this layer is around 400 km, and its temperature is around 5,500 K ([Brekke \[2012\]](#)).

The features of the photosphere include granulation patterns, caused by convective currents that transport energy from the solar interior to the surface. The “granules” are roughly 1,000 kilometres in diameter, and each lasts for only a few minutes ([Zirin \[1988\]](#)) due to the dynamic nature of the Sun’s photospheric region. The granulation patterns develop as hot plasma rises from the solar interior, emitting light as it cools and sinks back into the Sun’s depths in a continuous cycle. The intricate movements caused by this convection and radiation generate the Sun’s observable intensity and colour variations, and these have been the topics of several key studies that have significantly advanced understanding of the photosphere: [Schwarzschild \[1975\]](#), for example, delved into the intricate nature of photospheric granulation, offering insights into its formation and dynamics.

The distinct granulation pattern that is observed on the photosphere results from the complex interactions of convection currents below its surface. As hot plasma ascends, it brightens the cell centres, while the descent of cooling plasma creates darker intergranular lanes. Within the photosphere, a high- β plasma regime prevails, wherein the gas pressure outweighs magnetic pressure, enabling fluid motions to influence the magnetic field’s configuration. Buoyant

magnetic flux tubes also ascend through the underlying convection zone, culminating in the emergence of active regions (AR) at the photosphere's surface (van Driel-Gesztelyi and Green [2015]). These dynamic AR formations are accompanied by faculae or brightened patches that are mainly observable at the limb created by reduced density due to magnetic field concentrations. These density reductions unveil the slightly deeper and hotter atmospheric layer (Foukal et al. [2006]), and when magnetic flux attains substantial strength, it manifests as magnetic pores, inhibiting convective flows to form dark, cooler patches on the photosphere. These pores, under certain conditions, can grow and converge, becoming the larger features commonly identified as sunspots, whose origins lie in the footpoints of flux tubes (van Driel-Gesztelyi and Green [2015]). Sunspots, as temporary regions of reduced temperature, are noteworthy features of the photosphere, forming dark patches that are cooler than the surrounding areas that are often linked to the Sun's magnetic field. Sunspot observations over time thus offer information on the solar activity cycle, which spreads over approximately 11 years and is associated with variations in solar magnetic fields, sunspots, and overall solar irradiance.

The photosphere represents the Sun's visible façade; as such, it plays a pivotal role in the comprehension of fundamental solar properties. Its granular dynamics, spectral features, and interaction with the solar magnetic field are therefore central to various facets of solar physics research, and the photosphere's intricate behaviours continue to captivate researchers seeking to explore its complexities to enhance the field of knowledge regarding their nearest star and its impact on the solar system.

1.1.2 The Chromosphere

The chromosphere, the region situated immediately above the photosphere, is a dynamic layer within the Sun's atmosphere. This transition zone, which is around 1000 km thick, marks the boundary between the photosphere and the outer solar atmosphere (Jess et al. [2015]), demarcated by a notable rise in temperature from photospheric levels of around 5,500 K to values exceeding 20,000 K (Priest [2014]). The reason behind this temperature rise in the upper regions of the Sun's atmosphere remains a mystery. This rise may potentially be attributable to several suggested causes. For example, it could be due to the dissipation of energy from magnetic or acoustic waves produced by photospheric convection and also through the process of Alfvén wave-induced heating or the conveyance of mechanical energy along magnetic "channels" to the outer atmosphere (Srivastava et al. [2021]). The chromosphere also plays a pivotal role in shaping the Sun's overall behaviour, thus revealing several intricate physical processes.

Nevertheless, the chromosphere is a challenging region to observe directly due to its faint emissions, and such study commonly requires specialised instruments and techniques. Spectroscopic analysis of the chromosphere can provide valuable insights into its properties, and prominent spectral lines such as the H α line at 6562.8 Å; the Ca II H&K lines at 3968.5 Å and 3933.7 Å, respectively; and the Mg II h&k resonance lines at 2803.5 Å and 2796.4 Å, re-

spectively, serve as crucial diagnostic tools in investigations of the chromosphere's temperature, density, and magnetic field characteristics. Such lines' sensitivity to temperature stratification allow researchers to study the dynamics within the chromosphere, alongside various additional phenomena. The chromosphere's relatively low density means that local thermodynamic equilibrium (LTE) does not always apply there, making it an exception. LTE assumes that the local properties of a gas determine the population of atomic energy levels and the radiation field. In this model, the population of energy levels follows the Boltzmann distribution, and the radiation field is described by Planck's law, both of which are typical for a system in thermal equilibrium. The chromosphere is an exception, however, as its relatively low density leads to departures from the conditions required for LTE. The less frequent interactions between particles and photons in such low-density areas, makes the assumption of LTE less applicable. This decrease in interactions means that the radiation field does not significantly affect the population of atoms, which considerably simplifies calculations. Consequently, the chromosphere exhibits distinct and complex characteristics that are not fully explained by simple LTE assumptions. This necessitates the consideration of non-local thermodynamic equilibrium (non-LTE) processes. Within the resulting non-LTE framework, atomic level population densities can deviate from the conventional Saha-Boltzmann LTE descriptions (Mihalas [1978]).

The chromosphere is also the region in which prominences and filaments come into play, significant solar phenomena. Prominences, characterised by their substantial mass and density, stretch above the solar surface, often forming loops or arcs. When observed on the solar disc, they manifest as dark features, referred to as filaments. The study of prominences and filaments thus reveals the important role of magnetic fields in structuring and supporting complex structures (Labrosse et al. [2010]).

The chromosphere, as an intermediary layer between the photosphere and the corona, offers crucial information about the Sun's dynamic processes. Spectroscopic analysis of key lines and the study of spicules, prominences, filaments, and eruptive events all contribute to developing understanding of the chromosphere's complex behaviours and their significant roles in the Sun's overall activity.

1.1.3 The Transition Region

The transition region, situated between the chromosphere and the corona, is of interest to solar physicists due to its dramatic temperature increase over a relatively small spatial scale. While the photosphere and chromosphere have temperatures in the thousands of degrees kelvin, this thin region of about 200 km sees the temperature rise very quickly to 10^6 K (Shapiro et al. [2019]). This abrupt temperature rise has puzzled researchers for decades, with many theories being generated in an attempt to explain the underlying mechanisms of such an increase. One of the leading theories suggests that the energy responsible for the temperature increase is derived from magnetic reconnection, a process whereby magnetic field lines reconfigure and release

energy. These reconnections occur due to the complex and intertwined magnetic fields that characterise the transition region, and they release energy in the form of heat and kinetic energy, potentially driving the observed temperature surge. However, the intricate interplay of magnetic fields, plasma flows, and energy release mechanisms in this region mean that deciphering the exact nature of the process presents a formidable challenge (Brooks et al. [2011]).

Observations of the transition region primarily rely on spectroscopic analysis of the spectral lines emitted by ionised elements at specific wavelengths, as the formation of these spectral lines is intricately tied to the physical conditions prevailing in the region. The high-resolution capabilities of modern solar telescopes such as the Interface Region Imaging Spectrograph (IRIS) have, however, revolutionised the process of accessing details from this region (De Pontieu et al. [2014]).

1.1.4 The Corona

The solar corona has been described as one of the most captivating mysteries in solar physics. The corona exhibits extreme temperatures that defy conventional expectations, with a temperature range of between 10^6 and 2×10^6 K, as well as very low density (Brekke [2012]). While the photosphere and chromosphere register at thousands of degrees, the corona's temperatures soar to several million degrees, creating a paradoxical phenomenon known as the solar corona heating problem.

The corona's extreme heat has intrigued scientists for decades, sparking a multitude of hypotheses around the energy source responsible for the remarkable temperature increase. Some of the most popular theories are magnetic reconnection and wave heating. Magnetic reconnection is when magnetic fields change shape and release energy, which causes intense heating events. Wave heating is when different types of waves travel through the solar atmosphere and deposit energy as heat when they reach the corona (Cranmer and van Ballegooijen [2005]). The Parker Solar Probe Mission's explanation is gaining increasing credibility. According to them, coronal heating in the Sun's atmosphere can be attributed to two primary mechanisms involving magnetohydrodynamic (MHD) turbulence. The first mechanism involves the reflection and nonlinear interaction of Alfvén waves propagating outwardly. The second mechanism is related to the dissipation of quasi-2D turbulence, which originates from the magnetic carpet. The potential impact of and interplay between such mechanisms remains the subject of ongoing investigation, however (Zank et al. [2021]).

Observing the corona is an intricate endeavour due to its faint nature and its proximity to the intensely bright photosphere. Total solar eclipses provide rare opportunities to witness the corona clearly as it shines through the temporary darkness; however, the infrequent nature of such occurrences renders this observation method impractical for the majority of visible light corona studies. Recently, advances in solar telescopes and instruments have facilitated corona observations outside of eclipse events, however. The Atmospheric Imaging Assembly (AIA) on

the Solar Dynamics Observatory (SDO) (Lemen et al. [2012]) and the COR-1 and COR-2 coronagraphs on the Solar and Heliospheric Observatory (SOHO) (Thompson and Reginald [2008]) have thus revolutionised understanding of the corona's intricate structure and complex dynamics. AIA and other similar instruments observe the Sun's corona by using narrow band filters that isolate specific wavelengths of light emitted by highly ionised elements in the chromosphere and corona, excluding the brighter light from the Sun's photosphere (Lemen et al. [2012]). Also, there is the observational tool for this area is called a coronagraph. This specialised instrument can be used in solar observations to block out the intense light from the solar disk, allowing observation of the fainter outer regions of the solar atmosphere, such as the corona. This instrument is thus essential for observing the corona in the visible part of the spectrum under normal circumstances. It typically consists of an occulting disk or mask placed in the optical path of a telescope to block direct light from the Sun's photosphere, enabling the observation of the extended and dimmer structures of the solar corona (Brueckner et al. [1995]).

The corona is characterised by several distinct features such as coronal loops, prominences, and coronal mass ejections (CMEs). Coronal loops, often seen in UV and X-ray wavelengths, are magnetic structures that arch gracefully over the solar surface and trace the magnetic field lines of the corona, offering insights into the intricate magnetic topology of the region. Prominences, known as filaments when seen against the solar disk, are cooler and denser plasma trails suspended in the corona's magnetic fields, and these structures provide a tantalizing glimpse into the dynamic balance between magnetic forces and gravity. In contrast, coronal mass ejections, which are violent eruptions of plasma and magnetic fields into space, are amongst the most explosive events in the solar atmosphere, and these phenomena can lead to space weather effects when they interact with Earth's magnetosphere (Webb and Howard [2012]).

Understanding the corona is therefore not only a key aim for solar physics but also of practical significance for space weather prediction and the development of technological infrastructure. Coronal mass ejections, solar flares, and other coronal events all influence the Earth's magnetosphere, potentially disrupting communication systems, navigation, and power grids, making deciphering the mechanisms that drive coronal heating and influence coronal dynamics of paramount importance (Gopalswamy [2006]). The solar corona nevertheless remains an enigma despite the interest of solar physicists, though its extreme temperatures, intricate structures, and dynamic behaviours have inspired numerous hypotheses. Advancements in observational techniques and the development of sophisticated instruments have enabled the beginnings of a deeper understanding of the corona's properties and role in influencing space weather. However, there is still much to uncover in order to fully comprehend the Sun's influence on the rest of the solar system.

1.2 The Quiet Sun

The study of the Sun is often focused on its active manifestations, such as sunspots, flares, and coronal mass ejections (CMEs), rather than those events that occur in quiet Sun regions. This is reflected in the fact that there is a loose definition which is that a quiet sun region is where magnetic fields are weak, and thus its characterisation tends to differ across studies based on their specific requirements. For example, the quiet Sun (QS) is denoted as those regions with no polarisation signal in their synoptic magnetograms (Sánchez Almeida [2004]), which suggests that while these regions have magnetic fields, these are too weak or disorganised for easy detection through regular means. In such cases, the QS is thus composed of all regions with network fields (NE) and internetwork fields (IN) over the entire solar surface.

NE are commonly seen in the boundaries and the vertices of the supergranule cells (Wang [1988]). NE patches are the QS's most prominent structures under polarised light, and these last for between hours to days, with a total flux over the surface of the Sun of 10^{23} to 10^{24} Mx (Gošić et al. [2014]). While the shapes of the field elements change continuously, they typically maintain recognisable coherence over a day of observation (Zirin [1985]). The magnetic flux of network elements varies between 2×10^{18} and 3×10^{19} Mx: some of these move along the boundary of the supergrain at speeds of 0.1 km/s in a process known as simple movement, while others undergo marked changes over several hours, whether separating, combining with field fragments of the same polarity, or cancelling out with field elements of the opposite polarity (Wang [1988]).

Livingston and Harvey [1975] were the first to discover internetwork fields using the 512-channel magnetograph at Kitt Peak. IN fields consist of elements of mixed polarities inside the network that appear as small, isolated features with a total flux of around 10^{16} to 10^{18} Mx. These appear continuously within supergranular cells and move toward the NE, though their average lifetimes are less than ten minutes, which means that many of them never exit the IN. Some do, however, remain active long enough to reach the NE and transfer their flux there (Gošić et al. [2014]). These IN fields move at a velocity of about 0.3 km/s towards the supergranule cell boundaries (Wang [1988]).

In the quiet Sun, ephemeral regions, cancellation events, the network, and the internetwork, are all related to the magnetic flux distribution. The main source of magnetic flux in the quiet Sun has usually been considered to be the ephemeral regions. However, this is moot, as there is also a significant contribution to the flux from the internetwork. Internetwork elements interact with network patches, which in turn modifies the flux budget of the network through merging processes or cancellation events. High spatial resolution magnetograms show that internetwork magnetic elements continuously appear, emerge, disappear, and cancel over the quiet Sun surface (Gošić et al. [2014]).

1.3 The Solar Chromosphere

The solar chromosphere, which is situated above the photosphere and below the transition region, is a dynamic and complex layer of the Sun's atmosphere that exhibits distinct spectral features that offer valuable insights into various properties and behavior (Jess et al. [2015]). Among these features, the Mg II h&k lines act as key diagnostic tools (Leenaarts et al. [2013a]). The chromosphere's temperature exceeds that of the cooler photosphere by several tens of thousands of degrees Kelvin (Priest [2014]). This temperature inversion, known as the "chromospheric temperature minimum region," is a challenging phenomenon, however, due to the counterintuitive behaviour of the temperature gradient. The chromosphere is characterised by a myriad of physical processes, including the interactions of magnetic fields, shocks, and waves, however, and such complex interactions are fundamental in driving the chromosphere's dynamic behaviours and contributing to its unique emission signatures (Barczynski et al. [2018]).

The formation of the Mg II h&k lines involves several complex radiative and collisional processes. These lines are not formed in LTE due to their optically thick nature and the presence of various physical processes in the chromosphere, and thus non-LTE modelling is necessary to accurately interpret the observed line profiles and to extract valuable information about chromospheric properties. In recent years, however, the use of IRIS satellite has significantly advanced our understanding of the chromosphere and its spectral features. IRIS's high-resolution spectrographs have enabled detailed observations of the Mg II h&k lines and their associated profiles that have revealed many of the complex dynamics of chromospheric phenomena such as spicules (small, jet-like features in the solar chromosphere) and fibrils (see 1.3.2). IRIS's capabilities have also allowed researchers to explore the temporal and spatial variations of these features (Leenaarts et al. [2013a] and Leenaarts et al. [2013b]).

Studies utilising the Mg II h&k lines have broader implications for space weather prediction and understanding of the Sun-Earth connection., however, as solar chromospheric activity, including flares and prominences, may influence space weather conditions close to the Earth. Investigating the chromospheric dynamics using spectral features such as Mg II h&k lines thus contributes to the ability to predict and mitigate potential space weather impacts on communication systems, satellites, and power grids (De Pontieu et al. [2014]). Building on its contribution to such understanding, study of the solar chromosphere appears to be a vital step in the quest to decode solar phenomena. This critical transitional layer, sandwiched between the photosphere and the corona, serves as a window on the Sun's complex magnetic activity, being the point where the solar atmosphere becomes dominated more significantly by magnetic forces than gas pressure (Priest [2014]), generating an array of fascinating phenomena. From the relatively calm quiet Sun regions to the magnetic tumult of its more active regions, the chromosphere exhibits varying characteristics across a range of solar features. This study thus seeks to delve into its structure to observe the dynamic nature of its existence, which is shaped significantly by

magnetic interactions and radiation processes.

1.3.1 Structure of the Solar Chromosphere in Quiet Sun Regions

The structure of the solar chromosphere in the quiet Sun regions is a subject of significant interest in solar physics. These regions are characterised by their relatively weak magnetic fields as compared to those seen in the active regions, which makes them an ideal site for studying the fundamental properties and dynamics of the chromosphere. Understanding the structure of the quiet Sun chromosphere is also crucial for unravelling the complex interplay between magnetic fields, plasma dynamics, and energy transport in this crucial layer of the solar atmosphere.

The chromosphere's structure in the quiet Sun regions has been revealed through various observational and theoretical studies. One of the key challenges in studying the quiet Sun chromosphere, however, lies in its intricate nature, which is characterised by a variety of temperature regimes, non-LTE effects, and complex magnetic field configurations. The chromospheric temperature minimum region, for example, which is located at the top of the photosphere, represents a pivotal transition zone where the temperature undergoes a non-intuitive increase from the cooler photosphere to the higher chromospheric layers (Vernazza et al. [1981]). Recent observations of the quiet Sun chromosphere have been greatly facilitated by the development of instruments such as the IRIS satellite, and high-resolution observations of spectral lines such as $H\alpha$, Ca II H & K, and the Mg II h&k lines all provide insights into the temperature, density, and dynamics of the chromospheric plasma. These spectral lines showcase a range of behaviours, including emission, absorption, and complex line profiles, that indicate the presence of complex physical processes such as shock waves, magnetic reconnection, and chromospheric oscillations (De Pontieu et al. [2014]). Numerical simulations and theoretical models have also been developed to contribute to the understanding of the structure of the quiet Sun chromosphere, while magnetohydrodynamic (MHD) simulations have been used to capture the dynamic behavior of magnetic fields and plasma in the chromosphere, shedding light on phenomena such as spicules, fibrils, and wave propagation.

The role of magnetic fields in structuring the quiet Sun chromosphere is significant. Magnetic fields are believed to play a significant role in channelling energy and governing the temperature distributions across the different chromospheric layers, while the small-scale magnetic structures, often referred to as "magnetic elements", that are prevalent in the quiet Sun have been linked to a range of chromospheric features as well as the formation of chromospheric bright points (Solanki [2003]).

1.3.2 Structure of the Solar Chromosphere in Active Regions

Active regions are characterised by the presence of strong magnetic fields that influence the behaviour of the chromosphere. Any magnetic field interacts with plasma, generating a range

of phenomena and structures that provide insights into chromospheric dynamics. Within active regions, the chromosphere then exhibits various unique features, including fibrils, penumbral filaments, and umbral dots, all of which are directly related to underlying magnetic activity (Frank et al. [1993]; Scharmer et al. [2002]).

Fibrils, slender thread-like structures that may be visible in chromospheric images, are a hallmark of active regions. These also commonly align with the magnetic field lines, providing a visual representation of the intricate interplay between magnetic fields and plasma flows in the chromosphere (Cauzzi et al. [2008]). Penumbral filaments are elongated structures surrounding the sunspots' darker central regions, the umbrae, and these filaments are believed to be associated with convective motions and magnetic field reconfigurations within the penumbra (Schlichenmaier et al. [1998]). Umbral dots, bright structures found within the umbra of sunspots, are associated with the convective motions that carry heat from the solar interior to the surface. The interactions between magnetic fields and convective flows contribute to the formation and evolution of umbral dots, highlighting the intricate relationship between magnetic activity and chromospheric dynamics (Thomas and Weiss [2004]).

Understanding the structure of the solar chromosphere within active regions has significant implications for the study of the Sun's magnetism and energy transport processes. The interplay between magnetic fields, plasma flows, and radiative processes in active regions offers insights into the complex interactions that drive the dynamic behaviour of the solar chromosphere, and investigating these phenomena thus enhances our understanding of the Sun's magnetic activity, its influence on space weather, and the broader implications of these factors with respect to both solar and stellar physics.

1.3.3 Structure of the Solar Chromosphere in Coronal Holes

Coronal holes are intriguing regions on the Sun's surface that exhibit significantly lower emission rates and densities as compared to the surrounding areas. These regions are associated with open magnetic field lines that extend into interplanetary space, which thus allow the solar wind to escape more easily. The structure of the solar chromosphere in coronal holes therefore offers valuable insights into the interplay between magnetic fields, plasma dynamics, and the extended solar atmosphere (Cranmer [2009]).

The structure of the chromosphere in coronal holes is closely linked to examination of the underlying weaker magnetic fields and lack of strong plages or network concentrations. These characteristics contribute to reduced chromospheric heating, which in turn impacts the coronal structures above, and thus, magnetic field modelling and observations, such as those provided by the Hinode satellite (Kosugi et al. [2007]), can be used to shed light on these complex magnetic configurations and their influence on chromospheric behaviour. The structure of the solar chromosphere in coronal holes thereby provides a unique perspective on the interplay between magnetic fields, plasma dynamics, and the extended solar atmosphere, while examining the re-

duced chromospheric activity, distinct transition regions, and intricate magnetic configurations all contribute to developing understanding of the behaviours of coronal holes and their impact on the solar environment.

1.3.4 Structure of the Solar Chromosphere in Prominences and Filaments

The magnetic structures that rise above the solar surface exhibit unique characteristics that are intimately tied to the chromospheric environment. While solar prominences are typically observed as bright features above the solar limb, when they are observed on the solar disc, they appear as dark features, known as filaments, due to absorption (Mackay et al. [2010]), as shown in figure 1.2. Thus, the terms prominences and filaments refer to the same physical entities in a manner solely dependent on position. Solar prominences are clouds of comparatively cool ($\sim 10^4$ K, approximately 100 times cooler than the general corona) and dense ($\sim 10^9$ to 10^{11} cm^{-3} , about 100 times denser than the general corona) gas suspended in the solar corona at the height of 10^4 to 10^5 km above the chromosphere (Tandberg-Hanssen [1995]; Labrosse et al. [2010]). They have standard pressures of between 0.02 and 1 dyn cm^{-2} , ionisation ratios of 0.2 to 0.9, and flow velocities of approximately 5 km s^{-1} (Engvold et al. [1990]). A prominence's outer layer is referred to as the Prominence Corona Transition Region (PCTR) (Vial [2005]), and this acts as an interface between the prominence and the corona: at this point, the temperature rises from roughly 7,000 K to one million K (Parenti and Vial [2014]).

While prominences come in a variety of shapes and sizes, they can be classified into two main types: quiescent and active regions (Zirin [1988]). Quiescent prominences are long-lived, static, and varying in shape, though they tend to be much longer than they are wide. Their lifespans range from a few days to several months, implying that they can remain in place for several solar rotations. They are between 10^3 to 10^4 km thick, 10^4 to 10^5 km high, and 10^4 to 10^5 km in length. Quiescent prominences have magnetic fields of between 3 and 30 G, which are commonly weaker than the magnetic fields seen in active region prominences. Quiescent prominences located at high latitudes, within 30 degrees of the north and south poles, are often referred to as Polar Crown prominences. Active region prominences are short-lived (commonly a few days or less), and these are associated with solar flares and other violent activities (Krařkiewicz et al. [2016]), with lifetimes usually shorter than those of associated active regions (Labrosse et al. [2010]). Active region prominences are more dynamic than quiescent region prominences. CMEs and flares are usually associated with prominences of active regions that are more dynamic than quiescent prominences (Tandberg-Hanssen [1995]).

Prominences and filaments are both directly linked to the magnetic field configuration in the chromosphere. The magnetic field lines in the chromosphere play a pivotal role in supporting and stabilising these structures against gravitational forces. These magnetic fields create a magnetic cage that contains the prominence material, preventing its rapid descent back to the solar surface, which allows prominences to persist for extended periods; this process also offers valu-

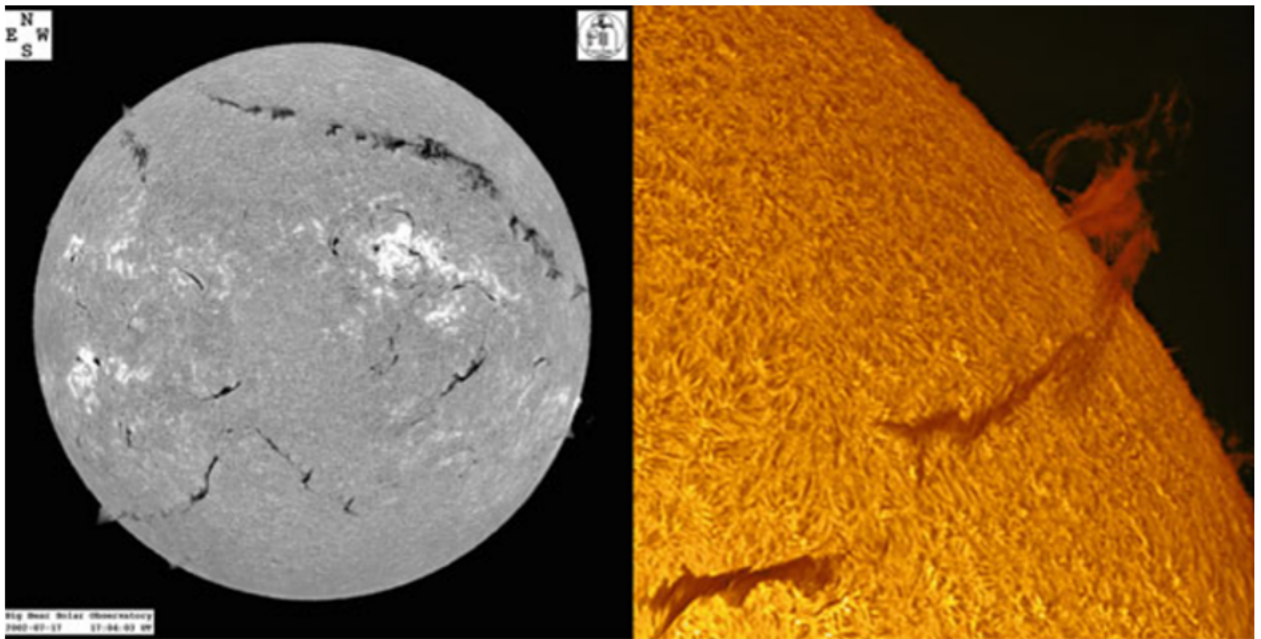


Figure 1.2: Left: A comprehensive portrayal of the entire solar disc, captured on July 17, 2002, in H-alpha, reveals a diverse array of filaments distributed across distinct regions of the disc. Right: Image acquired on November 25, 2011 (also in H-alpha) and offering a simultaneous visualisation of filaments situated on the solar disc and prominences positioned above the solar limb, Figure taken from [Engvold \[2015\]](#).

able insights into the dynamics of the chromosphere ([Labrosse et al. \[2010\]](#)). The role of the chromosphere becomes particularly evident in the process of filament eruption, which involves the ascent of a filament or prominence into the corona, leading to the release of large amounts of energy and matter into the solar wind. The initial trigger for such eruptions often originates in the chromosphere, where magnetic instabilities and reconnection events set the stage for eruption processes. Observations of the chromospheric environment surrounding erupting prominences can thus provide crucial insights into the physical mechanisms driving these explosive events ([Schmieder et al. \[2015\]](#)).

1.4 Mg II h&k Lines

1.4.1 Overview

In the 1970s, the Solar research focus in the scientific community gravitated toward the use of Mg II h&k lines, the ultraviolet spectral lines emanating from the Sun's chromosphere, as the sensitivity of these lines to variations in temperature, density, and velocity fields makes them useful tools for investigating a range of solar activities, including solar flares. The progression during this period of observational technology was critical to the understanding of Mg II h&k lines, but it was the launch of the Skylab mission by NASA in 1973 that allowed solar observa-

tion instruments to be taken into space in a manner that significantly contributed to developing understanding of the Sun's chromosphere (Dosc hek and Feldman [1977]).

An important study conducted in the 1970s by Kohl and Parkinson [1976] significantly increased understanding of the Mg II h and k lines in the solar atmosphere by developing an intricate set of new measurements of these lines with uncertainties ranging from -20 to +12 percent, an unprecedented level of precision at the time. This bolstered the robustness of the general understanding of these spectral lines, based on detailed observations of the Mg II doublet in quiet solar regions, including a focus both at the centre of the solar disc and near the limb. These valuable measurements thus not only created avenues for accurate modelling of these phenomena but also facilitated crucial comparisons with Mg II h and k observations from other regions and stellar bodies. After conducting an examination of the wavelengths and spectral intensities of the inflection points in the Mg II h and k profiles, Kohl and Parkinson [1976] also discovered that their results slightly exceeded the values given by Milkey and Mihalas [1974]. Despite these variations, the researchers suggested that their work offered overall consistency in terms of data as compared with that of Lemaire and Skumanich [1973], who had created a "k reference profile" in the inaugural study to identify variations in the structure of such profiles. One intriguing discrepancy was, however, noted in the ratio between core intensity and minimum intensity, which created a fascinating question for further investigation. Kohl and Parkinson [1976] thus became one of the most important studies in the field, contributing substantially to current comprehension of solar atmospheric processes and stellar characteristics.

In 1980, NASA launched the Solar Maximum Mission (SMM) to investigate the Sun during periods of high solar activity, such as solar flares (Strong et al. [1984]). While the SMM focused mostly on X-ray measurements, the mission helped advance the understanding of solar activity and its effects on spectral lines.

Vernazza et al. [1981] then conducted pioneering work utilising Skylab observations of the quiet Sun in the EUV wavelength range 40 to 140 nm. The researchers were able to derive distinct chromospheric models for six observed brightness components, which revealed that substantial integrated cooling rates are attributable to various elements and lines, including the Ca II infrared-triplet and resonance lines, the Mg II resonance lines, H⁻, and L α lines. Notably, that study marked the first attempt to create a comprehensive set of models specifically for the quiet Sun, offering a groundbreaking approach to understanding this crucial solar state.

In the 2010s, Further significant advancements were made using the Interface Region Imaging Spectrograph (IRIS) mission, launched in 2013. IRIS was designed to observe the solar chromosphere and the transition region (De Pontieu et al. [2014]), where the Mg II h&k lines form. The spectrograph on IRIS did indeed facilitate detailed observations of these lines, contributing significantly to current understandings of their formation and variations. At the same time, theoretical models of the solar chromosphere have become more sophisticated, and improved computational capabilities and modelling techniques have led to more accurate simula-

tions of the dynamic nature of the solar atmosphere, including the processes contributing to the formation and variation of Mg II h&k lines (Leenaarts et al. [2013a]).

The study of the Mg II h&k lines has made significant progress with the advancement in the use of instruments like IRIS. A pivotal study by Schmit et al. [2015] utilised IRIS to explore the intricate details of the Mg II h line. Their detailed examination revealed variations in this spectral line across different areas of the solar disc, laying the groundwork for future studies by highlighting the complex nature and significance of these spectral characteristics.

Following this essential research, Gunár et al. [2021], expanded upon these findings by investigating the Mg II h&k lines' variations from the center to the limb of the solar disc, utilizing a comprehensive collection of full-Sun images from IRIS. This study provided average profiles for the Mg II h and Mg II k lines, demonstrating how these profiles change from the center to the edge of the solar disc (see, Fig. 1.3). They suggested that these profiles could be very useful as standards for radiative transfer models, which are instrumental in examining various solar phenomena like prominences and spicules in the chromosphere and corona.

Overall, study of the Mg II h&k lines has played an important role in the development of understanding of the Sun's atmosphere and the dynamics of prominences and filaments. From their first use by Menzel and colleagues in the 1940s and 1950s to more recent studies by De Pontieu et al. [2014] these lines have thus proven to be valuable tool for solar physics research.

1.4.2 Formation and Properties of Mg II h&k Lines

The Mg II lines are among the strongest lines in the Sun's spectrum. They are also stronger than the Ca II lines due to the abundance of magnesium in the Solar atmosphere. However, these lines cannot be observed from the Earth because the UV portion of the spectrum in which they emit does not reach the Earth, and astronomers must thus use platforms in space to capture their details outside the Earth's atmosphere (Pereira et al. [2015]). The formation of Mg II lines in the chromosphere is complex, and a variety of studies have been carried out to develop understanding of this complexity. One series of papers (Leenaarts et al. [2013a]; Leenaarts et al. [2013b]; Pereira et al. [2013]) focused on the use of a four-level atom to model Mg II emission characteristics. However, this this series of studies produced models of limited accuracy due to the need for detailed radiative transfer computations in 3D, including partial redistribution (PRD) effects, that were not practically possible at that time.

Complete redistribution (CRD) is an approximation that assumes that line scattering is incoherent, and that there is, therefore, no correlation between the photons absorbed and those emitted. The CRD approximation hinges on the premise that the atomic levels involved in the line transitions are disturbed by elastic collisions with other atoms to an extent sufficient to destroy any detectable coherence between the absorbed and emitted photons. One of the key features of

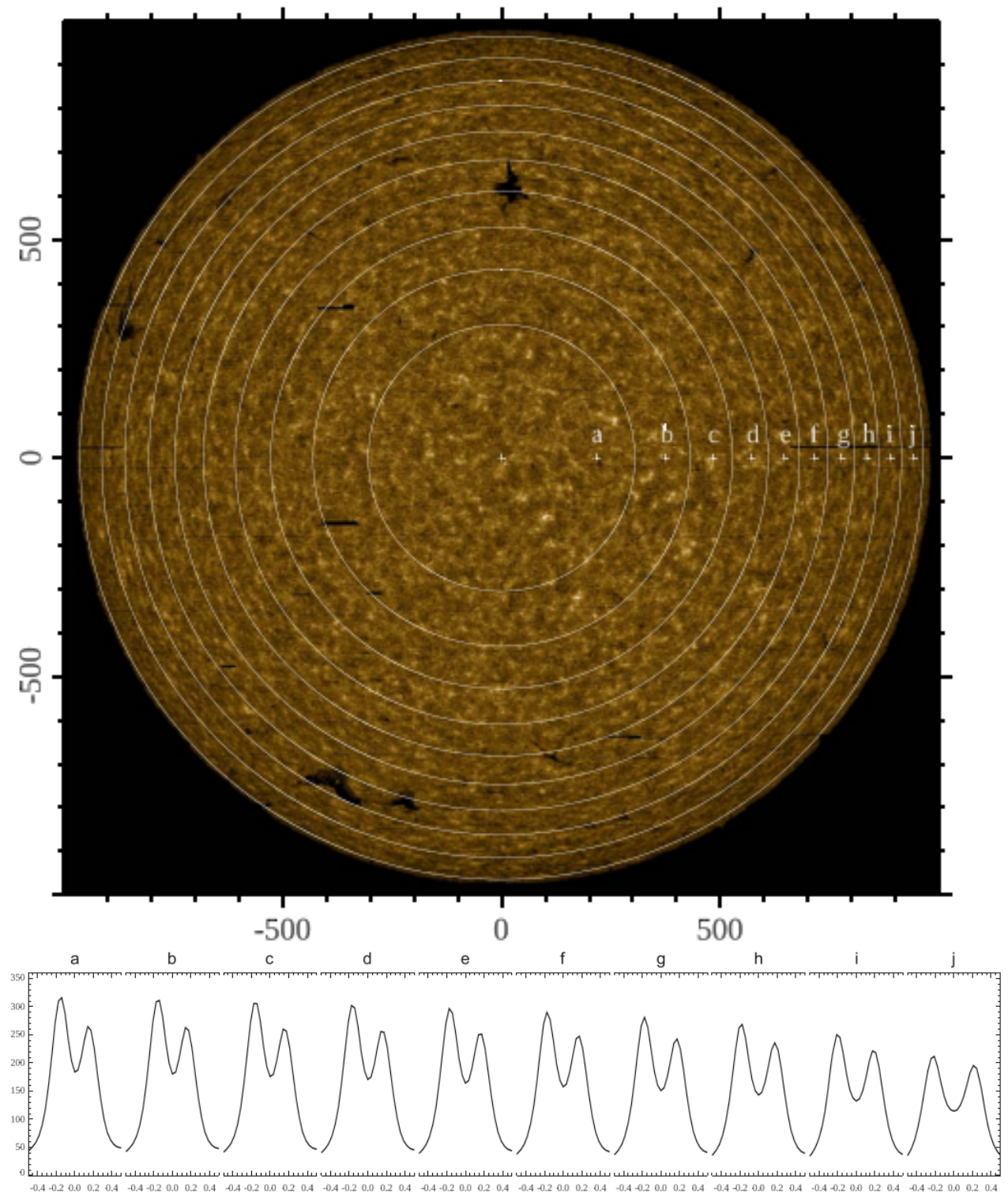


Figure 1.3: The top panel: the IRIS mosaic for the Mg II k line centre captured on October 20, 2019, with superimposed circles marking 10 equally divided areas and plotted against solar X and Y coordinates in arcseconds. The bottom panel: the Mg II k line’s reference profiles from zones a–j, where the x-axis measures the wavelength deviation ($\Delta\lambda$) in Ångströms, centered on the Mg II k line, and the y-axis displays the specific intensity in $\text{W m}^{-2} \text{sr}^{-1} \text{Å}^{-1}$. This panel visibly demonstrates a gradual decline in intensities from the central disc a to the limb j, showcasing how the Mg II k profiles’ shape changes with proximity to the disc’s centre (Gunár et al. [2021]).

CRD is that it renders the line source function constant across frequencies, greatly simplifying both the analytical and numerical approaches to solving radiative transfer issues in these lines (Sukhorukov and Leenaarts [2017]). Partial redistribution (PDR) emerged from the evolution of radiative transfer theory, which had originally assumed that the scattering in spectral lines was coherent. However, this assumption could not account for all of the observed intensities, which is what led to the CDR approximation (Sukhorukov and Leenaarts [2017]). However, as pointed out by Nagirner [1987], in time, the accumulation of observations of ever increasing precision, made it apparent that strong lines in the chromosphere do, in fact, show partially coherent scattering. This implies that the frequency correlation between incoming and outgoing photons in PDR is not arbitrary, and can be highly correlated, as seen in coherent scattering. For scattering to be partially or entirely coherent, several criteria must be met (as discussed by Hubeny and Mihalas [2014]). In stellar atmospheres with low density, like the solar chromosphere, the upper atomic level in a line transition must be only minimally influenced by elastic collisions. This limited effect is vital for maintaining the coherence of radiatively-excited sublevels throughout the level's radiative lifetime. For a line's extinction to substantially outweigh continuum extinction, the line's chemical element must be plentiful and primarily in an ionization state. The line should be characterized either as a resonance transition or involve a transition with a lower level that is metastable. Furthermore, most chromospheric lines require non-LTE descriptions, which implies that the atom population density at any specific location cannot be determined by local temperature and electron density alone. To address these challenges, inversion techniques have been developed for deducing chromosphere properties in regions with conditions where LTE doesn't apply. However, modelling these redistribution functions and conducting non-LTE inversions is very computationally intensive (Sukhorukov and Leenaarts [2017]).

Magnesium is one of the most abundant elements in the solar atmosphere, and its neutral and singly ionised states provide a variety of spectral lines of substantial diagnostic potential that stretch from the upper photosphere to the upper chromosphere, reflecting multiple variations in temperature, density, and velocity within the chromosphere. However, due to their distinct oscillator strengths, the k line appears twice as strong as the h line. Thus, while magnesium are composed of many lines, the Mg II h&k resonance doublet, at 280.27 and 279.55 nm, respectively, appear among the strongest, offering greater diagnostic value in terms of the solar spectrum. Nevertheless, these have been under-observed due to their wavelengths being in the centre of the UV range, which has precluded any ground-based observations. This issue has been significantly overcome with the launch of NASA's spacecraft Interface Region Imaging Spectrograph (IRIS), a spacecraft fitted with a high-resolution UV imaging spectrograph (<80 m Å spectral resolution) and an Mg II k slit-jaw imager (4 Å filter width) with a spatial resolution of 0.4 arcseconds.

The IRIS spectrograph uses a spectral window for composition of its images, and even slight differences in atomic structure between singly ionized calcium and magnesium thus provide

important possibilities for simultaneous sampling of temperature and velocity diagnostics. As the Ca II $3d^2D$ levels are less energetic than the $4p^2P$ upper levels of the h&k lines by about 1.3 eV, $4d^2D - 4p^2P$ triplet formation can be seen in the infrared. The Mg II $3d^2D$ levels also exist at roughly the same energy difference above the $3p^2P$ levels as above the Mg II $3s^2S$ ground state: hence, in the ultraviolet, a $3d^2D - 3p^2P$ triplet is formed, close to the h&k resonance lines, overlapping with them in terms of wavelength.

Due to their high opacity, both Mg II resonance and $3d^2D - 3p^2P$ triplet radiation can be seen to originate in the low-density chromosphere, suggesting that non-LTE radiative transfer and PRD effects are critical for line formation. Previously, researchers had modeled Mg II lines in a one-dimensional style using PRD, as documented by [Milkey and Mihalas \[1974\]](#), [Uitenbroek \[1997\]](#), and [Gouttebroze \[1989\]](#). This made interpreting the spectra from the IRIS mission quite complicated. A more effective approach involved comparing the IRIS observations with predictions from numerical simulations of radiation magnetohydrodynamics. Once this comparison was made, researchers could derive observable quantities from the known properties of the solar atmosphere, as detailed by [Leenaarts et al. \[2013a\]](#).

1.4.3 Mg II h&k Lines as Chromospheric Diagnostics

The Mg II h&k lines offer a sensitive gauge of temperature variations within the chromosphere ([Leenaarts et al. \[2013b\]](#)), as these spectral lines are primarily formed in the chromospheric layer, where the temperature exhibits a complex gradient. By scrutinising the shape, width, and intensity of the Mg II h&k lines, astronomers can thus deduce not only the temperature at various depths but also temperature changes across the chromosphere. Their sensitivity to temperature is particularly useful in terms of understanding the thermodynamic processes occurring within the chromosphere, as well as helping with the modelling of the atmospheric structure of the Sun, and hence of other stars.

Utilising Mg II h&k lines to study magnetic fields in the chromosphere also offers crucial insights into magnetic activity such as sunspots and solar flares. The polarization properties of these lines, arising from the Zeeman and Hanle effects, can be analysed in depth as a way to map the magnetic field topology within the chromosphere ([Trujillo Bueno et al. \[2011\]](#)). This is important, as understanding the magnetic field structure and its variation over time helps scientists unravel the underlying mechanisms of various magnetic phenomena, which in turn provides a deeper understanding of the magnetic behaviours of stars more generally. The Doppler shifts observed in the Mg II h&k lines offer a further powerful tool with respect to measuring velocity fields within the chromosphere. As these lines form in the chromospheric layer, any shift in wavelength can be attributed to movements within that layer, such as waves, oscillations, and bulk flows ([De Pontieu et al. \[2014\]](#)). Analysing these shifts therefore enables researchers to study the dynamics of the chromosphere in detail, offering insights into a range of phenomena such as shock waves, wave propagation, and energy transfer across different layers of the stellar

atmosphere.

Finally, the Mg II h&k lines offer a window into the chemical composition of the chromosphere. Through a detailed analysis of these lines, scientists can deduce the elemental abundance of magnesium, as well as its ionisation state within the chromospheric layer. This information is vital for constructing realistic models of the stellar atmosphere that incorporate essential details about its chemical makeup. Furthermore, such study provides an opportunity to compare the chemical compositions of different stars and to correlate these observations with theories of stellar evolution and nucleosynthesis (Asplund et al. [2009]).

1.5 Modelling Mg II h&k lines

The modelling of the Mg II h&k as doublet spectral lines, based on their importance in the study of stellar atmospheres due to their intensity and provision of information from various layers in the solar atmosphere, saw significant progress in the 1970s. Before this period, solar spectral observations had been seen as challenging due to the technological limitations, and early attempts for modelling these lines had thus focused primarily on simple static or semi-empirical models. During the 1970s, however, significant improvements in both observational capabilities, including the advent of space-based observatories, and theoretical modelling methods led to a more detailed understanding of these lines emerging. The development of more advanced radiative transfer codes, such as those created by Mihalas [1978], provided a more detailed understanding of the complex radiation-matter interactions that shape these lines, while improvements in modelling techniques in the 1970s also allowed for the inclusion of important mechanisms such as radiation damping and the quantum mechanical effect of partial redistribution, as highlighted by Shine and Linsky [1974]. Radiation damping is a process by which spectral lines are broadened, and occurs when the radiation emitted or absorbed by an atom affects the energy levels of that atom. This effect is significant in certain conditions, such as when dealing with very intense fields or in the vicinity of resonances. It is a critical factor in accurately modelling spectral lines, as it influences both their shape and intensity. It is often seen as a spurious and undesired effect, which broadens resonance lines for small flip-angle excitation pulses (Schlagnitweit et al. [2012]). Taken together, these advancements significantly improved both the predictive power and physical understanding of Mg II h&k line formation, offering a foundation for more advanced work in the 1980s and beyond.

In the 1980s, the modelling of Mg II h&k was further developed, driven both by the availability of more detailed observational data and improvements in modelling capabilities. Key to progress in this period was the launch of the Solar Maximum Mission (SMM) in 1980 alongside the International Ultraviolet Explorer (IUE) satellite, which provided unprecedented access to solar and stellar spectra, respectively, offering detailed data on Mg II h&k lines. Avrett and Loeser [1984] were among those offering significant advancement in terms of understanding

the solar atmosphere at that time. They developed a comprehensive, one-dimensional, semi-empirical model of the solar chromosphere, which took into account non-LTE effects. The introduction of multi-dimensional and time-dependent models also greatly improved understanding of the dynamic nature of the stellar atmospheres, although such models did not become prevalent until the 1990s. In addition, advancements in computing power allowed for increasingly complex radiative transfer models to be developed and used, and the introduction of models that took into account non-LTE effects helped further refine understanding of Mg II h&k line formation and its relationship to the physical conditions of the stellar atmosphere. Non-LTE describes situations where the assumption of local thermodynamic equilibrium is not met, leading to departures from equilibrium conditions in the interaction between matter and radiation. The non-LTE radiative transfer model is a computational framework that helps researchers simulate and understand how electromagnetic radiation propagates through a medium, and considers departures from local thermodynamic equilibrium. These models are essential tools for interpreting observations and gaining insights into the behaviour of light in different environments. Thus, the 1980s was a time of significant progress in both the modelling and understanding of Mg II h&k lines, fuelled by improvements in both observational data and the related theoretical models.

The 1990s saw further advancements in the modelling of Mg II h&k occur, and this played a significant role in consolidating understanding of stellar atmospheres and solar physics at that time. In this field, the decade was characterised by moves towards more complex, time-dependent, and multi-dimensional models, as seen in the work by [Carlsson and Stein \[1992\]](#), who pioneered time-dependent, non-LTE, 1-D models of the solar atmosphere that were capable of capturing the complex dynamic behavior of the chromosphere. The modelling of Mg II h&k lines was further enriched by the work of [Uitenbroek \[1997\]](#), which focused on a comparison of synthetic profiles for Mg II h&k lines formed in the solar chromosphere under the assumption of complete frequency redistribution. This work significantly enriched understanding of the Mg II h&k lines and their formation mechanisms, thereby contributing substantially to the field, yet further advances in technology later allowed for more precise and extensive observations, such as those from the SOHO spacecraft (launched in 1995), which in turn spurred further refinement and sophistication in modelling efforts. The increasingly detailed datasets generated from such missions helped validate and refine all of these models, and, overall, the 1990s was marked by advancements in both observational and modelling capabilities, which significantly contributed to the understanding of Mg II h&k lines and, by extension, the processes taking place in stellar atmospheres.

In the 2000s, the modelling of the Mg II h&k lines as crucial diagnostics of solar chromosphere conditions saw further significant advancements. This period was marked by a convergence of improved observational data and increasingly sophisticated modelling techniques as computational capabilities continued to expand.

One significant contribution to this came from the utilisation of non-LTE radiative transfer in various models, offering recognition that the conditions in the chromosphere are far from LTE. The importance of non-LTE effects in modelling solar chromospheric lines was well-understood even by the beginning of this period (Uitenbroek [2001]), but the coupling of such effects with 3D RMHD simulations was still in its infancy. During this decade, emphasis was also placed on understanding the dynamics of the chromosphere, including the role of magnetic fields, and their interplay in terms of shaping Mg II h&k lines. Researchers such as Carlsson and Stein [2002] laid down further critical groundwork in this period, underscoring the importance of developing dynamic models for chromospheric diagnostics. Thus, the first decade of the 21st century saw an expansion of the frontiers of Mg II h&k line modelling, aided by new observational datasets and sophisticated simulation capabilities.

During the 2010s, the modelling of the Mg II h&k lines has seen further significant advancements, driven by a combination of improved observational capabilities and increasingly sophisticated theoretical models. An early work in this decade was Labrosse et al. [2010], which focused on solar prominences, underscoring the significance of non-LTE modelling for capturing the intricate details of these structures. The launch of the Interface Region Imaging Spectrograph (IRIS) in 2013 was a further turning point, however, offering unparalleled high-resolution ultraviolet observations of the Sun that placed Mg II h&k lines at the heart of diagnostics. The rich datasets from IRIS have thus served as a robust testing ground for ever-more sophisticated models, enhancing understanding of the Mg II h&k lines. Among the most advanced studies so far have been those by Leenaarts et al. [2013a], Leenaarts et al. [2013b] and Pereira et al. [2013], who tapped into this resource to shed light on the formation of the Mg II h&k lines in the solar atmosphere using 3D RMHD simulations in non-LTE scenarios, emphasising the intricate interplay of magneto-hydrodynamics and radiation required to shape these lines. As the field moved into the 2020s, approaches to understanding the chromosphere thus evolved into more holistic patterns based on harmonising observations, simulations, and advanced data techniques; the use of Mg II h&k lines, however, continues to be central to all such studies. In one of the most recent contributions to this field, Gunár et al. [2022] studied the variation of periodic illumination from the Sun's surface and its affect on the Mg II h and k spectral lines emitted from structures in the chromosphere and corona. Their study focused on how variations in the incident radiation within the Mg II h&k lines influence the spectra derived from radiative transfer models in prominence-like plasmas. They found two main factors influencing the Mg II h&k spectra: shifts in the incident radiation, crucial for simulating plasma illumination from the solar disc, and the dynamics of line-of-sight within their models.

1.6 Previous Methods

Previous authors have developed various ways to study the shapes of the h and k line profiles and to determine the spectral features of the k_1/h_1 (outer minima), k_2/h_2 (outer minima), and k_3/h_3 (central absorption core) spectral features. Schmit et al. [2015] used a nine-parameter double-Gaussian model to fit a 3.4 \AA wide window centred on the Mg II h line using the MP-FIT least-squares minimisation algorithm to derive a best-fit model (BFM). Their objective was to establish a comprehensive measurement baseline and to conduct an initial analysis of the observed structure and formation of the Mg II profiles as captured by IRIS. Kerr et al. [2015] averaged the spectra along each of the 8 slit positions over time for the quiet sun area, as well as averaging the centroid wavelengths of the quiet sun pixels and shifting the IRIS images to match the AIA images as a way to analyse the potential diagnostic information in a flaring atmosphere using the Mg II h and k lines. Leenaarts et al. [2013b] used an extremum-finding algorithm, this is the method that is implemented in IDL SSW under the name `iris_get_mg_features_lev2.pro`, on a small spectral region ($-40 < \Delta v < 40 \text{ km s}^{-1}$), discarding maxima whose absolute distance to the line centre was larger than 30 km s^{-1} to determine the remaining maxima and minima in each line-core spectrum (see, Sec. 2.4.4). They thus developed a way to obtain the positions of k_2 , k_3 , h_2 , and h_3 , but could not identify the positions of k_1 , h_1 . As h_1 and k_1 are formed lower down in the atmosphere and can increase the range of altitudes over which the atmosphere can be probed, the current work is thus intended to develop a novel algorithm to also obtain the wavelengths and positions of h_1 and k_1 .

1.7 Conclusions

Over the years, the study of Mg II h&k lines has transformed our approach to unraveling the intricate structures and dynamics of the solar chromosphere. Starting from the pioneering work by Durand et al. [1949], and eventually the revolutionary data collected by space missions like OSO-8, Skylab, and IRIS, our understanding has grown exponentially. This chapter has an overview of the intricacies of the Sun's atmosphere, with a special focus on the chromosphere. We overviewed the vital role played by the Mg II h&k lines as chromospheric diagnostics, from their historical significance to their current, indispensable status in the field of solar physics. The focus is to investigate the temporal and spatial variations of Mg II h&k lines in the solar atmosphere in order to better understand the varying physical conditions where these lines are formed and to assess their impact on the chromosphere.

Chapter 2

Properties of Mg II h&k lines in the Quiet Sun at Disc Centre

The solar chromosphere performs a pivotal function in the transfer of energy and mass between the photosphere and the outer corona. Understanding the properties and variations of chromospheric features such as the Mg II h and k lines in the Quiet Sun area in the centre of the sun is thus essential to developing insight into the complex processes occurring within this region. To achieve such understanding, however, comprehensive and high-quality observations of the solar chromosphere are required, which must be obtained using advanced spacecraft and instruments specially designed to study various aspects of solar physics.

Observational tools for studying the sun have seen significant advancements since they were first developed, resulting in a plethora of modern data sources. These sources encompass both observatories located in space and those stationed on the ground, and these provide a range of data that can be used in statistical analyses of the solar atmosphere as well as providing more information about its properties in general. Each type of observatory has various advantages and disadvantages in terms of providing data, however, depending on the outcome required. For example, Earth-based astronomy imaging, while more cost effective, is constrained by the passage of light through atmosphere, which can severely distort the resulting images, while observatories positioned in space can gather data on infrared, x-ray, and gamma radiation, all which are unable to penetrate through the Earth's atmosphere without distortion.

This chapter offers a detailed examination of the spacecraft and tools utilised in this research, particularly the Interface Region Imaging Spectrograph (IRIS). Its spacecraft were specifically designed to provide high-resolution imaging and spectroscopy data related to the sun, making them invaluable for investigating both the properties and variations of the Mg II h and k lines in the Quiet Sun at both the disc centre and the centre-to-limb regions. As all the data presented in this thesis was acquired from the IRIS spacecraft, a complete overview of it is thus provided. In addition to discussing the capabilities, scientific objectives, and unique advantages of IRIS, this chapter also delves into the crucial process of data selection and processing, a phase that was

essential to guarantee the precision, dependability, and pertinence of the data employed in the study.

The specific motivation for studying the quiet Sun, particularly at the solar disc centre, lies in its pivotal role as a fundamental reference point for understanding solar behaviour and variability. First and foremost, observations at or close to the disc centre are free from projection effects, and minimise the extent of plasma intercepted by the line of sight, with respect to observations that are made closer to the limb. In addition, daily disc centre rasters acquired by IRIS provide a unique opportunity to observe the Sun with high spatial resolution over time, enabling us to track changes in solar features such as magnetic fields, granulation patterns, and chromospheric structures. This study allows for the investigation of short-term and long-term variations in solar activity and dynamics, providing valuable insights into the underlying physical processes governing the Sun's behaviour. Additionally, the Mg II lines serve as sensitive diagnostic tools for probing the chromosphere where they are formed, allowing us to investigate temperature, density, and magnetic field structure variations over time in this region. Therefore, studying the quiet Sun at the disc centre, in conjunction with Mg II line observations, offers a powerful means of unravelling the dynamic behaviour of the solar chromosphere.

2.1 Formation of Mg II h&k Lines

The Mg II lines are among the strongest lines in the Sun's spectrum. These lines cannot be observed from the Earth, however, as the full UV spectrum does not reach the Earth's surface; astronomers have thus begun to use platforms in space to capture these outside of the Earth's atmosphere (Durand et al. [1949]; Bates et al. [1969]; Doschek and Feldman [1977]; Staath and Lemaire [1995]; Morrill and Korendyke [2008]; West et al. [2011]; Pereira et al. [2015]).

The formation of Mg II lines in the chromosphere is a complex phenomena, and a variety of studies have been carried out to help understand this complexity. One such studies was the focus of a series of papers (Leenaarts et al. [2013a]; Leenaarts et al. [2013b]; Pereira et al. [2013]), that used a four-level atom to model Mg II emission characteristics. However, that work failed to produce an accurate model due to the need for detailed radiative transfer computations in 3-D, including partial redistribution (PRD) effects, that were not practically possible at the time those papers were written. More recent models do allow this, however, though in the initial models, a one-dimensional description of radiative transfer was used in an attempt to address these issues.

Magnesium is abundant in the solar atmosphere, especially between the upper photosphere and the upper chromosphere. Its neutral and singly ionised states thus provide a variety of spectral lines with substantial diagnostic potential across these layers. The spectrum of ionised magnesium is composed of many lines, with the two lines that form the Mg II h&k resonance doublet, at 2802.7 and 2795.5 Å, respectively, being among the strongest, and thus offering significant diagnostic value to the solar spectrum examinations. However, these lines are under-

observed due to their wavelengths lying in the centre of the UV range, which precludes ground-based observation. This has been significantly addressed by the launch of NASA's Interface Region Imaging Spectrograph (IRIS), a spacecraft fitted with a high-resolution UV imaging spectrograph (<80 m Å spectral resolution) and an Mg II k slit-jaw imager (4 Å filter width) with a spatial resolution of 0.4 arcseconds, however (De Pontieu et al. [2014]).

Magnesium's abundance is around 18 times that of calcium in the solar atmosphere, and its related h&k lines also form higher in the solar atmosphere than their homologous Ca II H&K lines. The abundance of magnesium is 3.98×10^{-5} , and the abundance of calcium is 2.19×10^{-6} , relative to hydrogen (Leenaarts et al. [2013a]). The Mg II resonance lines have been shown to form in a different region of the solar atmosphere than the Ca II lines, with the latter regularly lacking emission reversals or display single peak profiles. In contrast, the former always have double peak emission reversals when observed on the solar disc, except in the case of sunspots (Morrill et al. [2001]). The strong asymmetry seen between the red and blue peaks of the Ca II H&K lines, thought to be a consequence of regression in acoustic waves into shocks, is also much less pronounced in Mg h&k lines (Gouttebroze [1989]; Carlsson and Stein [1997]; Leenaarts et al. [2013a]).

The differences in atomic structure between singly ionised calcium and singly ionised magnesium lead to significant differences in temperature and velocity diagnostics. As Ca II 3d2 D energy levels are lower than the 4p2 P upper levels of h&k lines by about 1.3 eV, this leads to 4d2 D-4p2 P Ca II triplet formation in infrared. The Mg II 3d2 D levels also exist at roughly the same energy difference above the 3p2 P levels as above the Mg II 3s2 S ground state. Hence, the 3d2 D-3p2 P triplet lines are formed in the ultraviolet, close to the h&k resonance lines and overlapping with them in wavelength, as shown in Fig. 2.1.

Due to their high opacity, the radiation from the Mg II resonance and triplet lines can be seen to originate in the low-density chromosphere, where non-LTE radiative transfer and PRD effects are critical for line formation. Until recently, Mg II lines were modelled in 1-D using PRD, with the results compared to observations by Milkey and Mihalas [1974], Uitenbroek [1997], and Gouttebroze [1989]. Thus, the inversion of IRIS spectra to infer physical quantities such as temperature, velocity, and intensity is a complex process best accomplished by comparing the forward modelling of the spectra through numerical simulations of radiation magnetohydrodynamics with observations and using such simulations to extract the quantities observed from the physical quantities of the underlying atmosphere (Leenaarts et al. [2013a]).

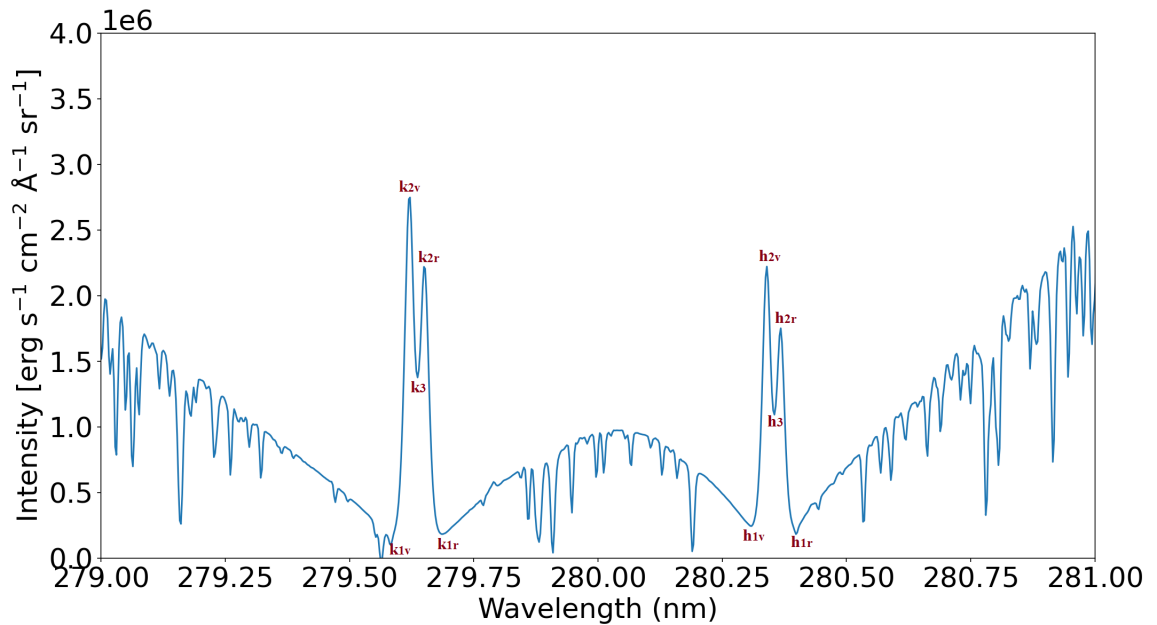


Figure 2.1: IRIS spectrum of Mg II h&k lines at 2796 and 2803 Å at the Sun’s centre (23 July 2019 04:25UT). The figure shows the location of the k_1/h_1 (outer minima), k_2/h_2 (outer minima), and k_3/h_3 (central absorption core) spectral features.

2.2 Observations and Data Analysis

2.2.1 The Interface Region Imaging Spectrograph (IRIS)

NASA launched the Interface Region Imaging Spectrograph (IRIS) spacecraft on 27 June 2013. IRIS is in a sun-synchronous orbit, and it is thus able to supply year-round solar observations except for a brief period when the Earth blocks its view of the sun between November and January. IRIS is designed to study the solar atmosphere’s interface region, which includes the chromosphere, transition region, and corona. The spacecraft is composed of a 19-cm UV telescope that feeds an imaging spectrograph with a slit-based dual-bandpass. The simultaneous spectrum and slit-jaw images (see figure 2.2) supplied by IRIS are highly sensitive to cool and hot plasma in the solar atmosphere, and spectra are taken by IRIS across three bands: the far-ultraviolet (FUV1) from 1332 to 1358 Å, the far-ultraviolet (FUV2) from 1389 to 1407 Å, and the near-ultraviolet (NUV) between 2783 and 2834 Å, thus covering the Mg II h&k in the chromosphere and the Si IV and C II lines in the transition region. IRIS is equipped with a single instrument that combines a slit-jaw imager (SJI) and a spectrograph, and the slit-jaw imager captures solar radiation across four different passbands simultaneously; these are the C II, the Si IV, the Mg II k at 2796 Å, and the Mg II h lines at 2803 Å (De Pontieu et al. [2014]). To do this, it uses spectral rasters that sample regions of up to 130×175 arcseconds across a range of spatial coordinates (see table 2.1) (De Pontieu et al. [2014]). These images provide essential contextual information for spectroscopic observations, while the spectrograph in turn records

Table 2.1: Primary characteristics of IRIS (Taken from [De Pontieu et al. \[2014\]](#)).

Parameter	Value
Primary diameter	19 cm
Effective focal length	6.895 m
Field of view	175×175 arcsec ² (SJI) 0.33×175 arcsec ² (SG – slit) 130×175 arcsec ² (SG – raster)
Spatial scale (pixel)	0.167 arcsec
Spatial resolution	0.33 arcsec (FUV) 0.4 arcsec (NUV)
Spectral scale (pixel)	12.8 mÅ (FUV) 25.6 mÅ (NUV)
Spectral resolution	26 mÅ (FUV SG) 53 mÅ (NUV SG)
Bandwidth	55 Å (FUV SJI) 4 Å (NUV SJI)
CCD detectors	Four e2v 2061×1056 pixels, thinned, back-illuminated
CCD cameras	Two 4-port readout cameras (SDO flight spares)
Detector full well	150000 electrons
Typical exposure times	0.5 to 30 seconds

spectra across several key wavelength ranges, including the Mg II h&k lines at 2803 Å and 2796 Å, respectively. The high spectral resolution and temporal cadence of these IRIS observations thus allow for detailed analysis of the Mg II h&k lines, which is an essential feature of detailed study of the solar chromosphere.

Overall, IRIS is a powerful tool for detailed investigation of the solar chromosphere and its associated phenomena. Its high-resolution imaging and spectroscopic capabilities in particular make it an ideal instrument for the study of Mg II h&k lines, providing valuable insights into solar magnetic activity and its effects on the earth.

2.2.2 IRIS Observations

The Interface Region Imaging Spectrograph (IRIS) is a UV slit-spectrograph that also captures slit-jaw images. The slit has a width of 0.33 arcseconds and a length of 175 arcseconds, offering a spatial resolution of 0.33 arcseconds in the FUV and 0.4 arcseconds in the NUV. The output IRIS FITS files are classified into four categories, depending on the level of data post-processing, this work, however, focuses on Level 2 FITS files, as the data processing pipeline used to produce Level 2 FITS files removes damaged pixels arising from dust on the detector, performs any necessary corrections on a flat field with dark current, and calibrates the geometry and wavelength based on a resting wavelength of Ni I 2799.17 Å ([Pereira et al. \[2018\]](#)).

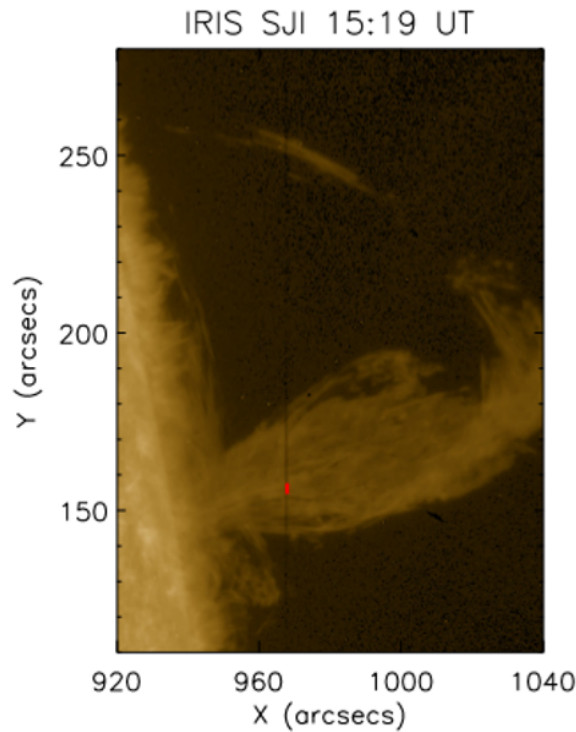


Figure 2.2: Slit-jaw image taken by IRIS (1400 Å); the dark line represents the slit position (Adapted from Zhang et al. [2019]).

The Mg II h&k line profiles in the solar chromosphere can vary significantly depending on the different solar circumstances, as they can have one or more peaks. In quiet Sun regions, these lines typically show a double-peaked emission with a central absorption feature, as shown in Fig. 2.1. During solar flares, the lines can become more intense and broaden due to the energetic events. In active regions with strong magnetic fields, the profiles can differ in width and intensity. The variability in these line profiles is influenced by the temperature, density, magnetic field strength, and dynamics of the plasma in the chromosphere, providing critical information for understanding different solar phenomena (see, Levens and Labrosse [2019] and Peat et al. [2021]).

Figure 2.3 shows a profile in the quiet sun obtained by IRIS highlighting the variation of intensity (intensities in DN, not calibrated) for both Mg II h and k lines and several other spectral lines. The Mg II h and k lines that contain five locations, two peaks, the core between these, and two other regions located in the wings of these lines, are those of most interest. Figure 2.4 shows two images that map the intensity of the Mg II k and h lines. These maps reveal a striking contrast between the internetwork—dark regions indicative of cooler, less active areas—and a surrounding network of brighter regions that signal more intense activity, possibly associated with stronger magnetic fields or localised heating. The contrast between the network and internetwork is not just visually salient, but is also indicative of significant variability in the atmospheric conditions of the Sun’s chromosphere between these two regions. The significance of these maps lies in their potential to provide insights into the physical conditions of the Sun’s

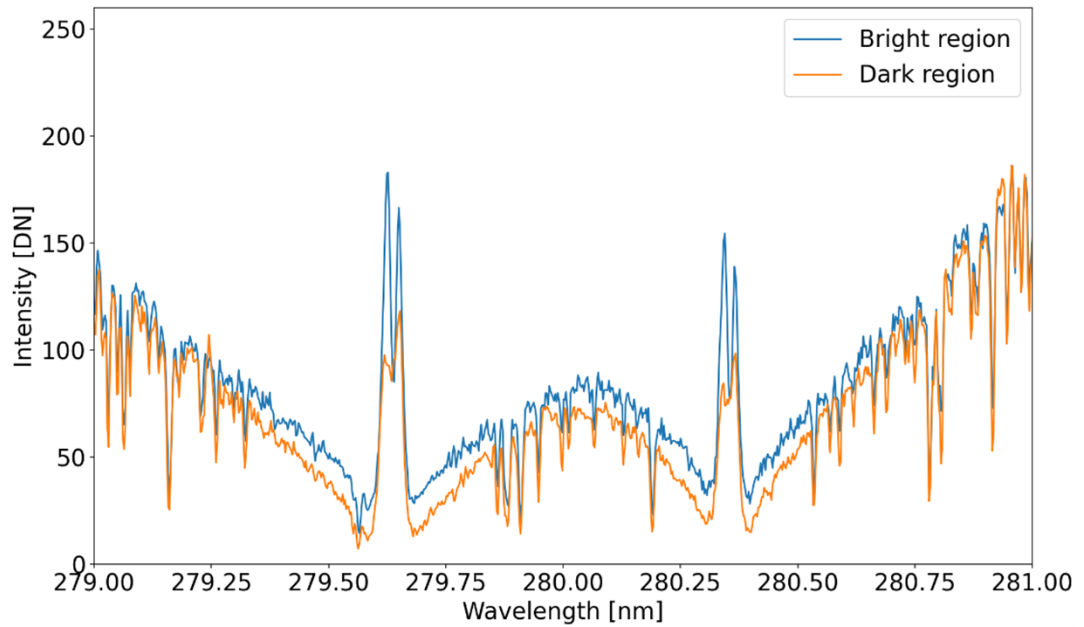


Figure 2.3: A spectrum in Mg II h&k lines at 2803 and 2796 Å taken from the sun disc centre (on 23 July 2019 at 04:25:06) by IRIS. The blue line corresponds with the network, while the orange line corresponds with the internetwork.

chromosphere, variations across different regions, and the processes that drive the dynamics of the solar atmosphere. The horizontal orientation of the two dark lines in the images, simply reflects the fact that the scanning was conducted in the y direction. The units used for the x and y axes are pixel coordinates. We downloaded all of the data between 1/3/2015 and 8/9/2022, with a particular emphasis on IRIS OBS-ID for the daily QS monitoring, which is 3882010194. These observations focus on the following four targets: QS monitoring “A1”, AR tracking “B1”, QS tracking “B2”, and the poles “C1”. Only the QS monitoring, “A1” was used for this study, however.

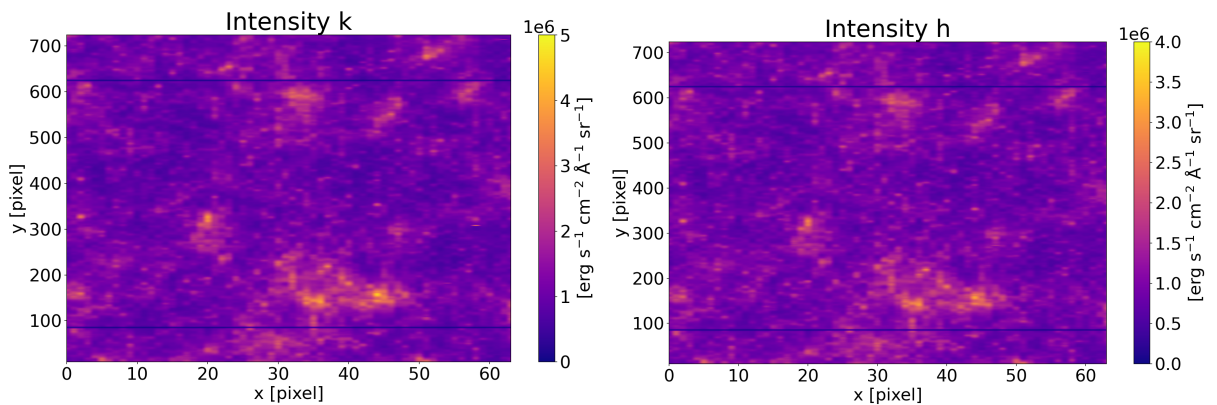


Figure 2.4: Intensity maps for the Mg II h&k lines at 2803 and 2796 Å. Image taken on 23 July 2019, from 04:25:06.

2.2.3 Radiometric Calibration

Radiometric calibration is a critical process in remote sensing and solar observation in that it helps ensure the accurate representation of the various physical properties and processes observed in the solar atmosphere. The necessary calibration process involves multiple steps to account for the instrument's response variations across its field of view and temporal changes in performance: these steps include correcting instrumental biases, subtracting dark current, applying flat-field corrections, and performing gain calibration (Lemen et al. [2012]).

IRIS radiometric calibration utilised both pre-launch and in-flight calibration methods, with the latter being ongoing. During the pre-launch calibration, the instrument's performance was characterised in a controlled laboratory environment using standard light, allowing determination of the instrument's initial response function and the establishment of a baseline for in-flight calibration (Tian et al. [2014]).

The ongoing in-flight calibration for IRIS involves monitoring the instrument's performance during its mission and regularly updating the calibration parameters (Tian et al. [2014]). IRIS thus observes stable, well-known solar or celestial targets, such as quiet sun regions, the disk centre, or solar limb to facilitate this in-flight calibration (De Pontieu et al. [2014]), a process that benefits from the instrument's design combining imaging and spectral data. The imaging data provides high-resolution spatial information, while the spectral data offers insights into the solar atmosphere's physical properties, complementary functions that allow researchers to cross-calibrate the instrument's response using multiple independent measurements.

The IRIS data are given in counts or Data Number units (DN). To convert these to a flux in physical units (e.g. $\text{erg s}^{-1} \text{sr}^{-1} \text{cm}^{-2} \text{\AA}^{-1}$) one must perform a radiometric calibration. Using the procedure detailed by Pereira et al. [2018] and Peat et al. [2021], radiometric calibration was carried out in Python for this study. The response function was obtained using the `iris_get_response.pro` function from SolarSoft (SSW). The Python version of SS-WIDL code that was written by A. Peat was used. He deconvolve the IRIS point-spread function from the data in Python using a method similar to SSW's `iris_sg_deconvolve.pro`. To convert Data Number units (DN) into a measurable flux value (in units of $\text{erg s}^{-1} \text{cm}^{-2} \text{\AA}^{-1} \text{sr}^{-1}$), the procedure employed was the 'iris get response' function specific to time (referred to as 'iris_get_response' function). When provided with the date and time of observation, this function yields the parameters required for this transformation:

$$\text{Flux} \left(\text{erg s}^{-1} \text{cm}^{-2} \text{\AA}^{-1} \text{sr}^{-1} \right) = \frac{\text{Flux(DN)}}{E_{\lambda} \cdot \text{DN2PHOT_SG}} \cdot \frac{A_{\text{eff}} \cdot \text{Pix}_{xy}}{\text{Pix}_{\lambda} \cdot t_{\text{exp}} \cdot W_{\text{slit}}} \quad (2.1)$$

where E_{λ} (in ergs) represents the energy per photon, DN2PHOT_SG denotes the photon count corresponding to each DN, Pix_{xy} (in radians) specifies the size of the spectral pixels, Pix_{λ} (in Angstroms) the size of the spectral pixels, A_{eff} (in cm^{-2}) is the effective area, t_{exp} (in seconds) refers to the exposure time and W_{slit} (in radians) measures the width of the slit used.

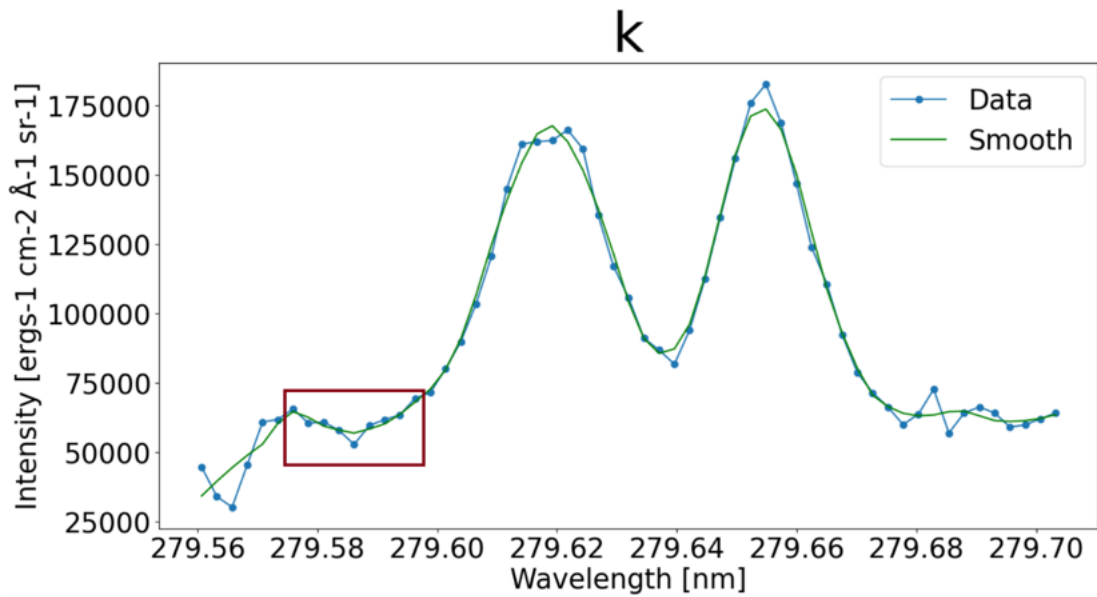


Figure 2.5: Spectrum measured at discrete points (blue line with dots). Filter window, $W_L = 9$, shown in the bottom left, illustrating the filter window's length.

Radiometric calibration was thus applied over the entire dataset of interest.

2.2.4 Savitzky-Golay Filter

Data smoothing is a very popular pre-processing step for spectral data. Smoothing is the process of applying numerical procedures to raw data to decrease noise, which is crucial when trying to identify significant spectral features that may be hidden by noise. To smooth the data and reduce noise in profiles, particularly in the wings (k_{1v} and h_{1r}), a Savitzky-Golay (SG) Filter, also known as digital smoothing polynomial filter or least-squares smoothing filter, was applied. The SG filter performs polynomial fitting to segments of data known as frames, offering a method that is particularly effective at smoothing noisy data, based on the length of the filter window. This must be a positive odd integer and the order of the polynomial used to fit the samples must be less than the window-length (Savitzky and Golay [1964]).

Figure 2.5 shows the process by which the Savitzky-Golay (SG) method, implemented through the 'savgol_filter' function from a Python package, smooths data by replacing the value at the centre of each window with a value derived from fitting a polynomial to the data within that window. This calculation occurs every nine consecutive points, with the fifth point (the middle of the window) replaced with the calculated value across all nine points. For the initial and final four points in the dataset, this package uses polynomial fit to estimate these values.

2.3 Algorithm for Automatic Identification of Mg II h&k Spectral Features

Studying the spatial and temporal variability of the Mg II h 2803.53 Å and k 2796.35 Å lines in solar observations is intended to allow the derivation of information on the spectral features of the Mg II h and k lines in the quiet sun centre. This work thus developed a tool in Python to support a novel approach to automatically determining the wavelengths and intensities of k_{1v} , k_{2v} , k_3 , k_{2r} , k_{1r} , h_{1v} , h_{2v} , h_3 , h_{2r} , and h_{1r} , in the line profiles obtained by IRIS for the quiet sun centre. To distinguish the red and blue sides of the local maxima and minima peaks, the subscript r or v is added, where subscript v refers to the blue side and r refers to the red side. Focusing on the Mg II k&k lines is important because the Mg II ions produce a number of spectral lines that can be used to make diagnostics in the solar atmosphere. The Mg II h&k lines have complicated line shapes with features that form at different heights in the solar chromosphere. In this spectral line, different photons at different wavelengths are coming from different layers; thus, we are probing different altitudes in the solar chromosphere.

2.3.1 Description of the Algorithm

The solar spectra of Mg II h&k lines all commonly show two emission peaks along with a central absorption core and surrounding local minima. These characteristics are referred to as k_{2v}/k_{2r} , k_3 , and k_{1v}/k_{1r} for the k line, with similar labelling used for the h line. An automated method was thus established to determine the positions of these spectral features in the line profiles obtained by IRIS at the quiet sun centre. At this stage of the work, only one raster was analysed, and after completing this task, this was applied to an extended data set covering the duration of the mission, to investigate temporal variations. Eventually the spatial variations over the full disc should be investigated (see Chap. 3), however, and manual feature determination is not possible due to a large number of spectra to be analysed (approximately 230×10^6 , which represents h and k lines for the whole period). An algorithm was thus created to automatically determine the positions of the k_1 and h_1 outer minima in wings, the k_2 and h_2 emission peaks, and the k_3 and h_3 central absorption cores that are labelled in Fig. 2.6 using the method for finding turning points. The algorithm determines the number of peaks in the spectrum using a set of rules, and the simple description of a typical h or k line profile thus contrasts with many of the more complex observed profiles, which exhibit several peaks. Some line profiles varied from the five extrema model (2 peaks and 3 minima); however, most line profiles exhibited a standard profile of blue and red outer minima, blue and red emission peaks, and a central minimum.

Local minima and maxima are shown in Fig. 2.7 as orange points. The data in only the wings was smoothed using the Savitzky-Golay (SG) method to reduce noise, and the window length and the polynomial order were set to nine and two, respectively. All differences in intensity

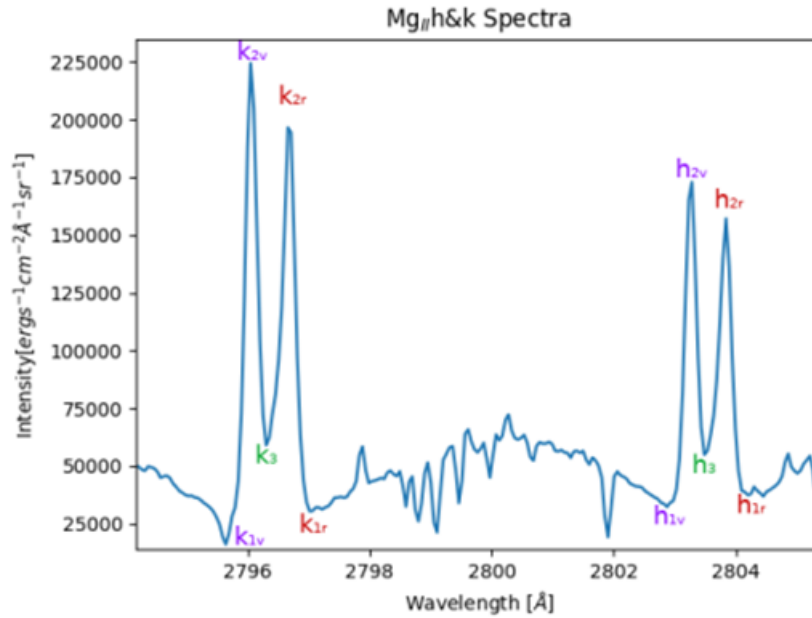


Figure 2.6: The k_1 and h_1 , k_2 and h_2 , and k_3 and h_3 as shown on Mg II h&k line (Gošić et al. [2018]).

(first derivative) between consecutive points across the line profiles were then calculated, and the sign of each value assessed. After that, the differences in sign (the second derivative) between each two consecutive points were noted in order to determine the turning points. Where a difference in the sign between two consecutive points was found to be positive, this was deemed a local minima, while where the difference in the sign was negative, a local maxima was defined. Table 2.2 summarises the turning points and non-turning points: for each minimum turning point, a positive result can be derived by taking the second difference while for the maximum turning point, a negative result occurs when taking the second difference. When the second difference for any non-turning point is tested, the result is zero, confirming its identity as a point that is not of interest to this work (To find the second difference, we assume that the values are equal, while the sign depends on the direction).

Table 2.2: Turning points and non-turning points with sign.

Signs of the first differences	Second difference result	Turning Point Type
Positive – Negative	Positive	minimum
Negative – Positive	Negative	maximum
Positive – Positive	0	Not a turning point
Negative – Negative	0	Not a turning point

As this method determines all peaks, while only five points are required for the determination of any of the h or k lines, conditions to determine the differences between valid and non-valid peaks were set. The standard deviation (sd) was thus used as a function to ensure that peaks with a difference in intensity of less than one-third of the standard deviation were excluded.

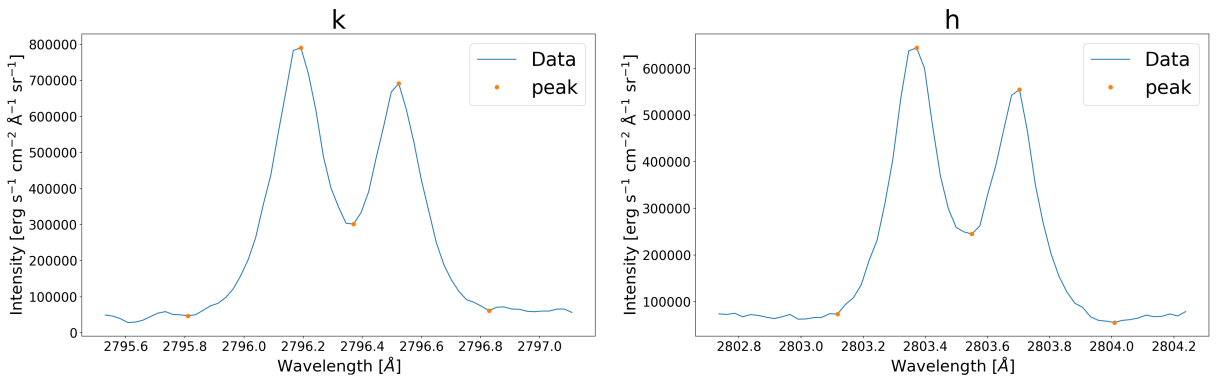


Figure 2.7: The Mg II h&k spectra for pixel location [30, 40] of these profiles are determined from Fig. 2.4, offering a conventional line profile. The left panel shows the line profile of the k line, while the right panel shows the line profile of the h line.

Finally, the line profile was divided into five regions, depending on the locations of the various features, in order to remove any excess unwanted points. Where two points or more appeared in the same region and the intensity difference between them was less than 1.45 standard deviations, the following procedure was applied:

- for the outer minima, in the blue wing we simply keep the point of greatest wavelength, while in the red wing, we keep the point at the shortest wavelength;
- In the line emission peaks, all points of lower intensity were removed;
- In the central absorption core, all points of higher intensity were removed.

Completing these processes produced the final results for line profiles. These were then stored in a standardised format to allow the algorithm to recognise the five necessary features (2 peaks and 3 minima) and their correct positions; based on this, any line profiles that still had more or fewer than five points were thus excluded.

Figure 2.7 shows a “standard” profile with well-defined features, offering an example of a spectral line plot for a single pixel in a raster of 9.1392×10^4 pixels. Due to the wide variety of profile shapes, any of these features may be absent or impossible to distinguish in other situations, however. Due to the vast number of spectra, an automatic method to reject plots with more or fewer than five features (2 peaks and 3 minima) was applied, as seen in Fig. 2.8. The number of rejected plots was 3.574×10^3 , out of 9.1392×10^4 plots, or 3.9%.

Description of Tests

Two Parameters

As explained in Sec. 2.3.1, 0.3333 and 1.45 standard deviations were applied as the first and second parameters, respectively. These parameters were selected after multiple tests across nine raster files for the period between 2014 and 2022, with optimisation based on the percentage

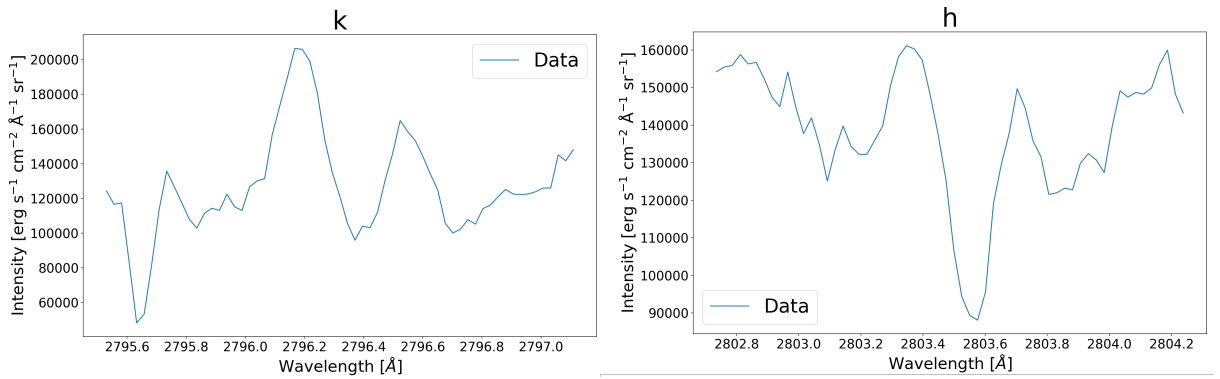


Figure 2.8: The spectra of the Mg II h&k of the pixel position [63, 15] of these profiles are determined from Fig. 2.4, offering a complex line profile. The left panel shows the line profile of the k line, while the right panel shows the line profile of the h line. These profiles are rejected

of rejected line profiles generated by changing the standard deviation value. The algorithm was altered to find the lowest percentage of excluded line profiles at the first parameter, from 0.1 to 0.5 of the standard deviation, while the second parameter was tested from 0.3333 to 1.67 sd. The lowest percentage of excluded line profiles was thus found when 0.3333 or 0.4 was used as the first parameter and 1.45 was used as the second. Table 2.3 shows the differences between the percentage of rejected line profiles across nine raster files on changing the sd value for the first parameter from 0.1 to 0.5; in each case, 1.45 was used as the second parameter. As shown, nine raster files representing the beginning of each year of the target period were selected, in addition to the basic raster file 23/07/2019, which was studied extensively in this chapter. These were the files for 01/04/2014, 01/01/2015, 02/01/2016, 01/01/2017, 01/01/2018, 01/01/2019, 01/01/2020, and 01/01/2021. The proportion of excluded profiles was very close among all selected raster files, indicating that the algorithm is consistent. At 0.3333 and 0.4, the percentage of rejections is thus the least possible. The large number of profiles excluded in the first file (iris_l2_20140401_082121) appears to be due to a defect in images taken in the early days of operation of the IRIS spacecraft.

Two criteria were used to select the best parameters: these were the number of excluded profiles and the accuracy of the positions of features. In terms of the proportion of excluded profiles, in some point files, this was lowest when one-third of the standard deviation was chosen as the first parameter, while in others, it was lowest when 0.4 of the standard deviation was chosen. Testing across multiple profiles, which is used to conduct a larger statistical study, further suggested that the value of 0.4 sd reliably determines five points for each profile, but that some of these may then not be in the correct locations.

The accuracy of the positions of features is defined by the lowest points on the curve before the emission peaks in the wings of the line (both blue and red), the point of highest intensity for emission peaks, and the point of lowest intensity for the central absorption core. Figure 2.9 illustrates an example of inaccuracy in feature positions, clarifying that the central absorption

Table 2.3: Number and the percentage of excluded line profiles for nine raster files based on changing the sd value for the first parameter from 0.1 to 0.5, with 1.45 as the second parameter.

Raster files	0.1	0.2	0.3	0.3333	0.4	0.45	0.5
iris_I2_20140401_082121	32196 (35.22%)	24409 (26.71%)	23586 (25.81%)	23517 (25.73%)	23473 (25.68%)	23509 (25.72%)	23671 (25.90%)
iris_I2_20150101_030918	11585 (12.68%)	5177 (5.66%)	4415 (4.83%)	4307 (4.71%)	4339 (4.75%)	4530 (4.96%)	4866 (5.32%)
iris_I2_20160102_035918	13542 (14.82%)	6059 (6.63%)	4851 (5.31%)	4708 (5.15%)	4724 (5.17%)	4977 (5.45%)	5490 (6.01%)
iris_I2_20170101_065518	12764 (13.97%)	5072 (5.55%)	3783 (4.14%)	3624 (3.97%)	3602 (3.94%)	3853 (4.22%)	4256 (4.66%)
iris_I2_20180101_052555	15331 (16.77%)	6559 (7.18%)	5185 (5.67%)	5002 (5.47%)	4917 (5.38%)	5185 (5.67%)	5636 (6.17%)
iris_I2_20190101_034650	12626 (13.82%)	5027 (5.50%)	3445 (3.77%)	3199 (3.50%)	3080 (3.37%)	3259 (3.57%)	3748 (4.10%)
iris_I2_20190723_042506	14240 (15.58%)	5498 (6.02%)	3969 (4.34%)	3733 (4.08%)	3736 (4.09%)	4001 (4.38%)	4526 (4.95%)
iris_I2_20200101_051202	14779 (16.17%)	5505 (6.02%)	4081 (4.47%)	3893 (4.26%)	3899 (4.27%)	4197 (4.59%)	4713 (5.16%)
iris_I2_20210101_052457	14166 (15.50%)	5595 (6.12%)	3911 (4.28%)	3637 (3.98%)	3512 (3.84%)	3767 (4.12%)	4313 (4.72%)

feature was not determined correctly: the algorithm should have chosen the point with the least intensity, which did not happen. The reason for preferring 0.3 sd for the first parameter is thus that it offers greater accuracy in terms of determining the correct locations of features in most cases, particularly where the difference between the two emission peaks and the central line absorption is larger than 0.3 sd and less than 0.4 sd.

Although these steps appear to effectively determine the spectral features of k_2/h_2 and k_3/h_3 , the algorithm did seem to encounter more difficulty in accurately determining the positions of k_{1v} and h_{1r} due to the relatively high noise at these two positions in the Mg II spectrum. Thus, the algorithm was developed further to address this limitation by smoothing the data to avoid noise across the wings of the profile.

Smoothing Data

The Savitzky-Golay (SG) method used in this work is among the best methods for data smoothing. The core idea of the SG smoothing is to select the window size and polynomial degree that best match the spectra of interest. This necessitates multiple tests to ascertain the optimal window length and polynomial order for the data. In this study, the values 9 and 2 were selected, respectively.

The optimal smoothing parameters were ascertained using two steps: 1) Calculating multiple smoothed spectra with varying SG function parameters; and 2) Calculating the relative error between the raw and smoothed data in each scenario.

- Calculating smoothed spectra with different parameters

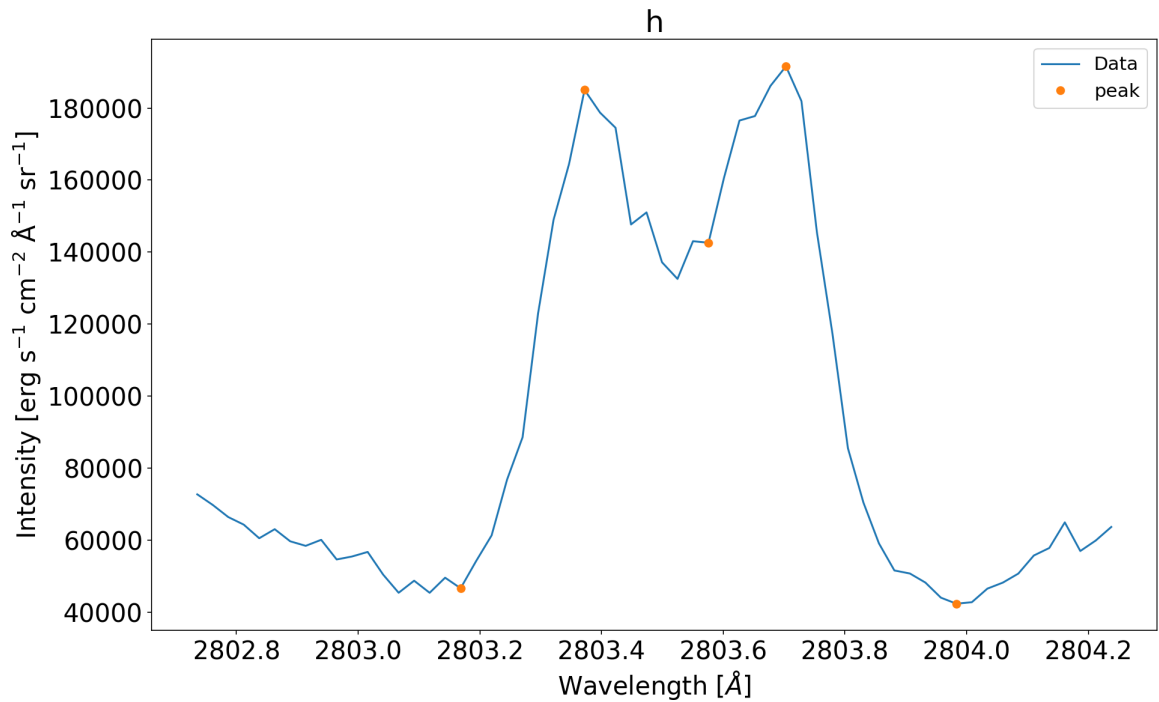


Figure 2.9: Mg II h line at pixel location [2, 37] using 0.4 as the first parameter and 1.45 as the second. This is an example of inaccurate determination of the position of h_3 .

Upon examination of the raw data, significant noise is apparent, particularly in the wings, especially on the blue side of the k line and the red side of the h line. This noise's effect is observable in the histograms of the found wavelengths for each feature, which don't align well with a Gaussian distribution for either k_{1v} or h_{1r} primarily due to their positions as outer minima, which introduce greater noise levels. The data smoothing's primary objective was to minimize the noise at these two sites, enabling the algorithm to precisely locate these points. Consequently, this would produce wavelength histograms closely matching the Gaussian distribution. Two criteria determined the optimal smoothing parameters: the number of excluded profiles and the histograms' Gaussian distribution alignment. We expect that small random factors may influence the wavelength at which k_{1v} and h_{1r} are found, and that this therefore should result in a Gaussian distribution. By varying the window width from 1 to 9 and adjusting the polynomial degree to values lower than the window width, the algorithm was assessed. Table 2.4 indicates that the best options in terms of profile exclusion and Gaussian distribution alignment were (5, 0) and (9, 2). Figure 2.10 also shows that the green line, symbolizing window length 9 and polynomial degree 2, mirrors the raw data closely. In contrast, the red line, denoting window length 5 and polynomial degree 0, is less representative of the original data.

- Relative Error

To choose between (5, 0) and (9, 2) as the optimal smoothing parameters, multiple relative error computations were executed, comparing the original data and the smoothed data for k_{2v} , k_{2r} , h_{2v} and h_{2r} features across eight random pixel sites. The calculation of the relative error

Table 2.4: Table comparing various window lengths and polynomial orders in terms of the number of excluded line profiles and whether the Gaussian distribution describes the wavelength histograms for k_{1v} and h_{1r} adequately. Original raster file obtained by IRIS on 23 July 2019, at 04:25UT. A histogram's classification as good or bad in the context of a Gaussian distribution depends on how well the data's distribution matches a normal distribution.

(Window length, Poly order)	Number of excluded profiles	The wavelength histograms for k_{1v} and h_{1r} by Gaussian distribution
(1, 0)	3594	Very bad
(3, 0)	3468	Very bad
(3, 1)	3682	Very bad
(3, 2)	3594	Very bad
(5, 0)	5313	Good
(5, 1)	10139	Very good
(5, 2)	2848	Very bad
(5, 3)	2785	Very bad
(5, 4)	3594	Very bad
(7, 0)	13555	Very bad
(7, 1)	31840	Very good
(7, 2)	3744	Bad
(7, 3)	3378	Bad
(7, 4)	2791	Very bad
(7, 5)	2774	Very bad
(7, 6)	3594	Very bad
(9, 0)	37548	Very bad
(9, 1)	64539	Very bad
(9, 2)	5304	Good
(9, 3)	4732	Good
(9, 4)	3136	Very bad
(9, 5)	2912	Very bad
(9, 6)	2850	Very bad
(9, 7)	2811	Very bad
(9, 8)	3594	Very bad

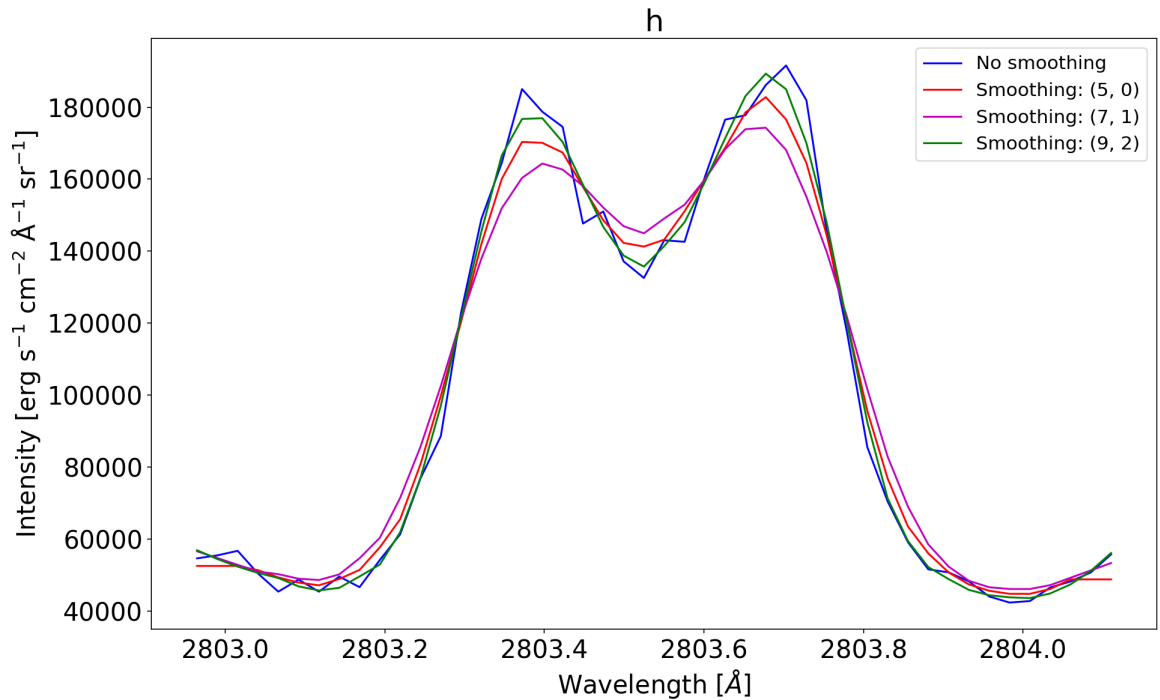


Figure 2.10: Mg II h line at pixel location [2, 37]: The blue line is the original spectrum. The red line shows mild smoothing with (5, 0). The magenta line represents more aggressive smoothing with (7, 1). The green line developed using (9, 2) thus represents further smoothing.

between the original and smoothed profiles for emission peaks was conducted using the formula:

$$R_{\text{err}} = \left(\frac{\text{abs}(I_{\text{org}} - I_{\text{sm}})}{I_{\text{org}}} \right) \times 100 \quad (2.2)$$

Here, R_{err} denotes the relative error, I_{org} represents the intensity of the original line profile, and I_{sm} signifies the intensity of the smoothed line profile.

Table 2.5 reveals that the relative error for (5, 0) always surpasses the error for (9, 2), indicating that (9, 2) is the optimal choice. Figures 2.11 and 2.12 display various spectra for h and k lines from the pixel locations mentioned in Table 2.5, illustrating the accuracy of data smoothing using (9, 2) and (5, 0), respectively. The x-axis signifies the wavelength in Å, while the y-axis denotes the intensity in $\text{erg s}^{-1} \text{cm}^{-2} \text{Å}^{-1} \text{sr}^{-1}$.

Based on the relative discrepancies between the raw and smoothed data, the optimal smoothing parameters were chosen.

The final algorithm was structured on the realisation of the following objectives:

- Data noise reduction through smoothing.
- Identification of all inflection points in the line profile.
- Removal of superfluous points (local minima/maxima).

Table 2.5: Comparison of relative error between the smoothing parameters (5, 0) and (9, 2) and the original data for k_{2v} , k_{2r} , h_{2v} and h_{2r} features on eight random pixel locations.

Pixel location	(5, 0)				(9, 2)			
	k_{2v}	k_{2r}	h_{2v}	h_{2r}	k_{2v}	k_{2r}	h_{2v}	h_{2r}
(0, 25)	4.53 %	10.68 %	8.32 %	8.02 %	1.45 %	6.15 %	5.67%	3.63 %
(53, 177)	4.09 %	8.40 %	8.31 %	10.57 %	0.08 %	3.42 %	4.55%	5.41 %
(0, 38)	11.41 %	11.50 %	13.14 %	16.05 %	5.77 %	5.90 %	7.06%	9.87 %
(1, 34)	11.08 %	5.09 %	11.87 %	3.17 %	5.62 %	2.18 %	6.06%	1.64 %
(40, 270)	7.54 %	14.64 %	8.91 %	12.85 %	3.60 %	8.87 %	4.42%	6.67 %
(3, 11)	10.60 %	12.32 %	9.95 %	8.98 %	6.10 %	6.54 %	5.96%	3.29 %
(30, 427)	7.40 %	10.83 %	8.41 %	10.36 %	2.51 %	6.02 %	3.55%	5.61 %
(13, 150)	8.23 %	9.52 %	6.35 %	11.40 %	3.85 %	4.93 %	2.03%	6.86 %

- Elimination of any consecutive point pairs with values below a third of the standard deviation.
- Maintenance of a single point per region, following the profile's division into five sections based on feature positions.

2.3.2 Algorithm Requirements

The algorithm works well for both the Mg II h and k spectra that form in the photosphere and the chromosphere. Each Mg II h and k line has a central absorption core surrounded by two emission peaks, with outer minima surrounding both; the algorithm thus excludes profiles with a single peak. This suggests that the algorithm can work with any spectrum in any region of the sun, whether in the centre or at the edge of the sun as long as it has the same shape, with two emission peaks, a central absorption core, and local minimums. The algorithm works only with IRIS observations on the disc of the Sun in level 2 Fits file format. Such publicly available data is readily obtainable from the IRIS website, and this work thus utilised a huge amount of data, about 6 TB, to better represent IRIS observations of the centre of the solar disk for the period from 2015 to 2022. Working with this huge data set required a machine with good computing power and a large memory capacity to analyse and store it. Further, even with this in place, as it takes about two minutes to run the code for a single raster profile, approximately four continuous

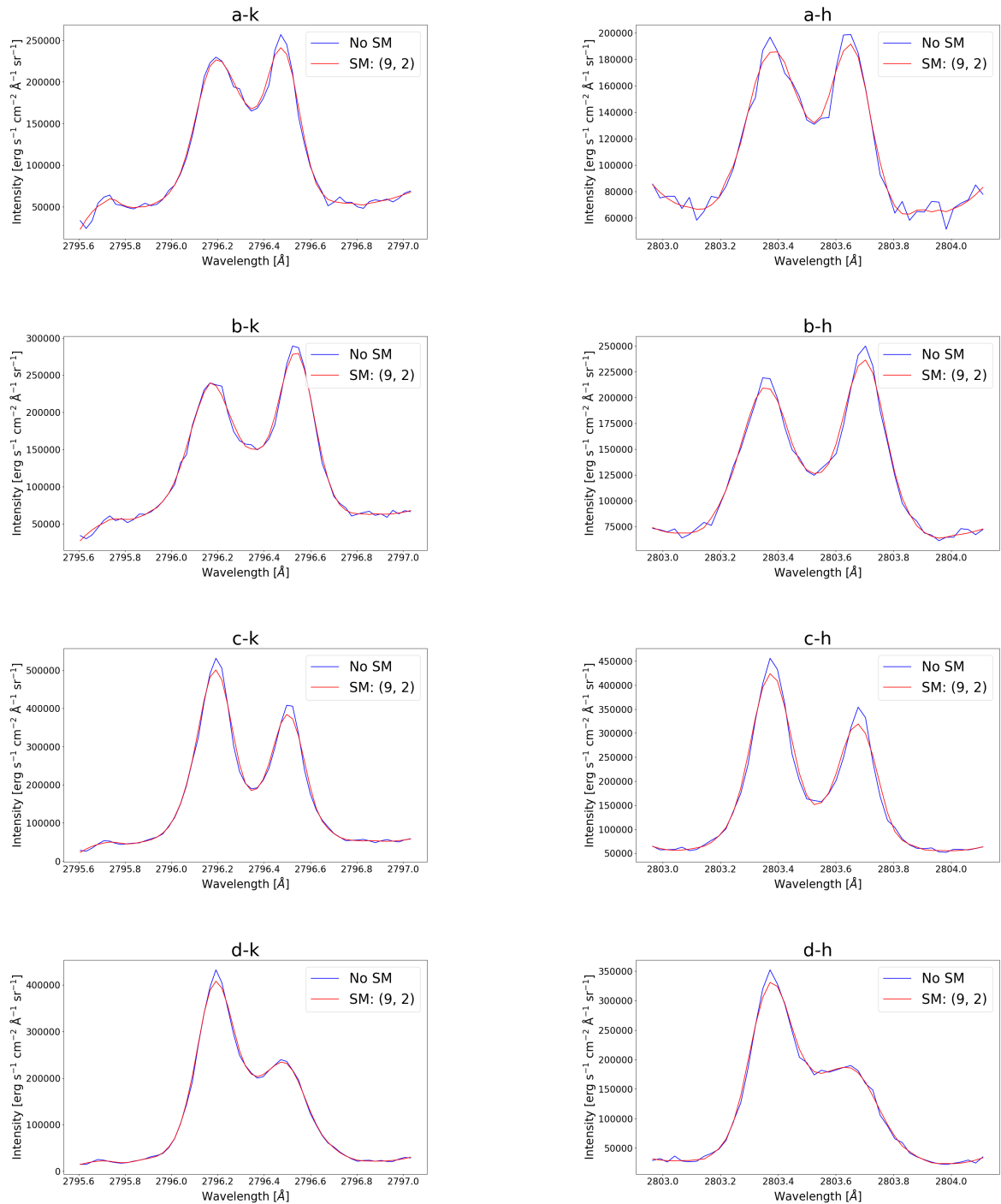


Figure 2.11: Examples of Mg II h&k lines for original and smoothed data at four different pixel locations. Blue line shows the original spectrum, and the red line is the smoothed data. The smoothing parameters are 9 and 2 for window size and polynomial degree, respectively. The left column represents the k line, while the right column represents the h line. Each row represents a pixel location, with a, b, c, and d representing (0, 25), (53, 177), (0, 38), and (1, 34) of these profiles are determined from Fig. 2.4, respectively.

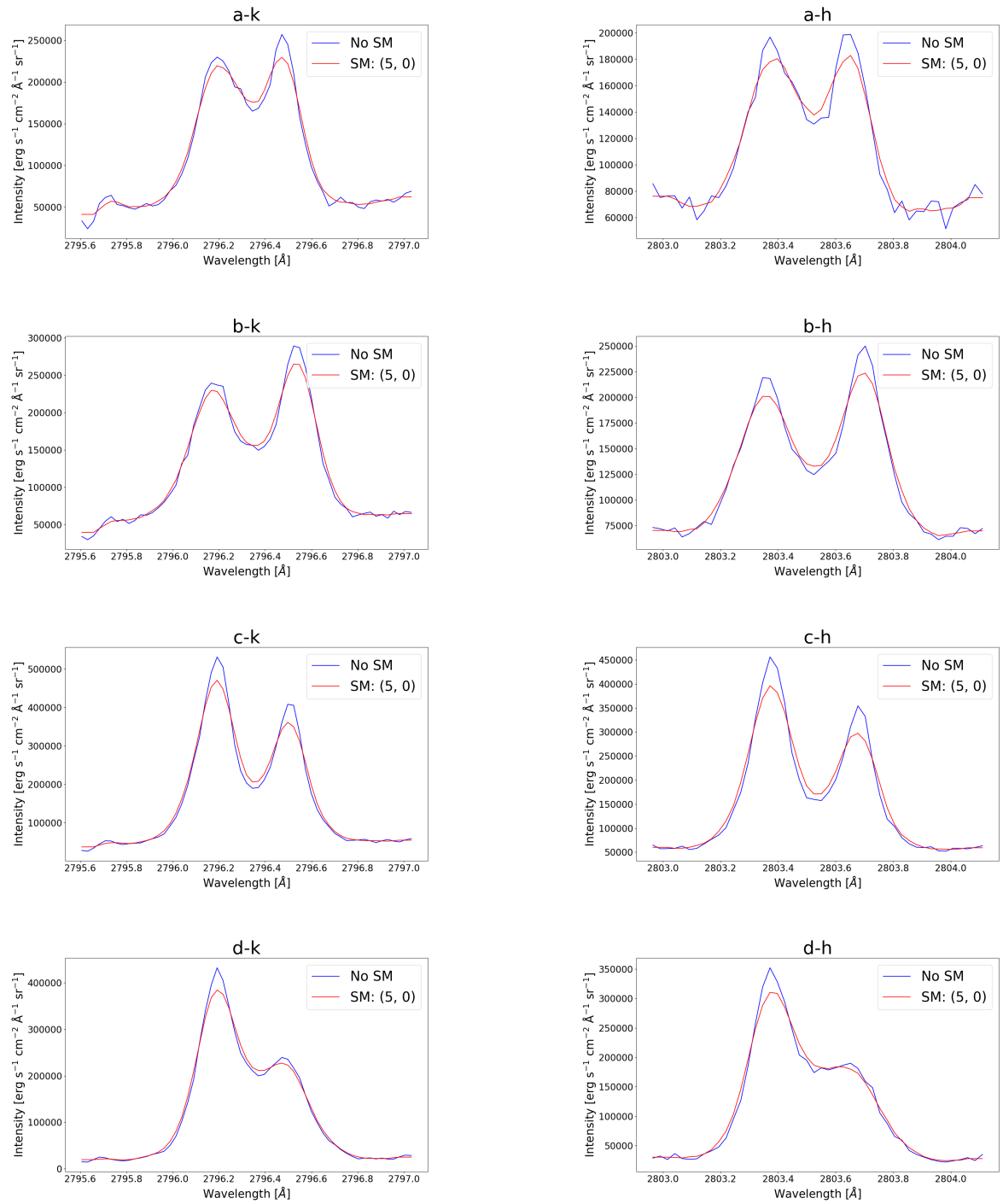


Figure 2.12: As for Fig. 2.11 with smoothing parameters 5 and 0, respectively.

days processing is required to run the code for eight years' data.

2.4 Data Quality Assessment

2.4.1 Applying Code to Synthetic Data

Synthetic data is one way of overcoming a lack of actual data for code testing by creating fake data. The term "synthetic data" thus refers to any data created by a computer program and not based directly on real-world events or phenomena. Random noise can also be included such a dataset.

In this thesis, such synthetic data is utilised to determine how effective the algorithm is at identifying the relevant spectral features (k_1 and h_1 , k_2 and h_2 and k_3 and h_3) of the Mg II h and k lines. The extent of this is determined by the number of profiles excluded and the algorithm's ability to accurately pinpoint the correct position for these spectral features, with the latter illustrated by a good representation of the Gaussian distribution being offered by the wavelength histograms.

2.4.2 Building Synthetic Data

A double Gaussian model with nine parameters was developed to fit a window of width 1.945 \AA centred around the Mg II h line (Schmit et al. [2015]) to generate synthetic data:

$$I(\lambda) = a + b * |\lambda - c| + d * \left(\exp \left(\frac{-(\lambda - f)^2}{g^2} \right) \right) - h * \left(\exp \left(\frac{-(\lambda - j)^2}{k^2} \right) \right) \quad (2.3)$$

where the units for I , a , d , and h are DN , that for b is $DN \text{ \AA}^{-1}$, and that for c , f , g , j , and k are \AA .

Using this equation for different parameters, seven original profiles with a line centre surrounded by two emission peaks, both surrounded by two local minimums, were generated, as illustrated in Figure 2.13. These seven profiles broadly reflect the different types of line profiles that can be found based on relative differences in shapes and intensities of the five features. Each of these seven profiles is then used to generate 9×10^4 further profiles to simulate a wide range of observed profiles. A normal distribution is used to generate random values through two separate distributions that output 300 values each for mean (centered around 0 with a standard deviation of 1) and standard deviation (with a mean of 10 and a standard deviation of 3). For each of the 300 pairs of mean and standard deviation, 78 random values (corresponding to the number of wavelength points across the line profile) are created and added as noise to an original intensity profile. This results in a total of 9×10^4 unique profiles by combining the randomised mean and

standard deviation values. The code was run only on the h line, though code performance for the k line is expected to be at least as effective, if not better, as the k line is stronger than the h line.

Figure 2.13 shows typical profiles generated by the nine-parameter double Gaussian model. In the standard profile, the fit extrema are labelled as follows: h_3 is the reversed core, the emission peaks are h_2 , and the minimum in the wings is h_1 , with the v and r subscripts corresponding to the violet and red sides of the profile, respectively. Panels a, c, d, and f in Fig. 2.13 share peaks that are identical in intensity while b, e, and g do not. The latter case thus offers more chances of determining how robust the algorithm is in terms of determining the five desired spectral features accurately under different conditions.

Examples of profiles created after adding random noise are shown in Fig. 2.14. Both positive and negative noise values were added to the original profiles to make them more similar to the real data from the sun captured by the IRIS spacecraft.

The current study examined only the Mg II h line at 2803.538 \AA , thus utilising the wavelength array for the same observed values as obtained from IRIS, which offers a resolution of 25 m\AA with wavelengths ranging from 2802.565 \AA to 2804.510 \AA . A 1.945 \AA wide spectral window centred on the Mg II h line was thus considered. We used the SG method here in the same way as on the real data obtained from the IRIS spacecraft (smoothing only the wings depending on a wavelength limit). The values nine and two were thus used for window length and polynomial order, respectively, to smooth out the noise from the synthetic data, as shown in Fig. 2.15.

2.4.3 Assessing Code Performance on Synthetic Data

This section assesses the effectiveness of the algorithm in terms of determining the desired spectral features using synthetic data. The algorithm was tested by running it on each original profile separately, resulting in varying results in terms of the number of excluded profiles. Figure 2.16 shows an example of the results for one profile (a) from among the seven original profiles created that were each expanded to 9×10^4 profiles with the addition of different patterns of noise. Adding noise randomly produced data with a range of mean values between 0 and 1 and a range of standard deviation values between 3 and 10. Table 2.6 shows the average values for the number of excluded profiles after the code was run five times, each with a unique random noise seed, resulting in varied line profiles for each time. In profiles (a), (c), (f) and (g), a close average of excluded files, between 0 and 1%, was obtained: the exact values were 0.05%, 0.86%, 0%, and 0.01%, respectively. In contrast, figures of 2.24% for profile (b) and 4.99% for profile (e) were obtained, while profile (d) was very extreme in terms of the average percentage of excluded files at 51.17%. This high value occurred because this profile had a very low intensity, so that any noise added to the profile has a large effect, making the profile more complex. Similarly, profile (f) had high intensities relative to the other profiles, so any added noise had little influence, re-

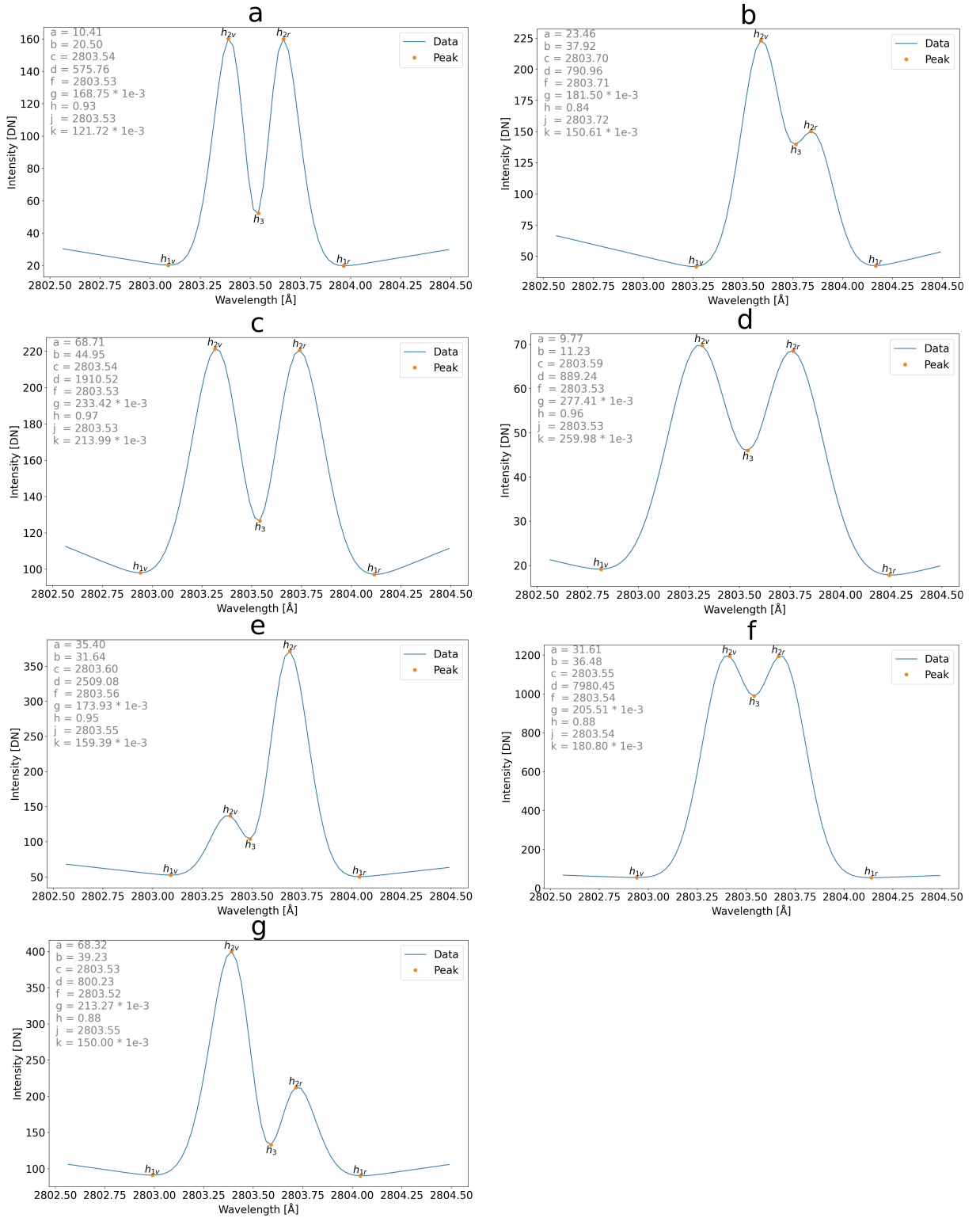


Figure 2.13: Seven double peak profiles panels using a nine-parameter double Gaussian model. The legend at the top left of each panel presents the model parameters as per Equation (2.3).

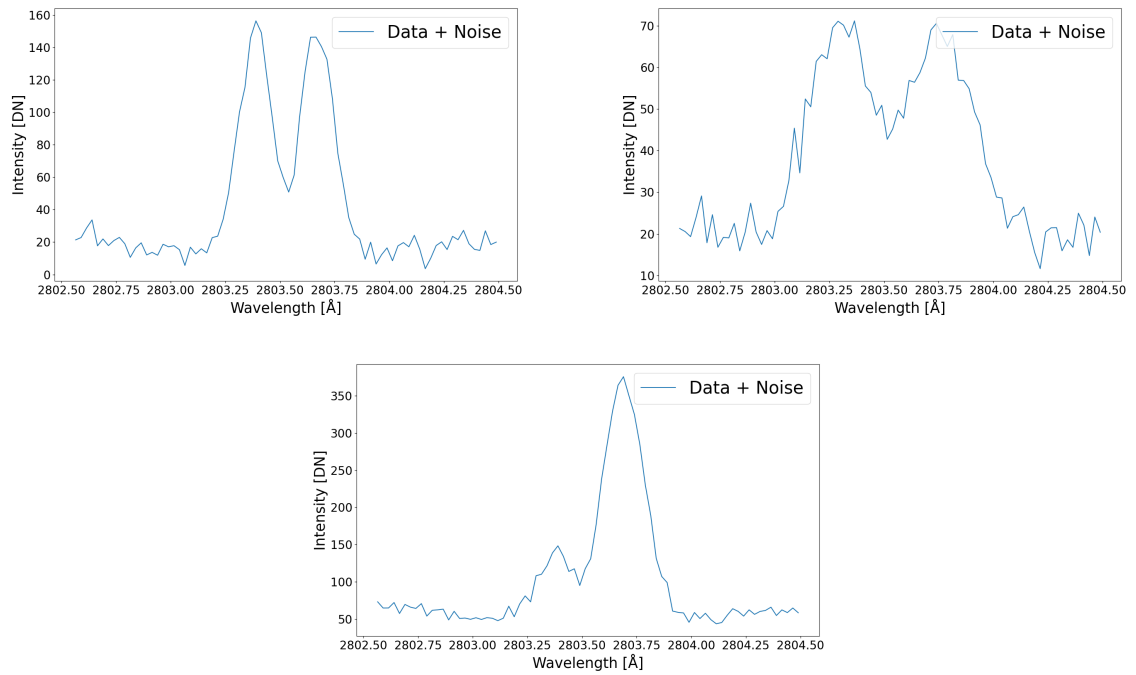


Figure 2.14: Original profiles in panels a, d and e (see Fig. 2.13) after adding noise.

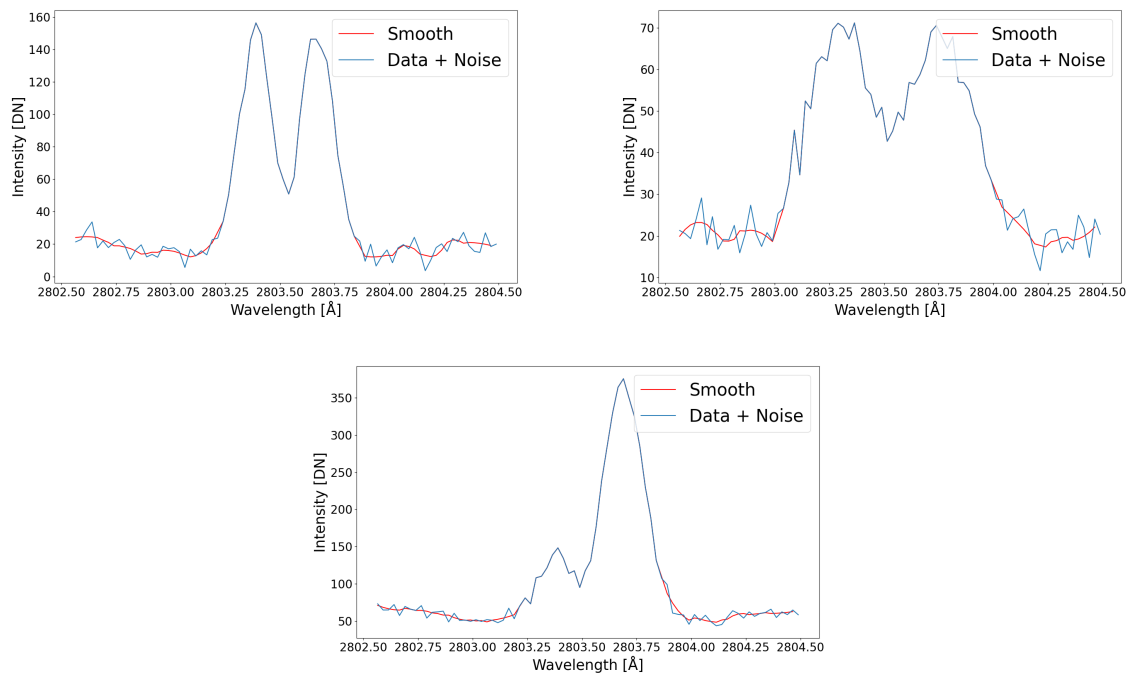


Figure 2.15: Profiles as in Fig. 2.14 smoothing only the wings. The blue line represents the noisy profile, while the orange line depicts the smoothed profile.

Table 2.6: Comparison of the number and percentage of excluded profiles among the synthetic profiles is shown in Fig. 2.13. The first column shows the original files created with a nine-parameter double Gaussian model from (a) to (g), while the second to sixth columns represent the number of excluded profiles, with the relevant percentage given in parentheses. The final column shows the average number and percentage of excluded profiles resulting from running the code five times for each file in columns 2 to 6.

Original profile	Number of excluded line profiles (Percentage of 90000 profiles)					Average
	1	2	3	4	5	
a	29 (0.03%)	49 (0.05%)	46 (0.05%)	44 (0.05%)	40 (0.04%)	42 (0.05%)
b	2063 (2.29%)	2027 (2.25%)	2048 (2.28%)	2104 (2.34%)	1816 (2.02%)	2012 (2.24%)
c	913 (1.01%)	765 (0.85%)	906 (1.01%)	723 (0.80%)	540 (0.60%)	770 (0.86%)
d	46036 (51.15%)	45545 (50.61%)	47706 (53.01%)	45261 (50.29%)	45722 (50.80%)	46054 (51.17%)
e	3974 (4.42%)	4478 (4.98%)	4358 (4.84%)	4696 (5.22%)	4961 (5.51%)	4493 (4.99%)
f	0 (0%)	0 (0%)	0 (0%)	0 (0%)	0 (0%)	0 (0%)
g	19 (0.02%)	6 (0.01%)	10 (0.01%)	7 (0.01%)	21 (0.02%)	13 (0.01%)

sulting in no excluded profiles.

All wavelength and intensity histograms for each original profile were plotted as for the real data for both h&k lines shown in Sec. 2.5; however, only the spectral features of the h line, h_{1v} , h_{2v} , h_3 , h_{2r} , and h_{1r} were used. Each histogram was also fitted with a Gaussian distribution. Figures 2.16 to 2.22 show that the Gaussian distribution offers a relatively good description of the wavelength and intensity histograms. Although there were noticeable differences in the number of bins between the synthetic and the IRIS-observed data when examining features h_{2v} , h_{2r} , and h_3 , the code was successful in determining the spectral features based on it producing the expected output. These differences mean the range of possible values for the parameters is the same, but the resolution within the parameter space is higher for synthetic profiles.

The vertical red-dash line displayed on all panels in Figures 2.16 to 2.22 represents the reference wavelength and intensity for each feature, as obtained from their values in the original profiles before any noise was added (Fig. 2.13). In h_{2v} , h_{2r} , and h_3 , the wavelength histograms are as expected, as these refer to the bins with the highest number of points; the noise has little effect in these positions. In contrast, the noise in all seven original profiles shifted towards the larger wavelengths in the h_{1v} and towards the shorter wavelengths in the h_{2r} . This shift was assessed by calculating the velocity of h_{1v} and h_{1r} with respect to the difference between the wavelength of the vertical line and the wavelength of the top of the Gaussian distribution, as shown in Table 2.7. All the profiles are close in velocity, at almost less than 5 km s^{-1} , with the exception of the original profile (d), which has a velocity of more than 16 km s^{-1} , almost three

Table 2.7: Velocities among the synthetic profiles in Fig. 2.13. The first column shows the original files (a) to (g) created with a nine-parameter double Gaussian model. The second column represents the velocity of h_{1v} and h_{1r} with respect to the difference between the wavelength of the vertical line and the wavelength of the top of the Gaussian distribution.

Original profile	Velocity (km s ⁻¹)	
	h_{1v}	h_{1r}
a	- 4	3.5
b	- 1.5	3.2
c	- 4.8	4.3
d	- 16.4	16.6
e	- 3.3	2.5
f	- 4.5	4.5
g	- 3.7	2.9

times the velocities of the other original profiles. Original profile (d) has a much lower intensity than the other original profiles, the effect of noise is also very large in this profile, leading to a more significant shift, which results in this large velocity as compared to other profiles.

Table 2.8 shows the wavelength and intensity values for the original seven profiles and the actual value wavelength and intensity ranges for all spectral features in these profiles after the addition of noise. By comparing the expected values with the histograms obtained from the seven synthetic profiles, the values can be seen to be fairly close, except in the case of original profile (d).

One indicator of algorithm accuracy is the width of the distribution associated with each spectral feature. A narrower distribution suggests a higher level of precision in identifying spectral features. In this work, we analyse the widths of the distribution of h_{2v} , h_3 , h_{2r} , h_{1v} , and h_{1r} features to assess the algorithm's accuracy in identifying these spectral characteristics. The analysis of the widths in h_{2v} , h_3 , and h_{2r} features revealed widths of 0.03, 0.03, and 0.02 Å, respectively (see Fig. 2.16, left column). These narrow widths indicate that the algorithm has a high degree of accuracy in locating these spectral features. The precise identification of h_{2v} , h_3 , and h_{2r} lines suggests the algorithm's robustness and its ability to discern subtle variations in the spectral data. However, as depicted in Fig. 2.16, the widths for h_{1v} and h_{1r} were found to be 0.1 Å for both features. This broader width indicates that the algorithm's accuracy in locating these spectral features is relatively lower. The wider distribution suggests a relatively reduced ability to precisely pinpoint the positions of the h_{1v} and h_{1r} features. This lack of accuracy can be attributed to the possibility that the outer wing features are situated beyond the boundaries of the line profile.

Overall, the histograms indicated reasonably acceptable velocity calculations derived from

Table 2.8: The original seven profiles' wavelength and intensity values and their manually estimated ranges for all spectral features after the addition of noise. The first column shows the original files (a) to (g) (as in Fig. 2.13) created with a nine-parameter double Gaussian model. The units of the wavelengths (λ) and intensities (I) are Å and DN, respectively.

Profile No.	Profile Type	h1v		h2v		h3		h2r		h1r	
		λ	I	λ	I	λ	I	λ	I	λ	I
a	Original	2803.09	20.28	2803.39	160.15	2803.54	52.30	2803.67	160.07	2803.97	19.87
	Noise	2802.93 - 2803.25	5 - 35	2803.36 - 2803.42	145 - 175	2803.51 - 2803.57	37 - 67	2803.64 - 2803.70	145 - 175	2803.81 - 2804.13	5 - 35
b	Original	2803.27	41.82	2803.59	223.10	2803.77	139.82	2803.84	150.15	2804.17	42.46
	Noise	2803.11 - 2803.43	27 - 57	2803.56 - 2803.62	208 - 238	2803.74 - 2803.8	125 - 155	2803.8 - 2803.89	135 - 165	2803.01 - 2804.33	27 - 57
c	Original	2802.94	97.96	2803.32	221.38	2803.54	126.56	2803.74	220.71	2804.12	97.08
	Noise	2802.78 - 2803.1	83 - 113	2802.29 - 2803.35	206 - 236	2803.51 - 2803.57	112 - 142	2803.71 - 2803.77	206 - 236	2803.96 - 2804.28	82 - 112
d	Original	2802.82	19.19	2803.32	69.76	2803.54	46.01	2803.77	68.52	2804.24	17.84
	Noise	2802.66 - 2802.98	4 - 34	2803.25 - 2803.35	55 - 85	2803.48 - 2803.59	31 - 60	2803.7 - 2803.81	54 - 84	2804.08 - 2804.4	3 - 33
e	Original	2803.09	52.65	2803.39	137.07	2803.49	104.06	2803.69	371.40	2804.04	50.37
	Noise	2802.93 - 2803.25	38 - 68	2803.32 - 2803.43	122 - 152	2803.44 - 2803.51	89 - 119	2803.66 - 2803.72	356 - 386	2803.88 - 2804.20	35 - 65
f	Original	2802.94	55.33	2803.42	1194.82	2803.54	989.63	2803.67	1194.09	2804.14	54.60
	Noise	2802.83 - 2803.15	40 - 70	2803.37 - 2803.45	1180 - 1210	2803.5 - 2803.58	975 - 1005	2803.64 - 2803.71	1179 - 1209	2803.94 - 2804.26	40 - 70
g	Original	2802.99	91.17	2803.39	399.98	2803.59	133.31	2803.72	212.44	2804.04	90.41
	Noise	2802.83 - 2803.15	76 - 106	2803.36 - 2803.42	385 - 415	2803.56 - 2803.62	118 - 148	2803.68 - 2803.77	197 - 227	2803.88 - 2804.2	75 - 105

the displacement of the peak of the Gaussian fit relative to the spectral feature values in the original profiles. In addition, comparing the estimated values of wavelengths and intensity in Table 2.8 with the histograms seen in Figures 2.16 to 2.22, the values in the histograms can be explained well by applying the actual values in the table. Thus, the algorithm performs well in terms of automatically determining the spectral features in the Mg II h&k lines; however, these results may be less reliable for very noisy spectra.

2.4.4 Comparison with IRIS IDL Code

This section discusses the relative performance of the new algorithm against that of the `iris_get_mg_features_lev2` IDL procedure as described in Leenaarts et al. [2013b] and Pereira et al. [2013]. A summary of the IDL algorithm, which aimed to identify the central reversal k_3 , h_3 and line peaks k_{2r} , k_{2v} , h_{2r} , h_{2v} of the h and k lines of Mg II is thus offered below:

- Look for extrema in a range of $\pm 40 \text{ km s}^{-1}$ around the resting wavelength.
- Identify the line-centre (LC) velocity and seek a parabolic fit for a few spectral points around the estimate to give the final line centre velocity. Outliers may be identified using a Gaussian filter, and a normalized Gaussian kernel with a given standard deviation is commonly used. These outliers are then passed through the LC fit process once more, using the weighted mean of neighboring pixels as an initial estimate.
- Identify the LC intensity by looking for peaks within a range of 10 km s^{-1} . The most straightforward case involves taking the minimum between two maxima. For several minima, the lowest is selected. If only one peak is identified within the 20 km s^{-1} range, the derivative method for blended peaks is used, taking a minimum of $\frac{dI}{d\lambda}$ (Pereira et al. [2013]). Afterwards, a parabolic fit is created around the estimate.
- Calculate the positions of the peaks by performing cubic spline interpolation of the initial estimates on a higher resolution wavelength grid. The initial estimates will be found within $\pm 30 \text{ km s}^{-1}$ of the LC. Peaks that are separated by less than $\pm 10 \text{ km s}^{-1}$ are discarded (inter-peak separation), while each peak's position with respect to LC dictates whether it corresponds to a blue or a red peak. Final velocity shifts and intensities for the peaks are obtained from the interpolated spectra.

Pereira et al. [2018] discussed areas where the IDL code struggles to perform well. The main issues appear to be related to cropped profiles with features incorrectly identified, which is addressed to some extent by the steps described above that look for outliers, while in the current Python code used in this study, the use of noise filtering is added as a further step to remove outliers. The sign difference between consecutive points accurately identifies any points

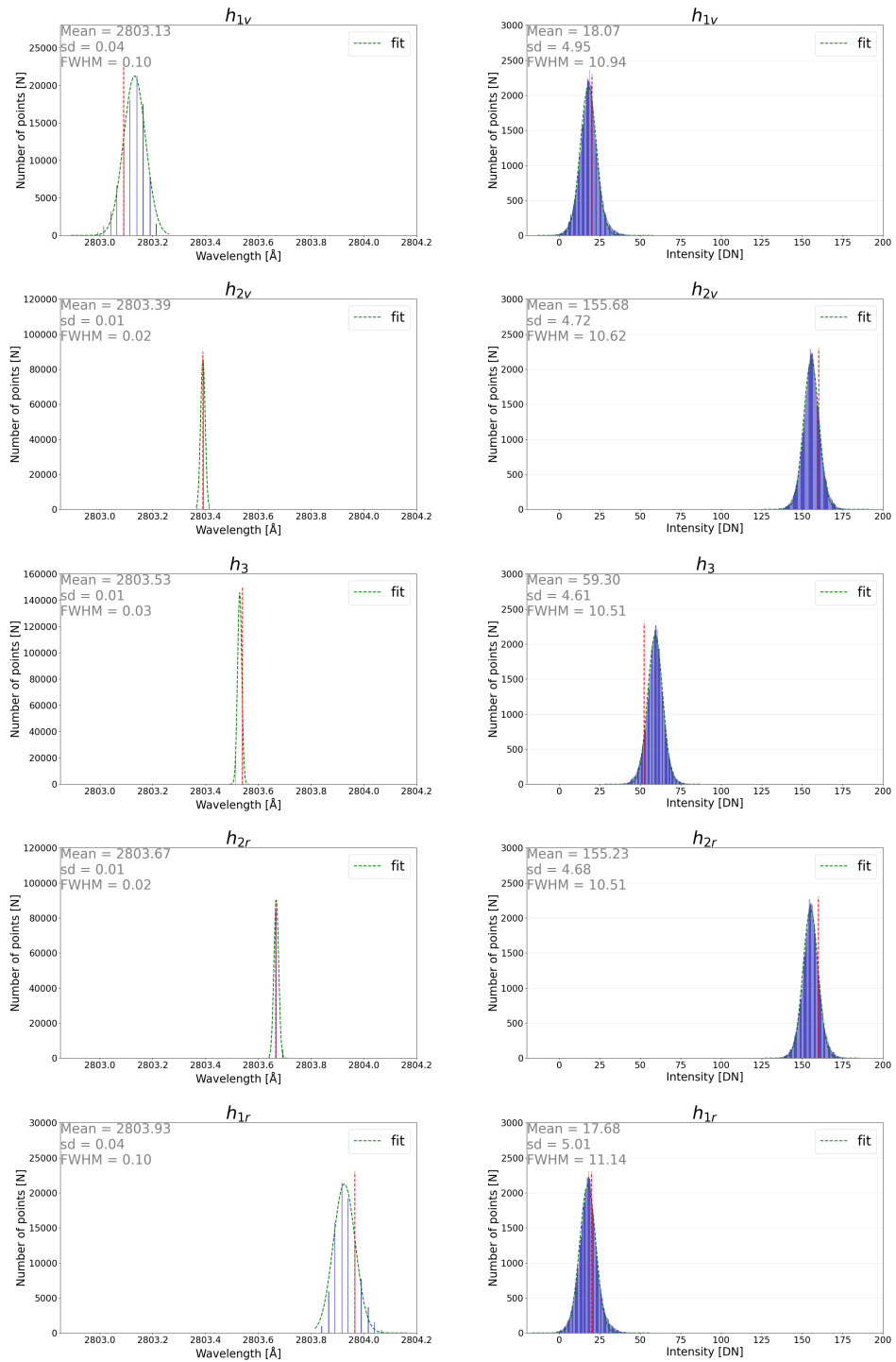


Figure 2.16: Histograms of wavelength and intensity for the h parameters of Mg II h line in original synthetic profile (a) (Fig. 2.13). The green dashed line represents the Gaussian distribution, while the red vertical line represents the predicted wavelength from the original synthetic profile. The legend at the top left for each panel shows the mean, the standard deviation, and the width of the distribution.

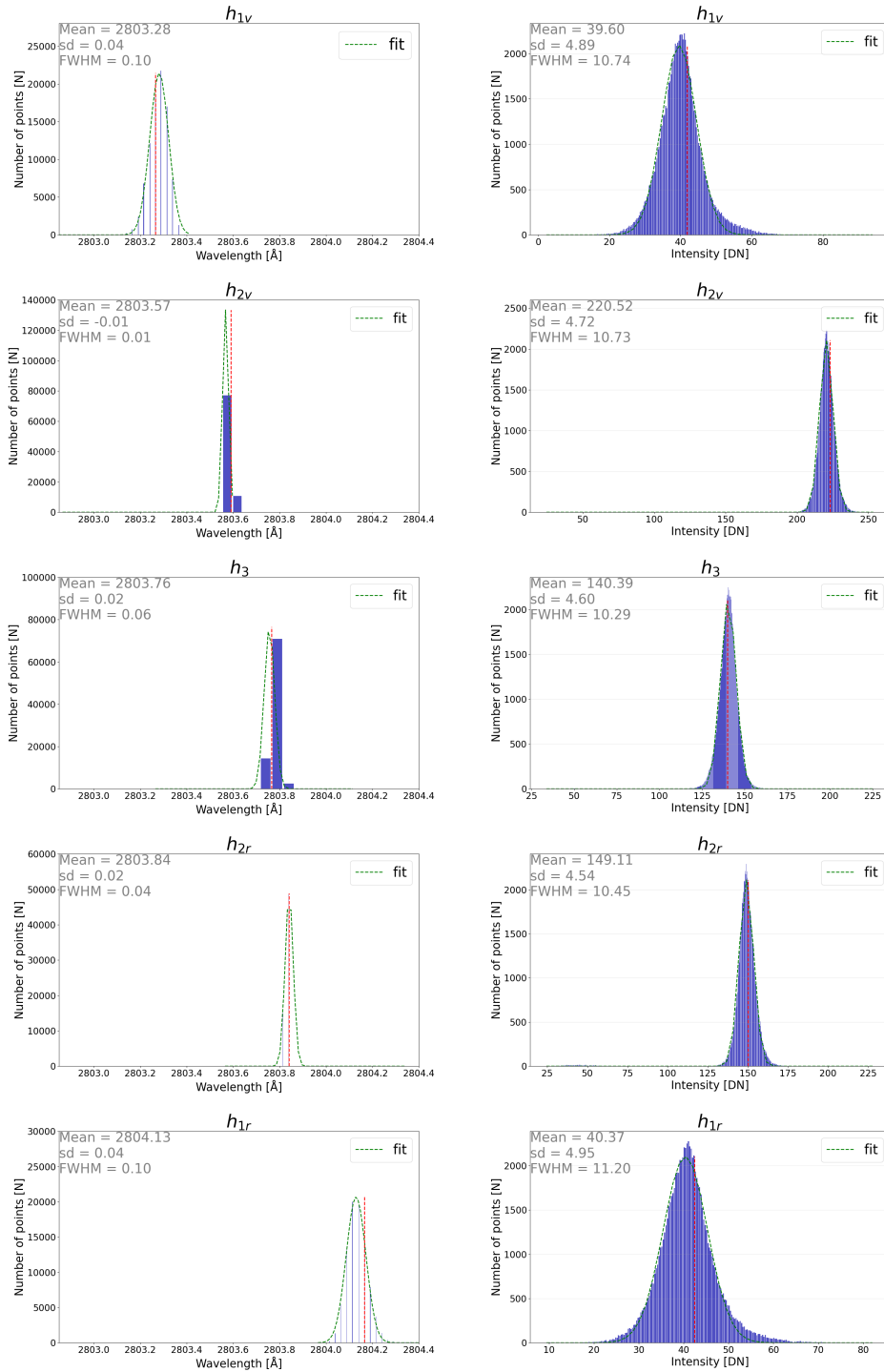


Figure 2.17: As with Fig. 2.16, but for original profile (b) from Fig. 2.13.

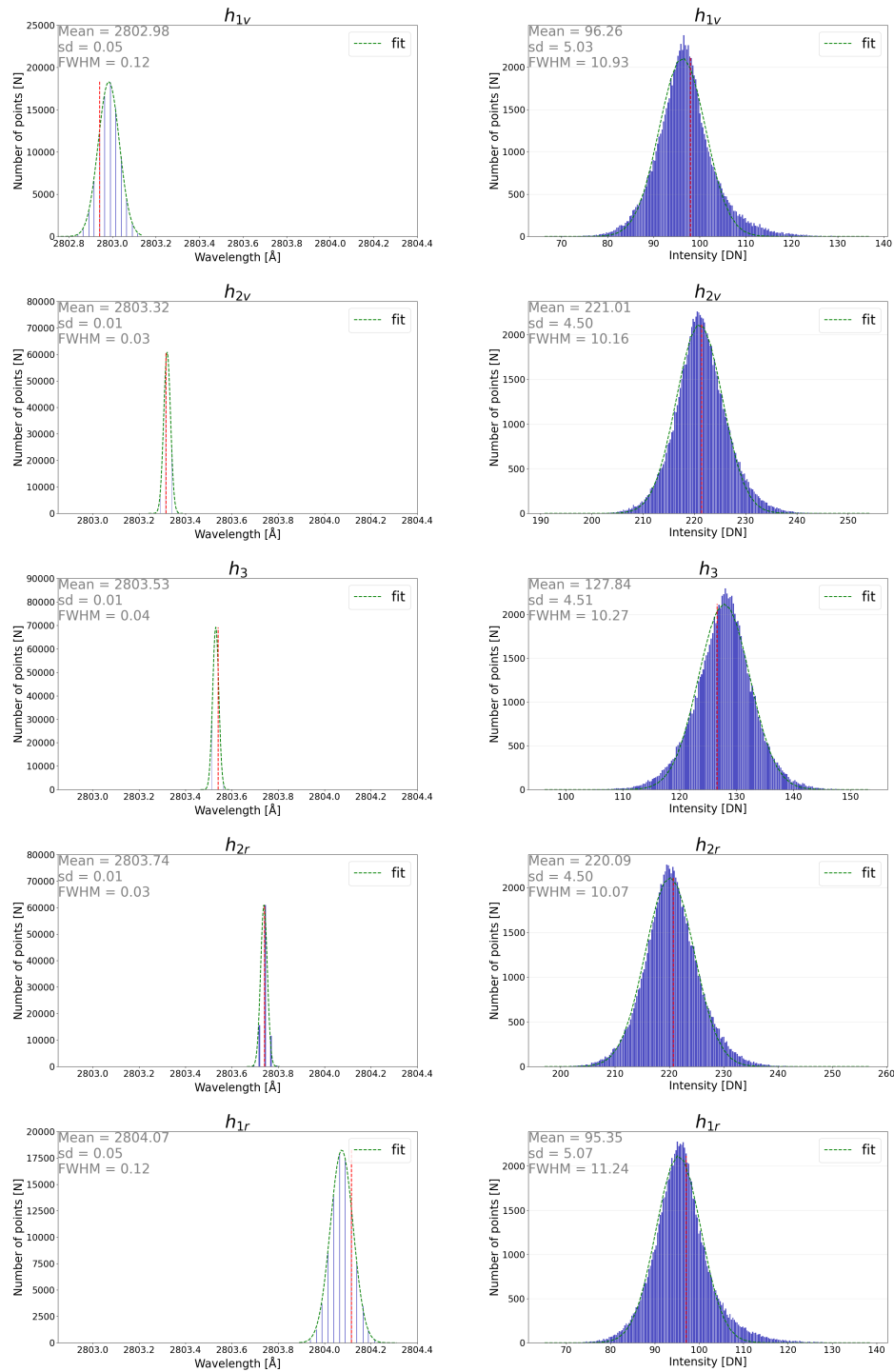


Figure 2.18: As for Fig. 2.16, but for original profile (c) in Fig. 2.13.

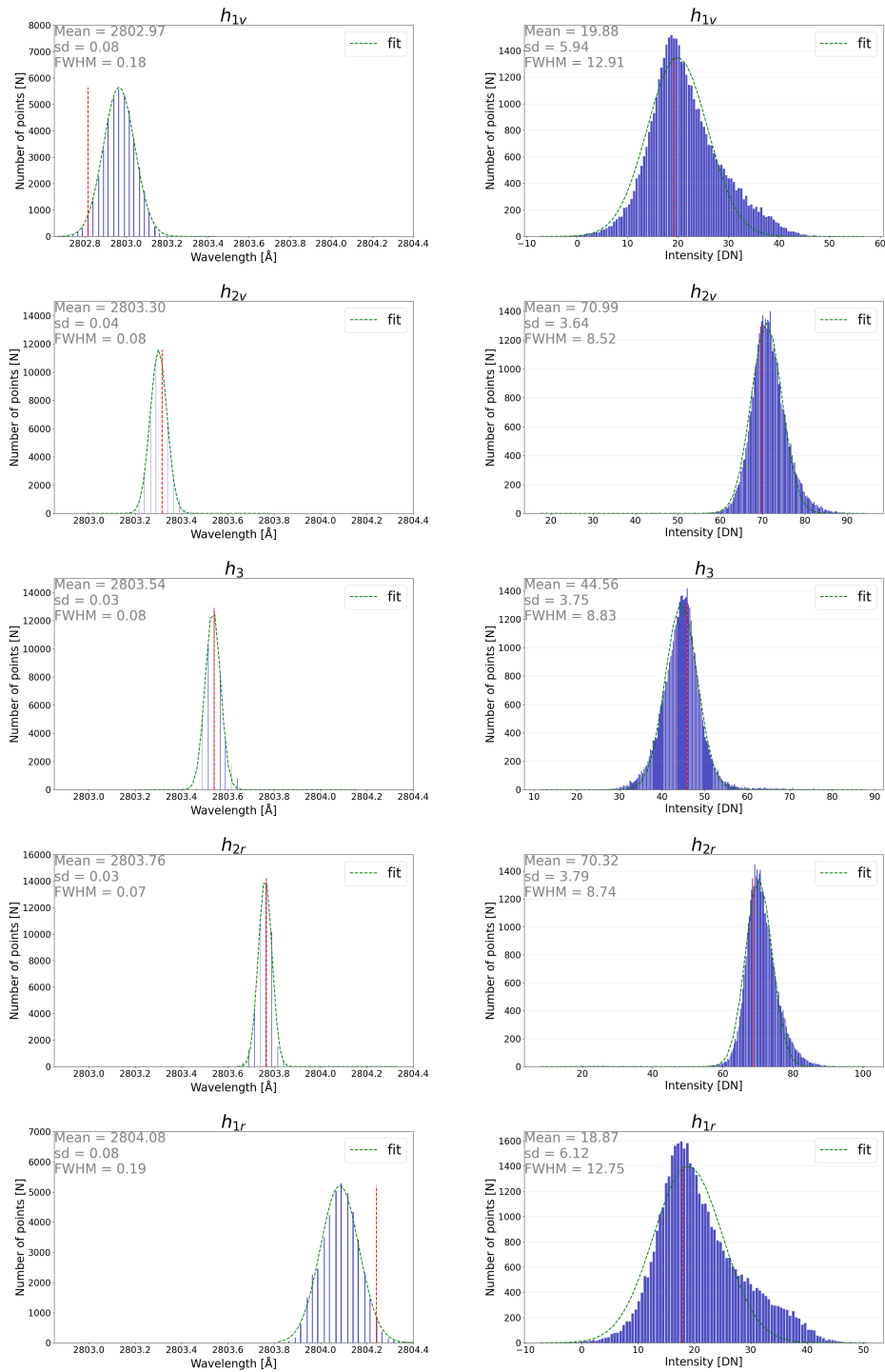


Figure 2.19: As for Fig. 2.16, but for original profile (d) in Fig. 2.13.

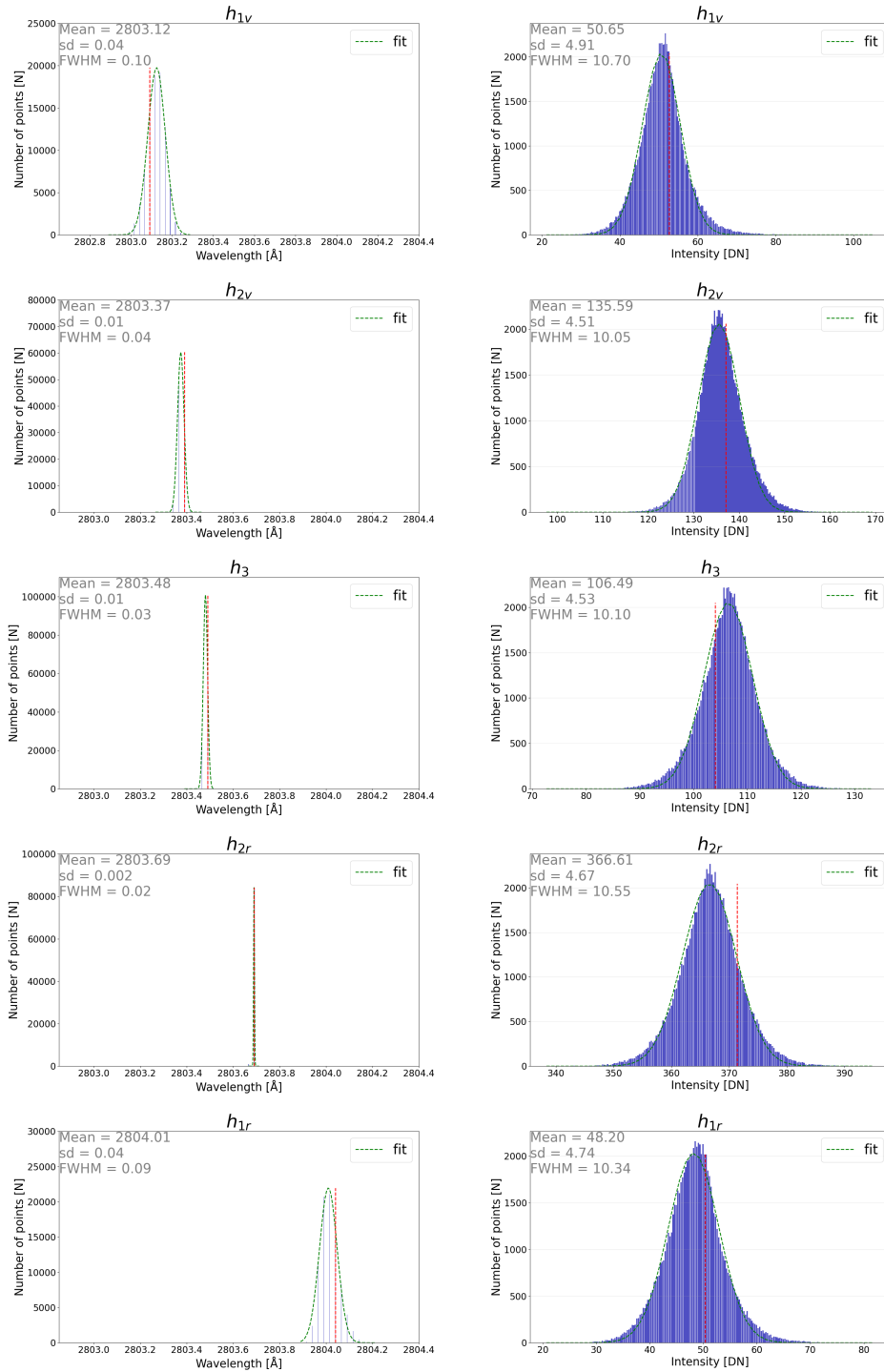


Figure 2.20: As for Fig. 2.16, but for original profile (e) in Fig. 2.13.

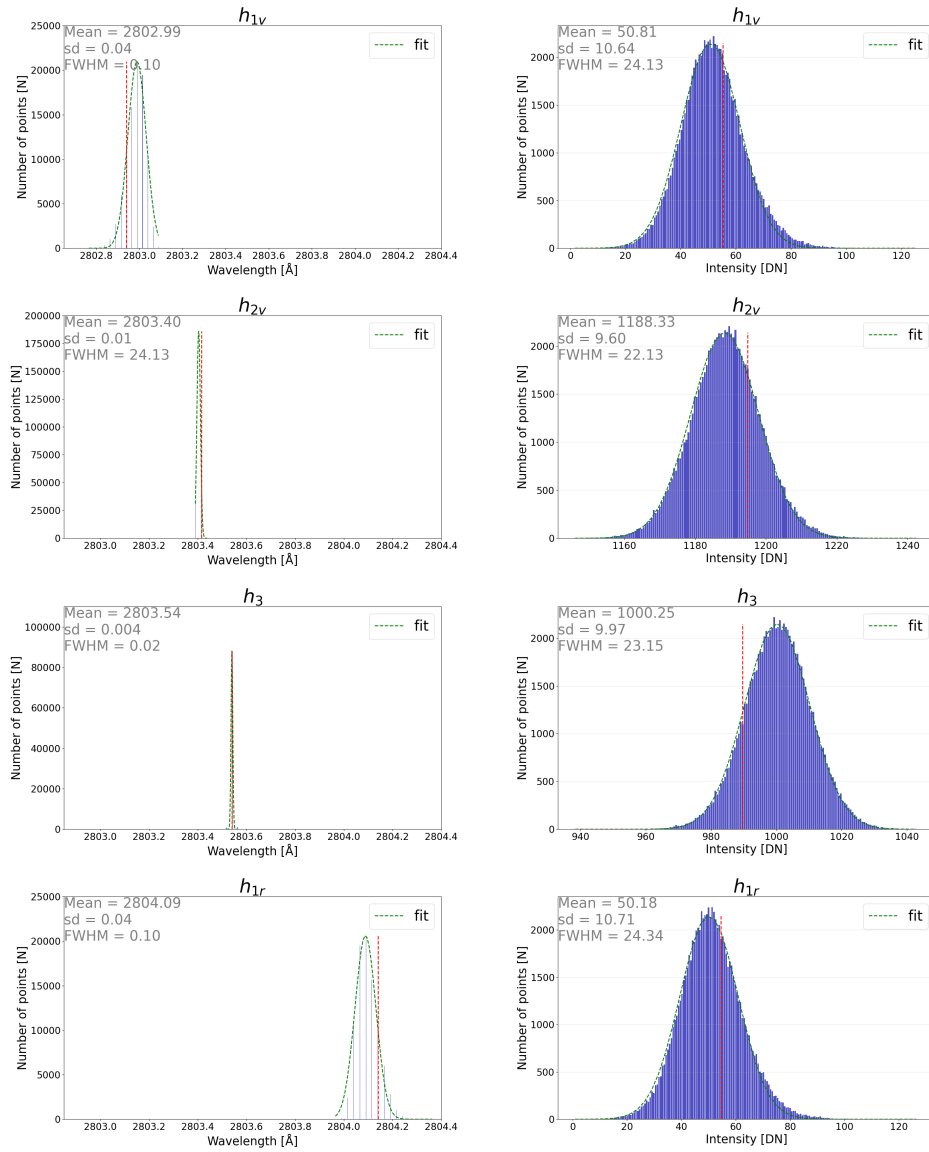


Figure 2.21: As for Fig. 2.16, but for original profile (f) in Fig. 2.13.

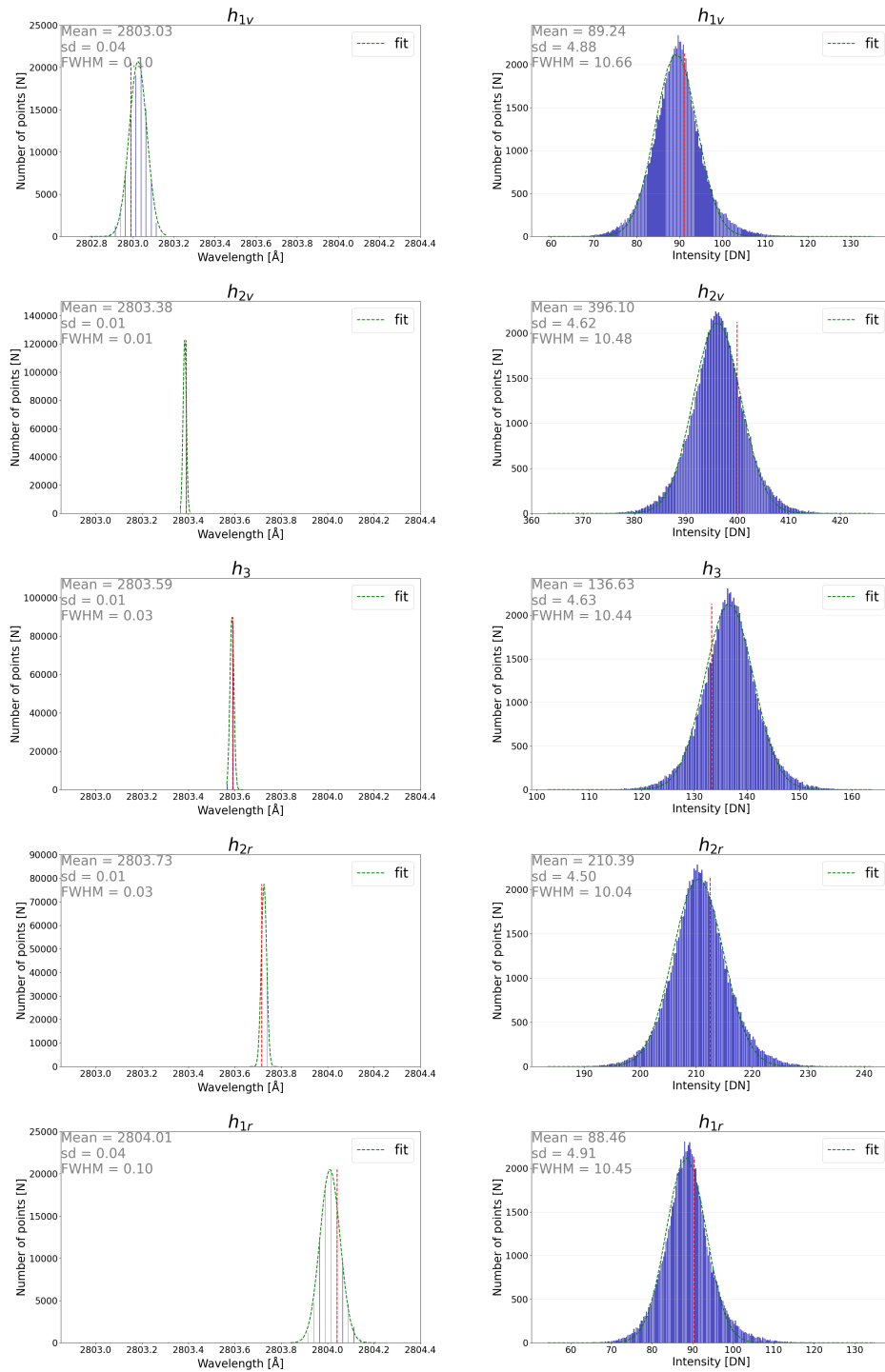


Figure 2.22: As for Fig. 2.16, but for original profile (g) in Fig. 2.13.

of inflection, while dividing the line profile into five regions allows removal of unwanted local minima and maxima.

Both their method and our method aim to identify the main line features of the Mg II lines. The former relies on a Gaussian filter and a cubic spline interpolation, allowing precise estimation around the rest wavelength and increased resolution for peak positions. However, it occasionally struggles with cropped profiles, sometimes misidentifying high-intensity points. Conversely, our algorithm employs noise filtering to effectively remove outliers and uses the sign difference between consecutive points to identify the locations of inflection points. Moreover, our algorithm identifies positions and intensities of h_1 and k_1 , allowing us to expand the range of atmospheric depths probed. While our method seems more accurate in some situations, especially in identifying k_3 and managing complex profiles, the best choice might vary depending on the specific dataset and user requirements.

2.5 Results: Histograms

This work plotted all histograms for k_{1v} , k_{2v} , k_3 , k_{2r} , and k_{1r} , as well as h_{1v} , h_{2v} , h_3 , h_{2r} , and h_{1r} , and fitted them to a Gaussian distribution. These plots contained ten local maxima and minima for the Mg II h&k line profiles, with each having two plots (a and b). The x-axis in (a) represents the wavelength, and the y-axis represents the total number of pixels in each corresponding wavelength bin, as seen in Fig. 2.23, while the x-axis in (b) represents the intensity, and the y-axis represents the total number of pixels in each corresponding intensity bin, as seen in Fig. 2.24. To do fitting for every single pixel in the raster, particularly within the wings, we employed the Savitzky-Golay (SG) filtering technique to minimise noise interference. The parameters chosen for this process were a window length of nine and a polynomial order of two (see Sec. 2.2.4 and Smoothing Data in Sec. 2.3.1). Additionally, for the construction of wavelength and intensity histograms, we utilised the 'matplotlib.pyplot.hist' function available within the Python library.

Figures 2.23 and 2.24 show the histograms of the wavelengths and intensities of the spectral features of interest for all pixels in the raster as presented in Sec. 2.2.2, respectively. The wavelength histograms are relatively well described by Gaussian distributions, and the spread in wavelengths is clearly larger for k_{1v} , k_{1r} , h_{1v} and h_{1r} , which may be expected due to their lower intensities and can be attributed to the possibility that the outer wing features are situated beyond the boundaries of the line profile. In Figure 2.23, most of the points are clustered on the central part of the wavelength axis, as expected. Examining intensity in Fig. 2.24, the k_1 & h_1 points are at lower intensities than k_2 & h_2 and k_3 & h_3 , while the k_2 & h_2 points are the largest intensities, again, as expected. The spreads of and differences in the k_{2v} and k_{2r} histograms suggest variations in temperature and velocities of the chromospheric regions where these peaks are formed (Pereira et al. [2013]), while the intensity histograms allow exploration of the relative

contributions of different quiet Sun features to the total emissions seen in the Mg II lines.

The analysis of the widths for k_{1v} , k_{2v} , h_{2v} , k_3 , h_3 , k_{2r} , h_{2r} and h_{1r} wavelength distributions shows values of between 0.03 and 0.09 Å, respectively (refer to Fig. 2.23). These values suggest that the algorithm is relatively accurate when it comes to identifying these particular spectral lines. This accuracy in locating k_{1v} , k_{2v} , h_{2v} , k_3 , h_3 , k_{2r} , h_{2r} and h_{1r} underlines the algorithm's capability to recognise minor fluctuations in the spectral information. In contrast, Fig. 2.23 shows that the widths of the k_{1r} and h_{1v} wavelength distributions were measured at 0.14 and 0.12 Å, respectively. This shortfall in precision could be due to the outer wing features being located outside the line profile boundaries, potentially due to their merging into the nearby continuum or being more affected by noise. The algorithm's relative accuracy is judged by how closely it identifies spectral lines, with a narrower FWHM indicating sharper, more precise detection. Most detected lines show FWHM values between 0.03 and 0.09 Å, indicating good precision. However, a couple of lines have a broader FWHM (0.12 and 0.14 Å), suggesting less precision, possibly due to noise or blending with nearby lines. Therefore, "relatively accurate" means the algorithm generally identifies lines precisely, with some exceptions.

In assessing the code performance for spectral feature detection, we observe that FWHM of the measurements, as depicted in Fig. 2.23, approaches the uncertainty level of the code's detection ability, as determined by the FWHM of the test profiles illustrated in Fig. 2.16. The test profile for h_{2v} (Fig. 2.16) exhibits a FWHM of 0.03 Å, which establishes the range of uncertainty for the code's detections. In contrast, the FWHM of h_{2v} derived from the observed data, presented in Fig. 2.23, is recorded at 0.08 Å. The proximity of this observed FWHM to the uncertainty range suggests a decrease in the accuracy of the algorithm when detecting spectral features. The accuracy of the algorithm in detecting spectral features decreases, perhaps because the noise level is greater in the degraded synthetic features than in the actual data.

2.6 Conclusion

A new method for automatically determining the positions of the Mg II h&k spectral line features has been developed. Synthetic data was generated using a nine-parameter double Gaussian model (6.3×10^5 profiles) to test the accuracy and effectiveness of our algorithm in determining these spectral features. The results that we obtained from the synthetic data histograms proved the algorithm's effectiveness in determining the spectral features of the Mg II h&k lines. In observed data obtained from IRIS, the Gaussian distribution fitted the wavelength histograms reasonably well, but not the intensity histograms, which were clearly asymmetrical and not well fitted by the Gaussian distribution.

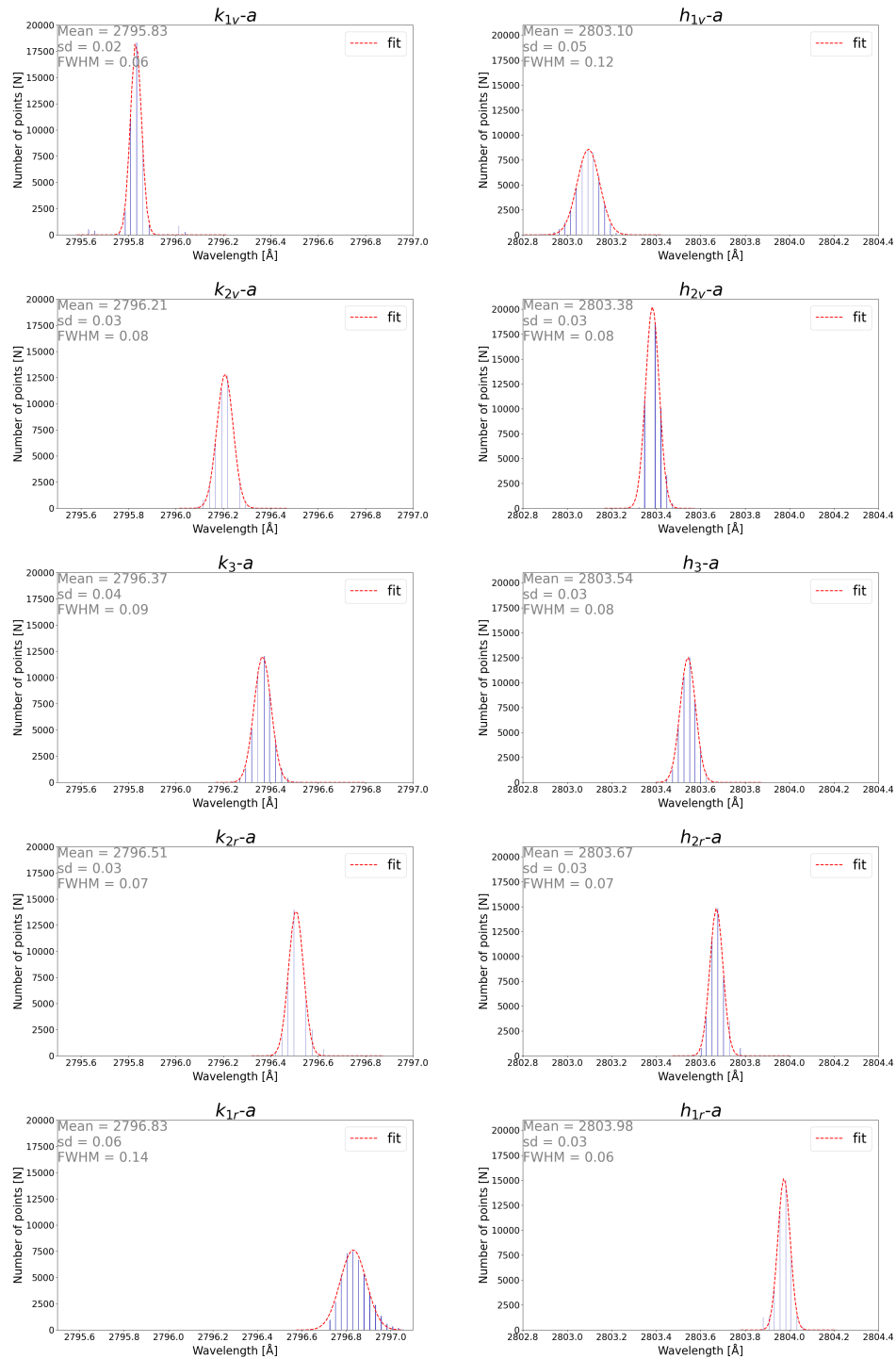


Figure 2.23: Wavelength histograms for profile features of Mg II h&k lines in one raster as obtained by IRIS on July 23, 2019. The dashed red line represents the Gaussian distribution. The legend at the top left for each panel shows the mean, the standard deviation, and the width of the distribution.

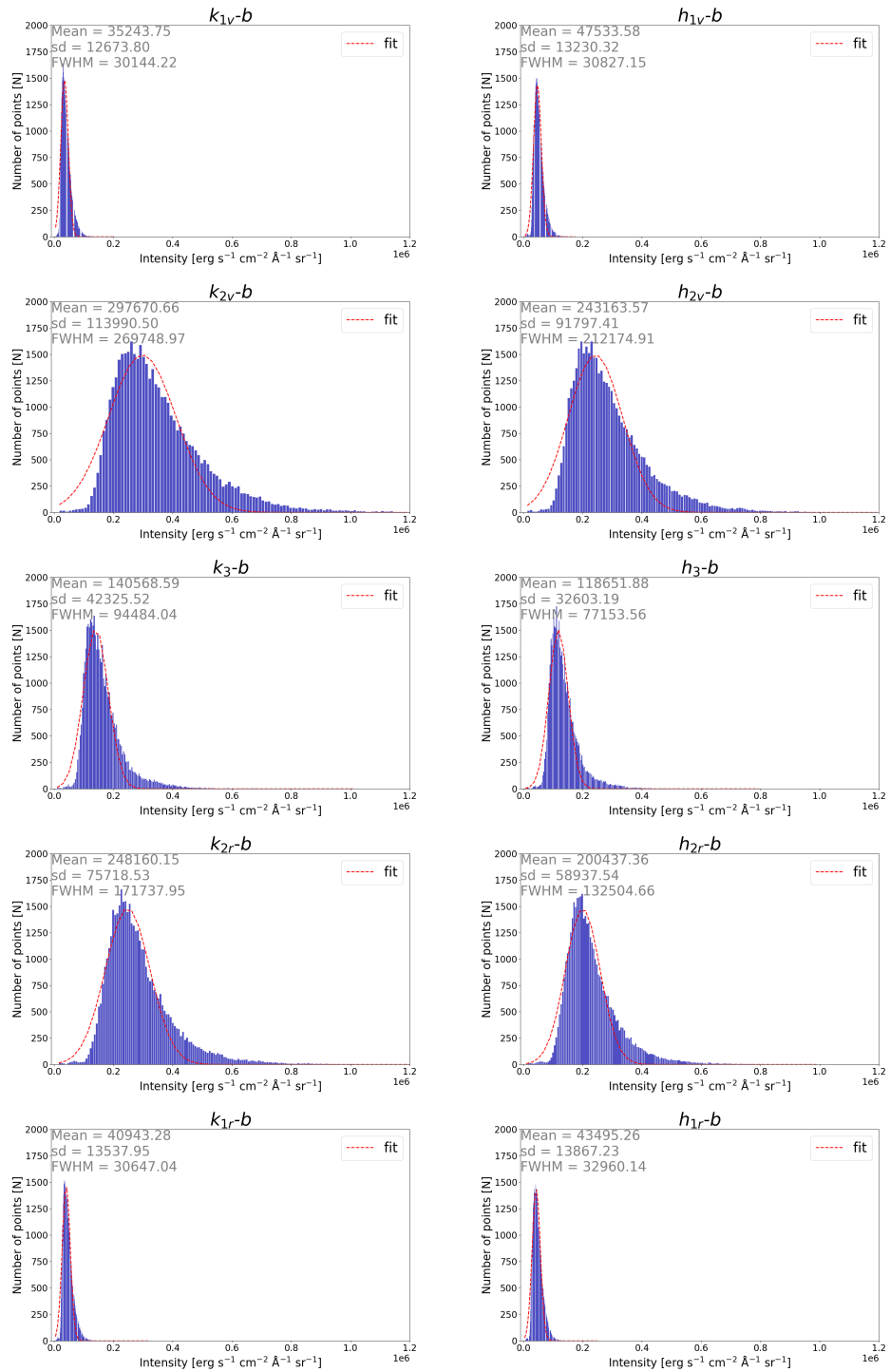


Figure 2.24: Intensity histograms for the profile features of Mg II h&k lines in one raster as obtained by IRIS on July 23, 2019. The dashed red line represents the Gaussian distribution. The legend at the top left for each panel shows the mean, the standard deviation, and the width of the distribution.

In the next Chapter, we will investigate the temporal variation of the averaged flux for all Mg II h&k features over the time period 2015-2022 representing the end of the 24th and the beginning of the 25th solar cycles. We also will investigate the relationship between radiation temperatures, total integrated intensities, and line widths, as well as their relationship to feature intensities for all Mg II h&k lines.

Chapter 3

Variation over the Solar Cycle of the h and k Lines at the Quiet Sun Centre

Within the near-ultraviolet (NUV) range of IRIS, the Mg II h&k lines are robust chromospheric indicators that enable precise assessments of velocity and temperature across a range of chromospheric altitudes. Previous investigations have explored correlations between these physical parameters and distinct Mg II features, each associated with a specific altitude (see Table 4 in [Pereira et al. \[2013\]](#)). The h and k lines have a common origin, although the k line's oscillator strength is twice that of the h line ([Pereira et al. \[2013\]](#)).

[Gunár et al. \[2022\]](#) published one of the most recent studies on the variation of periodic illumination from the Sun's surface and its effect on the Mg II h and k spectra emitted from chromospheric and coronal structures. They examined how alterations in the incident radiation within the Mg II h&k lines impact the spectra computed using models of radiation transfer in prominence-like plasmas. Their findings revealed two key factors affecting the generated Mg II h&k spectra. The first factor involves shifts in the incident radiation, which are essential for prescribing simulated plasma illumination originating from the solar disc. The second factor relates to the presence of line-of-sight dynamics within their multi-thread configuration.

In this chapter we investigate the temporal variation of averaged flux taken at the centre of the solar disc for all Mg II h&k features in the period 2015 to 2022. This period represents the end of the 24th and the beginning of the 25th solar cycle and is therefore a transitional phase. Additionally, we examined the relationship between radiation temperatures, total integrated intensities, line widths, and their connections to feature intensities across all Mg II h&k lines. Section 3.1 gives an overview of the solar cycle and how it relates to chromospheric activity. Section 3.2 presents an analysis of the variations in the Mg II h&k lines throughout the solar cycle. Section 3.3 describes the data reduction process, and section 3.4, the algorithm used for this analysis. In Section 3.5 some of the diagnostic information embedded in the Mg II h&k lines is discussed, temperature, total integrated intensity, line width, and temporal variation.

Section 3.6 discusses the findings, with Section 3.7 providing a concise summary of the work and the conclusions drawn from the results.

3.1 Overview of Solar Cycle and Its Influence on Chromospheric Activity

The solar cycle is a periodic variation in solar activity that lasts approximately 11 years. The Sun undergoes alternating phases of reduced solar activity (solar minimum) followed by heightened solar activity (solar maximum). The cycles are accompanied by characteristic waxing and waning of solar phenomena such as sunspots, solar flares, and solar prominences (see e.g., [Hathaway \[2010\]](#)). Sunspots are well-known characteristics of solar activity, visible as darker regions on the sun's surface (photosphere) where the magnetic field is concentrated. The solar cycle plays a pivotal role in influencing the behaviour of the Sun's atmosphere, particularly the chromosphere, which lies between the photosphere and the corona, and is a transitional region crucial for understanding the energy transfer mechanisms from the Sun's interior to its outer atmosphere. Solar prominences are another form of chromospheric activity influenced by the solar cycle. These are large loops of magnetic fields filled with relatively cooler plasma, and appear as bright structures against the solar disc or as dark filaments when observed at the limb of the Sun ([Tandberg-Hanssen \[1995\]](#)). The influence of the solar cycle on the chromosphere has consequences for space weather and consequently for the Earth. Solar flares and other chromospheric activities can lead to geomagnetic storms, affecting satellite operations, power grids, and even causing the auroras (Northern and Southern Lights) to be more vivid as well as frequent ([Gonzalez et al. \[1994\]](#)). Solar Cycle 24 began in December 2008, peaked in April 2014, and ended in December 2019, while Solar Cycle 25 commenced in December 2019 ([Li et al. \[2015\]](#)), with its peak projected in 2025 ([Prasad et al. \[2022\]](#)).

Our study predominantly focuses on the large-scale structure by averaging all the pixels for each raster file, thereby giving a perspective that is primarily relevant to the quiet Sun at the disc centre over solar cycles. It is correct that individual datasets capture the variance in solar structures. The distinction between network and internetwork regions and their random mixture may be important, depending on the specific objectives of the analysis being carried out. However, the methodology we adopted emphasises average behaviour, making our results more representative of the quiet Sun. This means that variations on a finer scale, and the interactions between the network and internetwork, might not be as prominently reflected in our conclusions. When interpreting our findings, it is essential to bear in mind that our focus is on average behaviour and the large-scale structure. Future studies will delve deeper into these finer-scale variations to provide a more detailed understanding.

3.2 Analysis of Mg II h&k Line Variations over the Solar Cycle

The Mg II h&k lines correspond to wavelengths of 279.6 nm and 280.3 nm respectively, and serve as valuable spectral indicators for studying variations in solar activity over the solar cycle and originate from the chromosphere. The Mg II h&k lines are sensitive to both thermal and magnetic conditions in the chromosphere, making them particularly useful for investigating the complexities of solar behaviour (Leenaarts et al. [2013b]).

During solar maxima sunspots are abundant and often accompanied by brighter regions known as plages, where magnetic activity is concentrated and thus implying intense chromospheric activity. The Mg II h&k lines are often enhanced in plages, indicating higher temperatures and increased magnetic activity (Fontenla et al. [2016]). During less active phases, the Sun's magnetic field is less complex, and chromospheric activity is present at lower levels. Increased temperatures typically lead to higher intensities; however, an excessively high temperature can paradoxically decrease this intensity. This phenomenon is particularly observable in plages, where the temperature range facilitates an augmentation in the population of Mg II ions in their optimal energy states. Such a condition enhances the emission strength of photons in the h and k lines. The chromosphere plays a significant role in coronal heating, a process still only poorly understood. What is known is that the exchange of energy between the chromosphere and the corona varies throughout the solar cycle, affecting the temperature and density of the corona.

3.3 Data Reduction

IRIS FITS files are categorized into four groups based on the level of data postprocessing, and our current emphasis is on Level 2 FITS files. Managing an overwhelmingly large dataset within the rapidly expanding universe of big data is daunting, especially in complex fields that require precision and sophisticated understanding. Our dataset covers the period from 2015 to 2022, consisting of raster files that serve as digital snapshots, capturing specific variables for each day of the year, resulting in 365 raster files annually. Each raster file contains over 9×10^4 profiles, with more than 4.5×10^4 assigned to each h and k line. Particular emphasis has been placed on the IRIS OBS-ID for the daily QS monitoring A1, which is 3882010194 (see Fig. 3.1). The magnitude of this data poses significant challenges for effective analysis and interpretation. While storage simply requires more space and more efficient memory structures, drawing meaningful conclusions from the complexity of the raw data is challenging without some form of data reduction. This is a strategic process designed to transform this enormous repository of information into something amenable to analysis without losing information crucial for accurate interpretation.

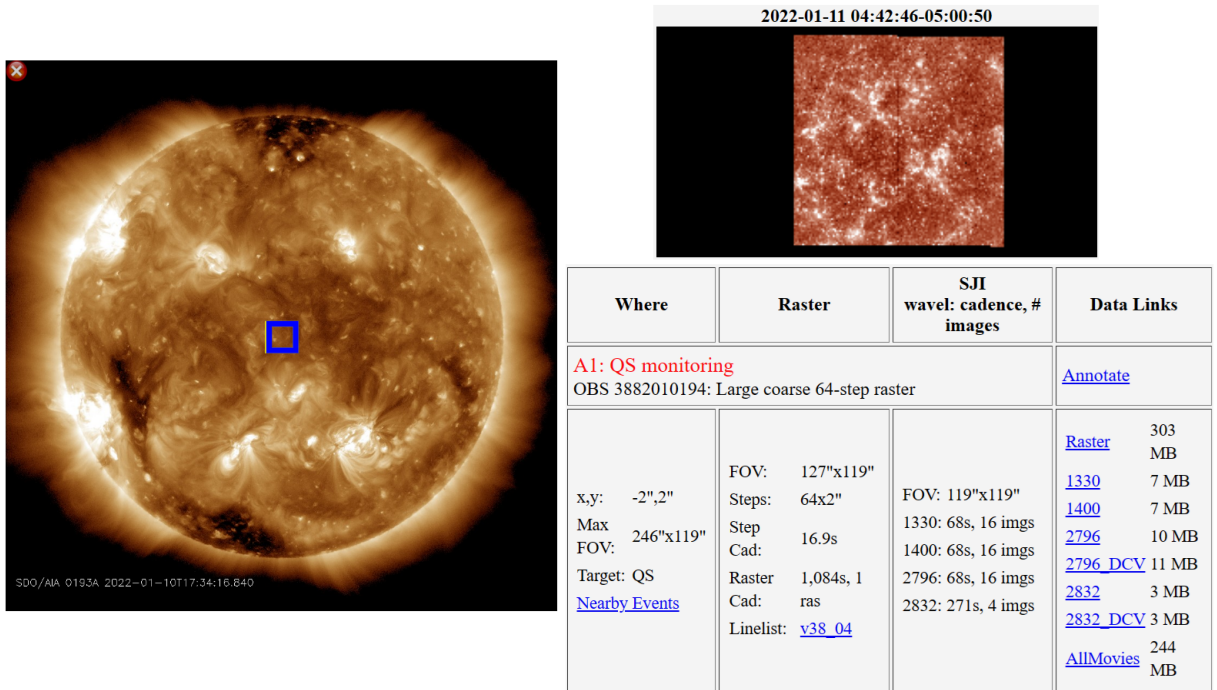


Figure 3.1: An SDO/AIA image of the sun shows a detailed view of the sun’s surface on January 11, 2022, with a highlighted blue box indicating the targeted area for the slit jaw raster image. Accompanying information includes observational details, raster data, dimension of raster, step cadence, and the FOV.

The data reduction process starts with the elimination of 'bad pixels', defined as those with either zero or negative intensity values. These bad pixels add to the noise in the data, obscuring meaningful signals and making it increasingly difficult to isolate relevant information. Once these are excluded the pixels for each h and k line are averaged (the average here is a process that combines all pixel values across a whole raster, producing one spectrum per day), effectively condensing the information contained in the individual pixel data points to a single average value for each line, thereby simplifying the overall structure without sacrificing the essential characteristics of the dataset. This results in dual (h and k) line profiles for each raster file. These line profiles represent the averaged over the FOV (averaged in spatial domain) valid data, providing a streamlined version of the original raster files that can be more easily manipulated and analysed. Given our specific interest in tracking temporal variations in the line profiles at the centre of the Sun, any loss of spatial resolution does not compromise the soundness of this approach.

3.4 Description of the Algorithm

The algorithm is designed to deal with the large data set spanning eight years, from March 1, 2015, to August 9, 2022, as described in Sec. 3.3. The algorithm is designed to address the

9×10^4 profiles in each raster file, each of which represents a single day's worth of data. The algorithm calculates two reduced profiles for each raster file (one each for the h and k lines). This data reduction is effective enough to obviate smoothing of the averaged data, a process that was used in Sec. 2.3 when analysing single raster files. However, this approach lacks utility when the objective is to investigate spatial variations of the spectral lines. Addressing the challenge of processing a vast number of profiles across the entire period requires a meticulous approach to data handling and analysis. This process begins with the invocation of FITS files, each containing valuable spectral information, including the intensities for both the k and h lines. To ensure the integrity and accuracy of the data, the first step of the method involves excluding bad pixels, which often occur at the beginning and end of each file, thereby preventing them from skewing the results. Following the cleansing of the data, an averaging function is applied to the remaining valid pixels to synthesise the information into an (average) intensity value that is representative of each line. This procedure is applied to all years, with each raster file corresponding to a one-line profile per day.

While analysing the IRIS Mg II h&k quiet sun data at the disc centre spanning the entire IRIS mission, we encountered a calibration issue with the IRIS data. A perplexing dip in the intensity of the h and k lines was observed around January 1, 2022. After reaching out to the IRIS team with our concerns regarding the potential intensity calibration issue, it was identified that there indeed was an issue with the calibration. Thankfully, this was recently addressed by the IRIS team. Consequently, the latest radiometric calibration data and routine (`iris_get_response.pro`) in SSW were updated on May 26, 2023.

3.5 Mg II h&k Lines Diagnostics

The Mg II h&k lines serve as an invaluable diagnostic tool for assessing and interpreting many chromospheric properties, thereby understanding of the solar chromosphere's underlying behaviour. These lines are integral to the study of factors such as temperature fluctuations, total integrated intensities, line widths, and temporal changes across different scales.

In this section, we discuss the relation between the radiation temperatures, the total integrated intensities, and line widths, as well as their relation to each spectral feature. we only present results for the k line as results for the h line are very similar. we reduced the volume of data by averaging all the pixels ($\sim 9 \times 10^4$ pixels) for each of the 2644 raster files (these represent the number of days observed during 8 years, which is the entire target period) to produce separate profiles for h and k. The results presented here are mostly relevant to the quiet sun at the disc centre (not filtering out brighter regions) .

3.5.1 Temperatures

Understanding the intricate relationship between gas temperature and radiation temperature in the solar chromosphere is crucial for unraveling the mysteries of the Sun's dynamic atmosphere. In a study by [Pereira et al. \[2013\]](#), 3D radiative magnetohydrodynamic simulations of the solar atmosphere were used to explore this relationship, with a particular focus on synthetic Mg II h and Mg II k line profiles. This investigation sheds light on the temperature dynamics of the middle chromosphere, where the k_2 and h_2 peaks are formed, and how radiation temperature can serve as a proxy for gas temperature in these regions, provided an absolute calibration of the IRIS spectra is performed.

The Planck function describes the spectral radiance of electromagnetic radiation at all wavelengths from a black body at a given temperature. We use the Planck function to describe the intensity of h_2 or k_2 because these spectral features can be approximated to form under conditions close to LTE, where the source function couples to the local gas temperature via the Planck function.

One fundamental aspect highlighted by [Pereira et al. \[2013\]](#) is the challenge associated with using the line cores' intensities to infer gas temperatures. This limitation arises from the deviation of the source function in the line core from the Planck function. However, in the middle chromosphere, where the k_2 and h_2 peaks emerge, a stronger coupling between gas and radiation temperatures is observed. This observation forms the basis of the study's main finding that radiation temperature gives an accurate estimation of the gas temperature at the heights where the k_2 and h_2 peaks are formed. This insight can significantly enhance our understanding of the solar chromosphere's thermal structure.

The temperature sensitivity arises due to the dependence of atomic level populations on temperature, following the Boltzmann distribution. Observations of these lines can thus provide important temperature diagnostics for the chromosphere, which has approximate temperatures ranging from 4100 K (see [Avrett \[1995\]](#)) to peaks of 25,000 K in some regions. Models by [Leenaarts et al. \[2013b\]](#) detail how the line profiles change with temperature, thereby enabling precise profile-to-temperature mapping.

The series of studies published in IRIS papers by [Leenaarts et al. \[2013a,b\]](#), [Pereira et al. \[2013\]](#), highlight that in the middle chromosphere, the source function remains linked to local atmospheric conditions, allowing the intensity of k_2 or h_2 peaks to be transformed into radiation temperature. This is based on the understanding that the source function aligns with the Planck function under the conditions of blackbody radiation and LTE. The direct relationship between peak intensities and temperature was further validated by research findings from [Leenaarts et al. \[2013b\]](#). Consequently, we used the Planck function given below to calculate the middle chromosphere's radiation temperature

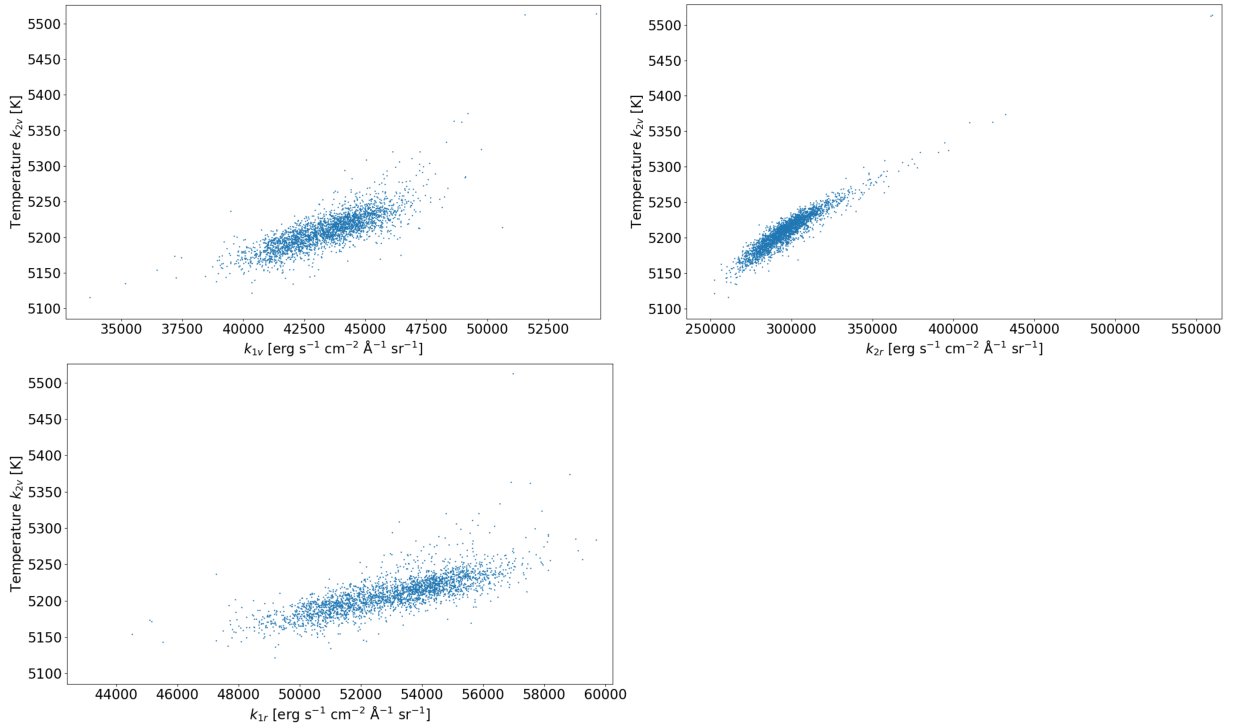


Figure 3.2: Scatter plots of the relationship between the temperature for k_{2v} peak intensity (K) and intensities at all spectral features ($\text{erg s}^{-1} \text{cm}^{-2} \text{\AA}^{-1} \text{sr}^{-1}$).

$$T = \left(\frac{hc}{k\lambda} \right) \left[\ln \left(\frac{2hc^2\lambda^{-5}}{I_\lambda} + 1 \right) \right]^{-1} \quad (3.1)$$

Here λ represents the wavelength corresponding to k_{2v} or h_{2v} (2796.35 or 2803.53 \AA), I is the intensity associated with k_{2v} or h_{2v} , h denotes Planck's constant, k stands for Boltzmann's constant, and c represents the velocity of light. This equation allows for the estimation of radiation temperature, a key step in evaluating the middle chromosphere's thermal conditions.

Figure 3.2 provides a visual representation of the relationship between temperatures and the intensities of spectral features. Temperatures are obtained by applying the peak intensities detected by the algorithm to the Planck function. While some scatter is observed in k_{1r} and k_{1v} , there is a strong correlation between temperature and intensity for k_{2r} . These correlations help us estimate the temperature at the middle of the chromosphere, where the k_2 and h_2 peaks originate. This knowledge assists in comprehending the intricate thermal dynamics within the solar chromosphere.

The scatter plots in Fig. 3.3 show how the temperature for k_{2v} changes over time. They show that the averaged solar flux remains consistent during the period from the 24th to the 25th solar cycle. Despite this overall stability, fluctuations were observed in 2015 and 2016, coinciding with the decline of peak solar activity.

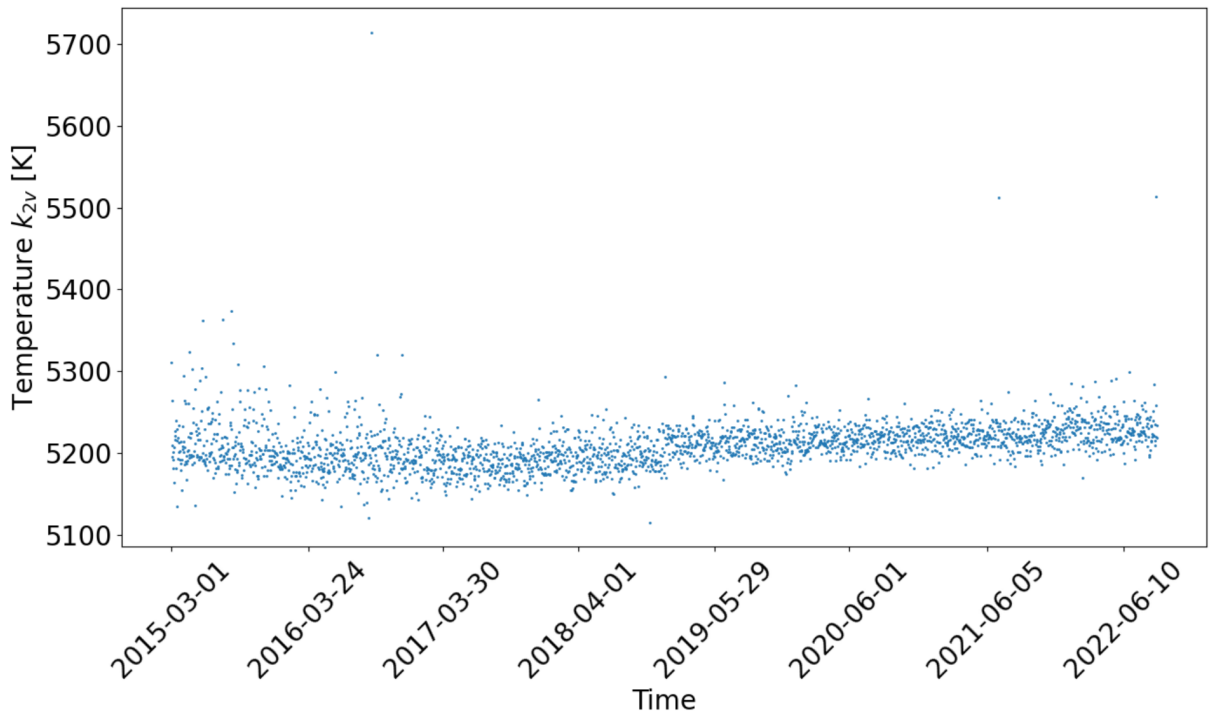


Figure 3.3: The variation of the middle chromosphere’s radiation temperature for the period 2015-03-01 to 2022-09-08.

3.5.2 Total Integrated Intensities

Unlike more complex approaches, such as line profile analysis, which can yield higher-resolution details about the atmospheric structure and dynamics, focusing on integrated intensities simplifies the computational models.

The quiet Sun is a region that encompasses many distinct phenomena. Our goal was to understand the complexities of this region as a whole without distinguishing between the different phenomena involved. In pursuit of this goal we have chosen to focus on one essential parameter: the total integrated intensity. Our objective is to unravel the connection between this parameter and specific spectral features, particularly k_1 , k_2 , and k_3 , to gain insights into the behaviour of the quiet Sun. At this stage we do not differentiate between the distinct phenomena within the region, such as the network and internetwork phenomena, opting instead to consider the total integrated intensity for each raster file as our primary metric. This is illustrated in Fig. 3.4 which shows the correlations between feature intensities and the total integrated intensity for all spectral features.

Figure 3.4 shows the strong correlation between the intensities of all spectral features (k_1 , k_2 , and k_3) and the total integrated intensity. This correlation is particularly pronounced in the case of k_{2v} , k_3 , and k_{2r} . These findings suggest that these specific spectral features are closely tied to the total integrated intensity, which further suggests that they indicate underlying processes that

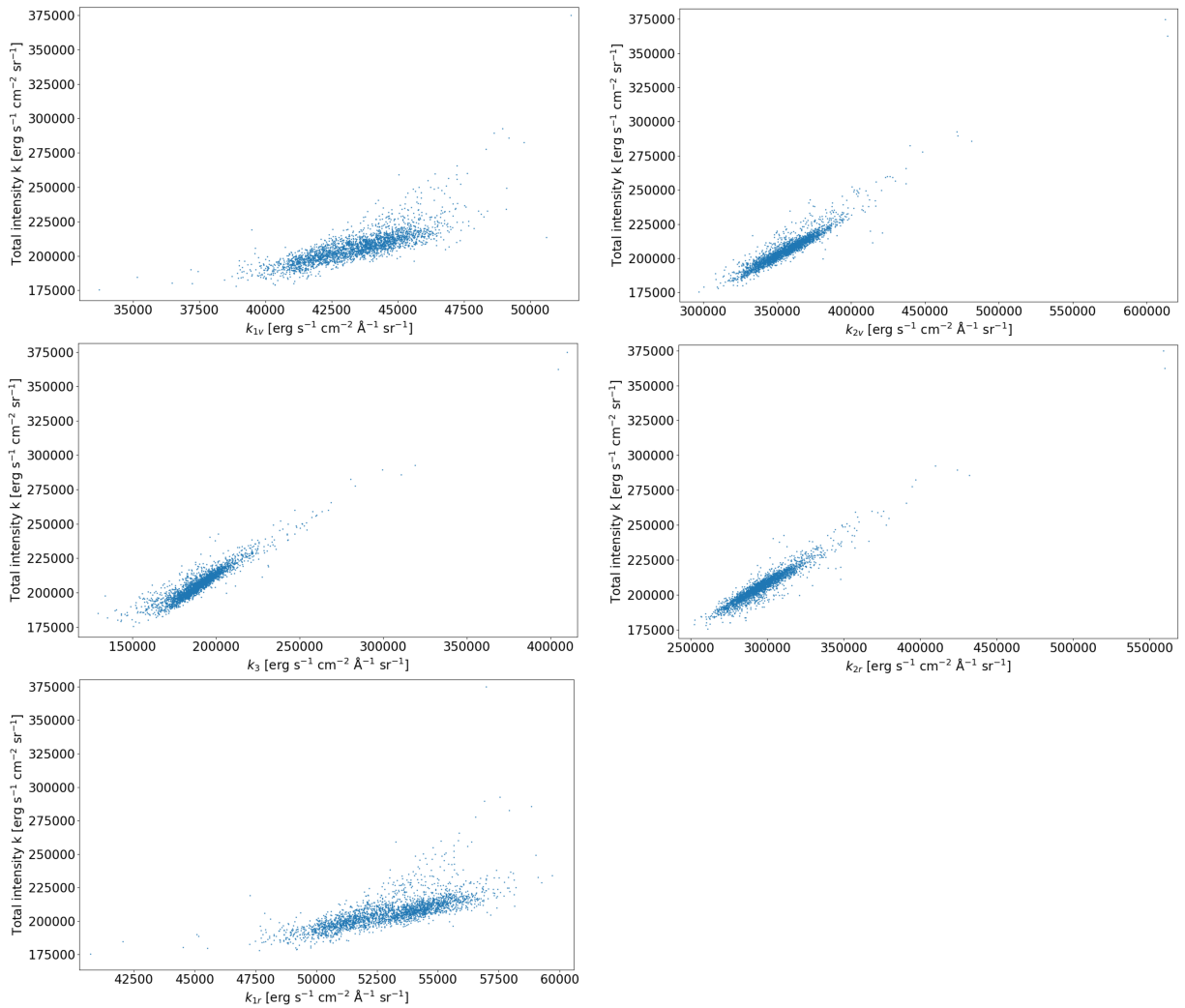


Figure 3.4: Scatter plots of the relationship between the total integrated intensity and the intensity of each spectral feature.

have a significant contribution to the total energy emitted by this region of the Sun.

While results presented Figs. 3.4 and 3.2 show robust correlations, it should be remembered that contributions to the total integrated intensity come from many sources, including network and internetwork processes. Further investigation is needed to separate out the individual contributions from the underlying processes.

3.5.3 Cumulative Sum of the Intensity

The cumulative sum of the intensity is a running total of intensity values across a dataset. This method sequentially accumulates the intensity values from one spectrum end to the other, displaying a sum of the intensity at each point that has been accrued from the beginning to that specific point. This can help reveal how the intensity is distributed across different parts of the line. In this work, the term is used to describe the cumulative distribution of intensities across

the different contributing wavelengths (see Fig. 3.5).

We used the function given below to calculate the cumulative sum of the intensity

$$I_{tot} = \sum_{i=0}^{i=N-1} \left((\lambda_{i+1} - \lambda_i) \cdot \left(\frac{1}{2} \right) \cdot (I_{i+1} + I_i) \right) \quad (3.2)$$

Where λ_i and λ_{i+1} are the wavelengths at the i^{th} and $(i+1)^{\text{th}}$ positions, respectively. I_i and I_{i+1} are the intensity values corresponding to the wavelengths λ_i and λ_{i+1} , respectively.

The procedure involves integrating the intensity across all wavelengths, and then determining what fraction of the total intensity lies below any particular wavelength. The cumulative sum of the intensity is used in the analysis of the Mg II h&k lines to quantify their variation with time, either through direct observations or via synthetic spectra generated from models.

Figure 3.5 shows an example line profile for the Mg II k line and its corresponding cumulative sum of the intensity, which plots the cumulative intensity against wavelength to show how much of the total intensity comes from a particular range of wavelengths. It therefore reflects the underlying distribution of the wavelengths in the spectrum. The wavelengths corresponding to the 12% and 88% levels on the cumulative sum of the intensity were identified, which allows us to compare this with the FWHM of a Gaussian line profile.

3.5.4 Line Widths

One important parameter in the diagnosis of plasma conditions using the Mg II h&k lines is the line width. The line width is affected by many factors including thermal motions, non-thermal velocities, and pressure broadening, and therefore summarises the contributions from many different underlying physical conditions (Jejčić et al. [2017]). Line width diagnostics on the Mg II h&k lines are typically performed through spectral fitting procedures. Increasingly detailed radiative transfer simulations (e.g., Pereira et al. [2013]) have significantly advanced our understanding of how these lines are formed. This has enabled more sophisticated modeling and more accurate diagnoses of the underlying solar processes the lines and their individual features indicate.

Beside the temperature and the total integrated intensity information, we used the quantile method to calculate the line width. To do this, we first calculated the total integrated intensity, then found the wavelength values corresponding to the total intensity values at 88% and 12% of the total integrated intensity. The difference between the two wavelength values is taken as a representation of the line width. In the case of a purely gaussian profile, this measure is equivalent to the theoretical FWHM (Ruan et al. [2018]). Figure 3.6 demonstrates that the width of the Gaussian profile accurately corresponds to the standard FWHM. We used the cumulative

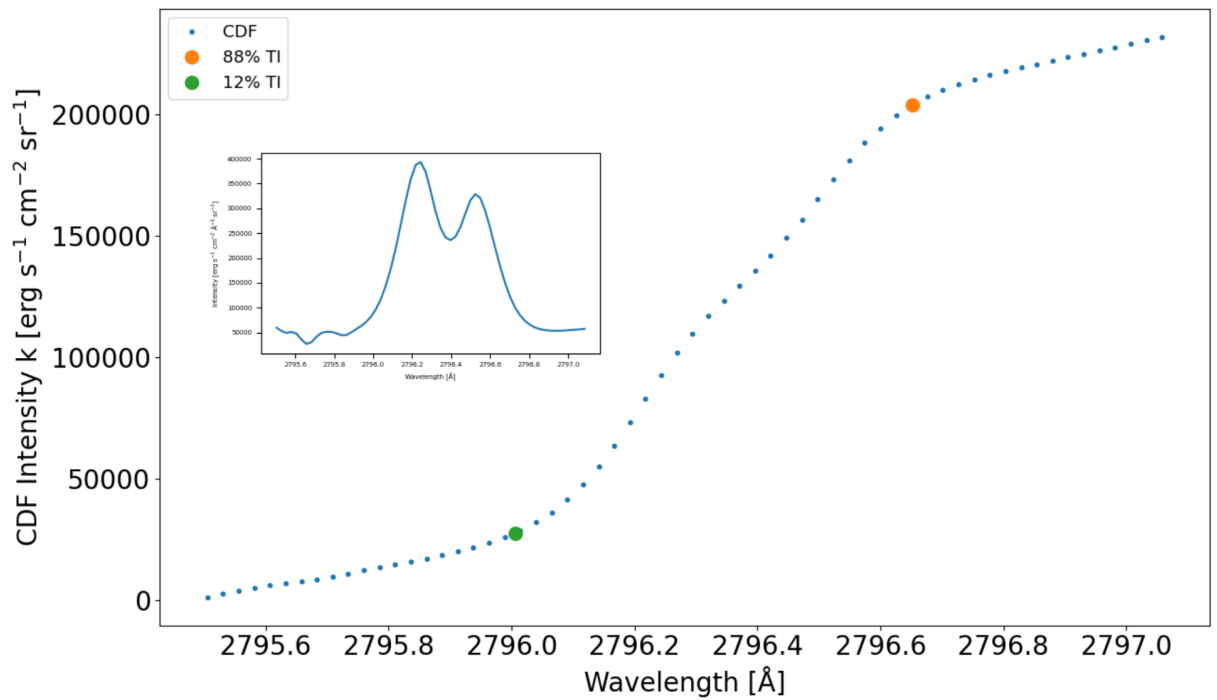


Figure 3.5: An example of a cumulative intensity distribution for the k line intensity. The green and orange points correspond to the wavelength at which 12% and 88% of the total intensity have been accounted for. The small panel represents the Mg II k line profile, taken from the averaged raster obtained on September 12, 2015, corresponding to the presented cumulative sum of the intensity.

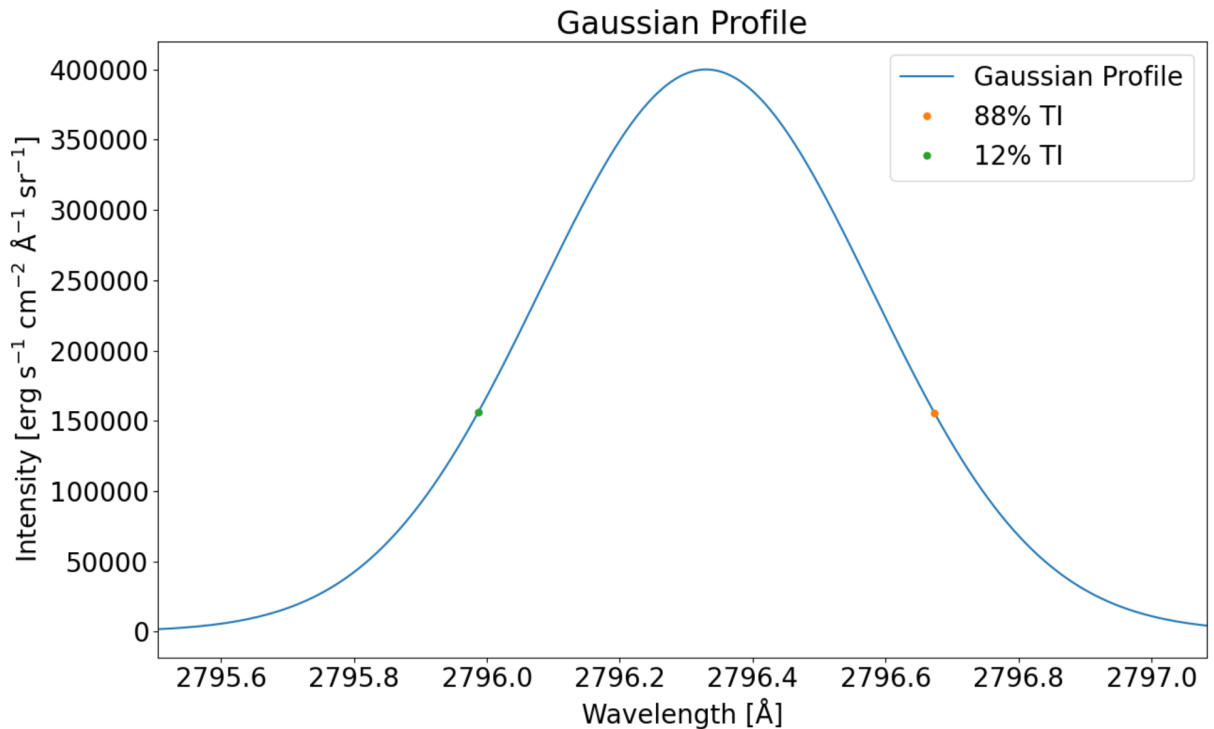


Figure 3.6: A theoretical Gaussian profile demonstrates the precision of the quantile method that determine the full width at half maximum. By identifying the positions at the 12% and 88% intensity points marked in green and orange, respectively.

sum of the intensity to find the total integrated intensity, and the linear interpolation function to find the wavelength values that correspond to 88% and 12% level of the cumulative sum of the intensity.

The relationship between the line width and k_{2v} , k_3 and k_{2r} shows an inverse correlation, while there is no correlation with k_{1v} and k_{1r} intensities (see Fig. 3.7). A likely explanation for the lack of correlation between line width and intensities in k_{1v} and k_{1r} is that the line width is primarily determined by the line profile shape and intensity at wavelengths where the line formation processes are different from what is happening at those positions in the wings. The bottom-right panel in Fig. 3.7 also shows that there is an inverse correlation between the line width and the total intensity for the k line. The observed broadening of the line width to increase with increasing intensity does not seem to be temperature-dependent. Instead, it seems that the measurements at lower intensities are predominantly influenced by noise rather than by a reliable correlation.

3.5.5 Temporal Variations

In this section, we review the variation of the averaged flux of the quiet Sun at the Sun's centre over the period from 2015 to 2022, which marks the end of Solar Cycle 24 and the beginning of Solar Cycle 25. Here, we examine the relationships between the feature intensities of Mg II

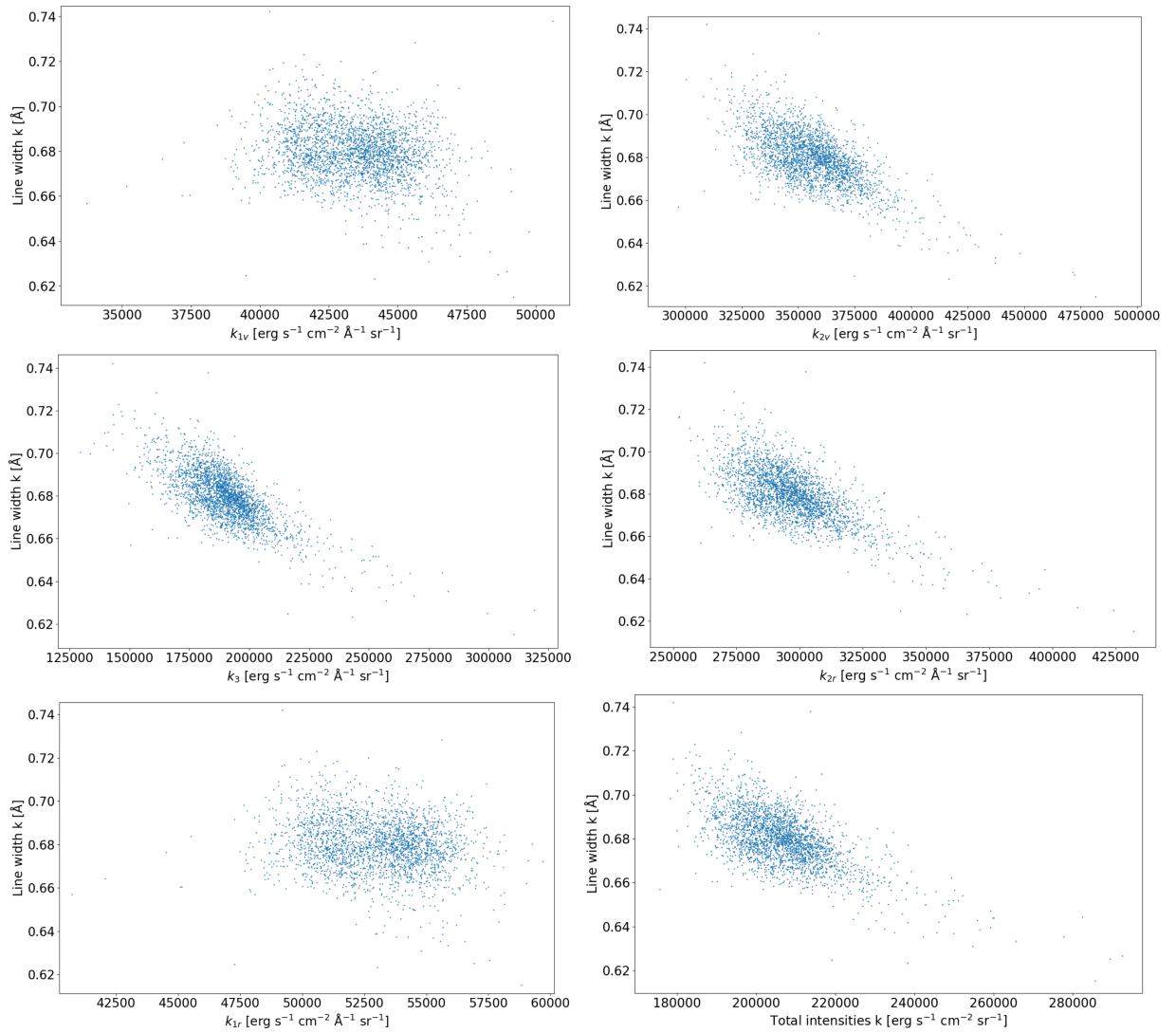


Figure 3.7: Scatter plots of the relationship between the line width and all spectral features in intensity. Bottom-right panel: Scatter plot of the relation between the line width and the total integrated intensity for the k line.

h&k lines for all spectral features and time. We also investigate the relationships between time and the ratio of total intensity for k over h.

The quiet Sun is a useful baseline or reference point for understanding solar activity since it is a region devoid of significant solar disturbances. To assess changes in the quiet Sun's behaviour, we examined the averaged flux at the Sun's center. The scatter plots in Fig. 3.8 show that the averaged flux is stable throughout the end of the 24th solar cycle and the beginning of the 25th solar cycle, although there is some scatter in 2015 and 2016 since this period was the end of the maximum solar activity. In Figure 3.9, the scatter plot shows that the ratio of the total intensity for k over h is also stable throughout the period. Also, the ratio is more scattered in 2015 and 2016. In general, little activity in that region, although in 2015 and 2016 at the end of solar max it could be expected that there will be more variations. Figure 3.8 also shows the intensities k1v and k1r exhibit so little variation over years and then noticeably jump around January 2019 and then return to remain a little variation over remained years. This jump seems puzzling and raises curiosity about its causes. Could there be an issue with the calibration? Perhaps like the ones we encountered at the beginning of the IRIS data analysis, as we mentioned in Sec. 3.4.

Our findings are good for understanding how these features evolve during the transition from one solar cycle to the next, although the task has computational complexity. Each raster profile took approximately two minutes to process, making it necessary to allocate around four days to analyse the entire dataset.

3.6 Discussion

The Mg II h&k lines' fundamental formation characteristics in the solar atmosphere exhibit a complex formation behaviour that extends from the upper photosphere to the upper chromosphere. There is a wide range of resulting line shapes due to the differences in temperature, density, and velocity in this region, and due to how changes in solar activity over time affect different layers of the solar atmosphere in different ways.

In this work, we were able to build an efficient algorithm that can accurately deal with double-peak profiles. Our algorithm is able to determine the position of spectral features of the Mg II h&k lines (the outer minimum in the wings, emission peaks, and central absorption core) with great accuracy, according to a set of rules (see Sec. 2.3). Our algorithm determines the outer minimum in the wings (k_1/h_1) in addition to the emission peaks (k_2/h_2) and the central absorption peaks (k_3/h_3). The algorithm works well for the Mg II h&k spectrum that forms in the photosphere and the chromosphere at the Sun's centre. Each Mg II h&k line has a central absorption core between two emission peaks, with outer minima flanking both. Our algorithm excludes profiles that have a single peak. Therefore, it will work with any line profile in any

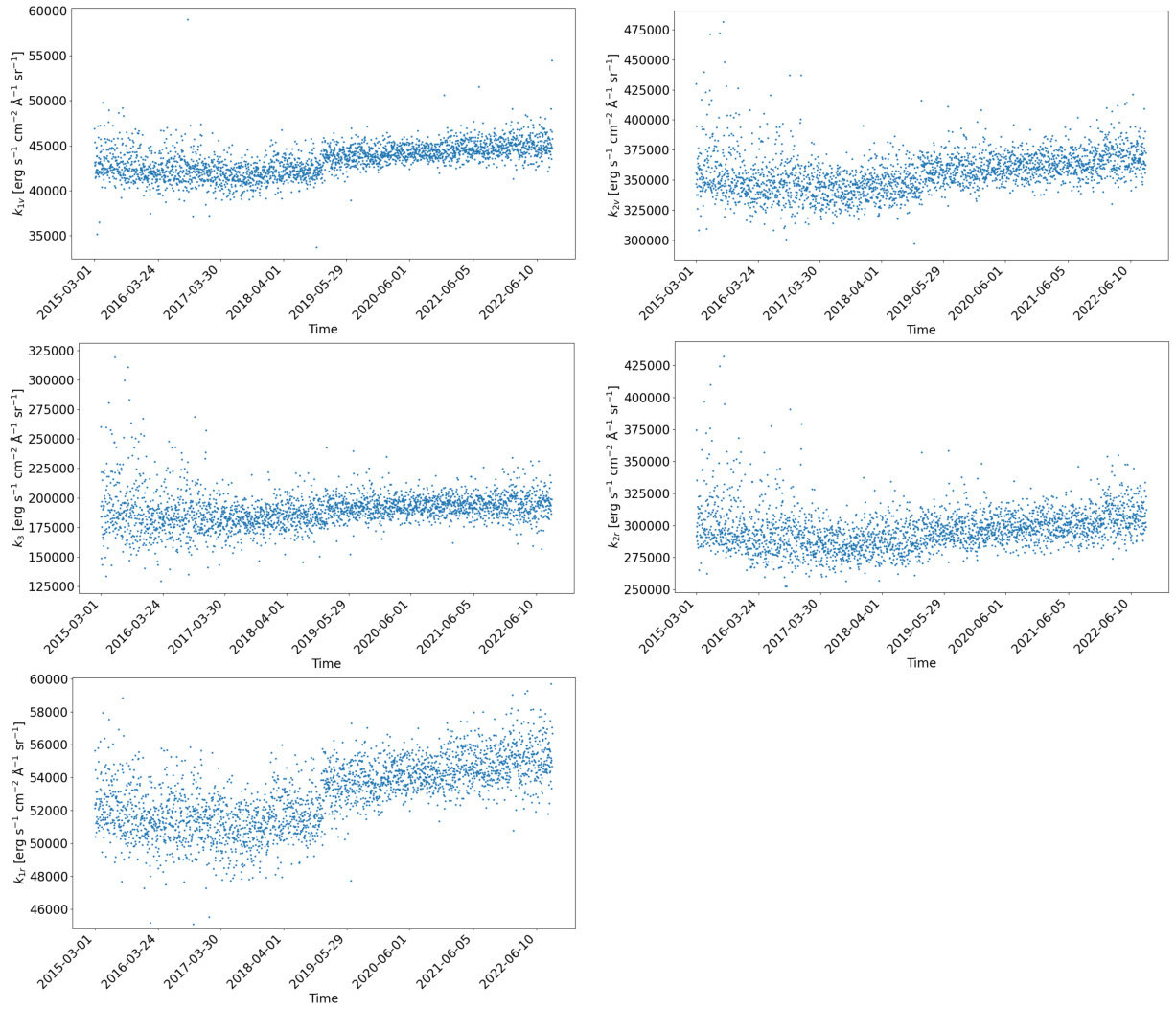


Figure 3.8: The variation of intensities for all Mg II k features for the period 2015-03-01 to 2022-09-08.

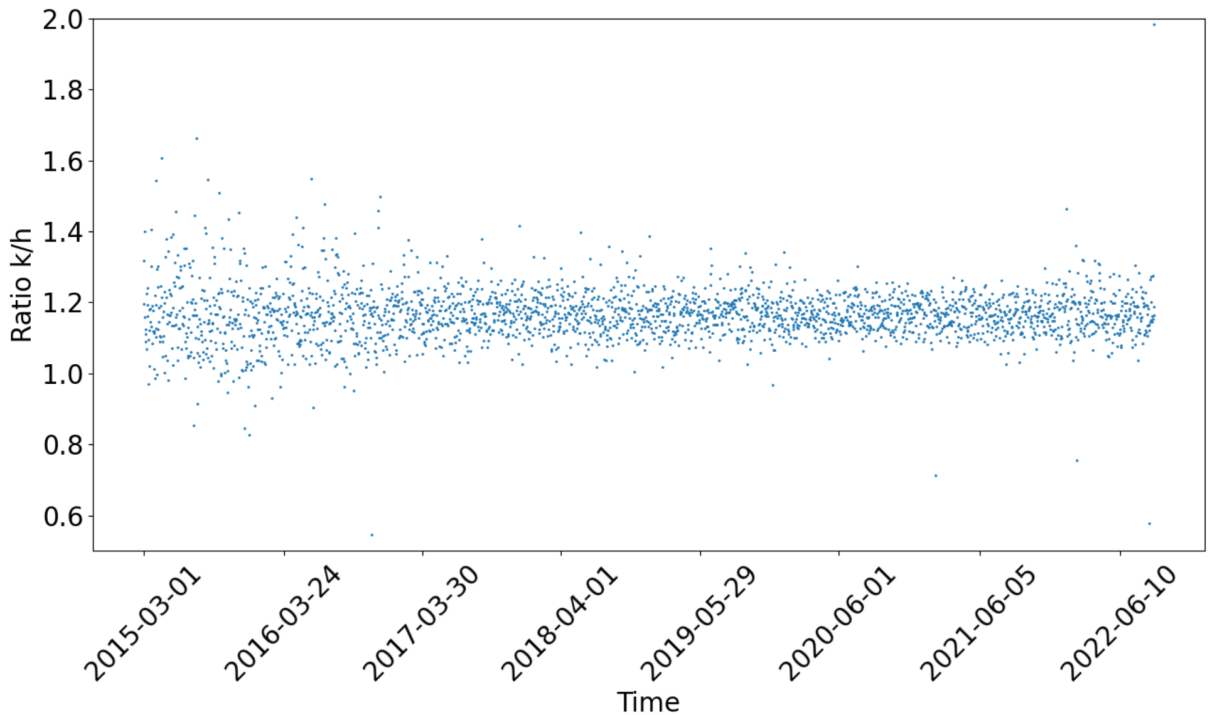


Figure 3.9: Scatter plot of the relation between the ratio of the h and k total intensity for the period 2015-03-01 to 2022-09-08.

region of the Sun if it has a similar shape with two emission peaks, a central absorption core, and well-defined minima on either side of the line profile.

As noted by [Pereira et al. \[2013\]](#), a constraint on the minimum temperature of the gas is provided by the radiation temperature of the k_2 or h_2 peaks. The temperature we obtain from peak intensity at k_{2v} and the feature intensities for all spectral features, especially k_3 and k_{2r} , are strongly correlated, as shown in Fig. 3.2. There is a correlation between peak intensities and the temperature of the atmosphere at their $\tau = 1$ peak heights. The temperatures we found are less than 6000 K; these findings are consistent with those of [Pereira et al. \[2013\]](#), who found a correlation between the radiation temperature (T_{rad}) and the gas temperature (T_{gas}), even though there is more scatter at temperatures below 6000 K. While the radiation temperatures in their work cover a much broader range, but their investigation spanned a broader temperature range as they were examining the entirety of solar chromospheric phenomena in their simulation.

In the study by [Pereira et al. \[2013\]](#), it was found that while the source function at the k_3 and h_3 cores of these lines is decoupled from local atmospheric conditions, indicating independence, there remains some level of coupling to these conditions at the k_2 and h_2 levels situated in the middle chromosphere. This relationship allows the conversion of the intensity at these peaks into radiation temperature, serving as an effective proxy for gas temperature at their formation heights. The conversion process is straightforward for synthetic spectra but requires absolute calibration for IRIS data. The study also indicates that instrumental smearing has a minimal effect on the correlation between measured and actual temperatures, mainly affecting extreme

intensity values above 7 kK, with the correlation at the k_{2r} peak being slightly more influenced due to the narrower range of T_{rad} .

To further understand the details of solar spectra and what processes are responsible for their formation, we analysed the line widths of the spectral profiles. Examining the contribution of wavelength ranges with the quantile method, as described in Sec. 3.5.4, we investigated the relationships between line width values and spectral feature intensities. Figure 3.7 illustrates our findings and shows the patterns and correlations observed for line widths and spectral feature intensities. Of note is the concentration of line widths between 0.64 and 0.72 Å. One of the most significant observations is the negative correlation between line width and the intensities of the spectral features k_{2v} , k_{2r} , and k_3 . As line width decreases, the intensity in these spectral features tends to increase. This inverse relationship suggests that narrower lines are associated with more prominent spectral features, highlighting the intricate relationship between line width and spectral feature intensity. In contrast, no correlations were observed between line width and the intensities at k_{1v} and k_{1r} . One plausible explanation for this lack of correlation lies in the spatial distribution of features in the outer wing. The outer wing features, represented by k_{1v} and k_{1r} , are located at positions that may fall outside the bounds of the line profile itself.

3.7 Summary and Conclusions

This preliminary analysis of all quiet Sun rasters at disk center obtained between 2015 and 2022 demonstrates there is a wealth of information that can be obtained from the complex Mg II line profile shapes by studying their key features automatically. Our research examined key features of these complex line profiles and found both correlations and temporal variations. Our primary objective was to explore the intricate relationships between radiation temperatures, total integrated intensities, line widths, and spectral feature intensities in the solar chromosphere.

We found that the temperature correlates strongly with k_3 & k_{2v} intensities, but the correlation with k_{1r} & k_{1v} intensities shows more scatter. The total integrated intensity and the feature intensities for k_{2v} , k_3 , and k_{2r} are well correlated. There is no relationship between k_{1v} & k_{1r} and the line width, but the line width has an inverse relationship with k_{2v} , k_3 , and k_{2r} intensities. We also investigated the temporal variation of Mg II h&k lines between the end of the 24th and the beginning of the 25th solar cycles. We found that at this period, the averaged flux remained constant.

In the next chapter, We will focus on mosaic observations to study the centre-to-limb variations of the spectral line features by applying our algorithm to the whole Sun's disc.

Chapter 4

Mosaic Observations

The Interface Region Imaging Spectrograph (IRIS) is one of the most advanced tools for advancing our comprehension of the solar atmosphere, having made significant contributions to understanding the structure and dynamics of the Sun. Among IRIS's various capabilities, perhaps its most remarkable is the generation of full-Sun mosaics, which extend beyond individual snapshots of the solar state to offer comprehensive, high-resolution maps that have allowed scientists an unprecedented view of the Sun's many layers, from the photosphere to the upper chromosphere.

Creating a full-Sun mosaic is a complex procedure, however. To achieve this, IRIS collects a series of high-resolution images, each focusing on a particular portion of the Sun that are then meticulously stitched together to form a comprehensive map. The result is a mosaic that reflects the different layers of the solar atmosphere, offering a detailed multifaceted view that is invaluable for researchers in this area.

This chapter extends the work established in chapter 3 by focusing on the entire solar disc. More specifically, it examines the centre-to-limb variations of spectral line features for the Mg II h&k lines, which are particularly useful as diagnostic tool with respect to determining the conditions in various layers of the Sun's atmosphere. To illustrate this, the chapter examines an IRIS mosaic captured on February 24, 2019, which corresponds to the solar minimum period marking the end of the 24th solar cycle. Section 4.1 offers an overview, outlining the significance of centre-to-limb observations in solar atmosphere and referencing existing studies to offer context for the current research. Section 4.2 then presents the temperature minimum region of the solar atmosphere. In Section 4.3, the focus is on the formation heights of the Mg II lines for the spectral feature k_1 , while section 4.4 provides an overview of the data used in this study, specifically the IRIS Full-Disc Mosaic, offering details of the data selection and reduction process. Section 4.5 presents Mg II k line profiles for 20 different annuli. Section 4.6 focuses on centre-to-limb variation of the Mg II h&k lines, with a focus on features such as intensities, line widths, total integrated intensities, temperatures, velocities, and depth k_3 . Section 4.7 thus offers

a discussion of these data, highlighting various interpretations and implications of the findings presented throughout the chapter, and section 4.8 rounds up the chapter by offering a summary and conclusions.

4.1 Introduction to Centre-to-Limb Variation

The study of centre-to-limb variation in the solar atmosphere plays a role in the analysis of Mg II h&k lines, as well as helping facilitate understanding of the three-dimensional structure of the solar chromosphere, an aspect that is important for accurate interpretation of data and for advancing understanding of chromospheric properties and dynamics. The phenomenon of centre-to-limb variation is related to the ways in which solar radiation propagates through the chromosphere, with the term "centre-to-limb" referring to the gradient of solar radiation as measured from the centre of the solar disc to its edge, or limb.

One of the most pronounced manifestations of centre-to-limb variation is limb darkening, which causes the solar disc to appear darker at the edges and brighter at the centre. CLV, including the phenomenon of limb darkening, occurs because of how the observer's line of sight changes when looking at different parts of the solar disc. When you look directly at the centre of the Sun, your line of sight penetrates deeper into the solar atmosphere, reaching layers that are hotter and denser. These layers emit more radiation, making the centre of the solar disc appear brighter.

As your line of sight shifts towards the edge, or limb, of the solar disc, the angle of observation changes. This angle means the light comes from progressively higher layers of the Sun's atmosphere as you move to the limb. These higher layers are the photosphere and, above it, the chromosphere, where the temperature initially decreases with altitude before increasing again in the chromosphere. However, the key point for limb darkening is that the layers from which most light reaches the observer at the limb are cooler and less dense than those viewed directly at the center. This change occurs because the opacity of the solar material varies with wavelength and height, causing the depth at which the solar radiation effectively comes from (often referred to as the optical depth $\tau=1$ layer) to be located higher in the atmosphere at the limb compared to the center. The cooler higher layers emit less intense radiation, causing the limb to appear darker than the center (Pierce and Slaughter [1977]).

Such study of Mg II h&k lines is itself pivotal in terms of supporting understanding of chromospheric activity, as these lines are sensitive to temperature and magnetic field variations. However, accurate modelling of the Mg II lines requires a deep understanding of centre-to-limb variations in the solar chromosphere to enable more precise diagnostics of the state and variability of the chromosphere across various solar cycles (e.g., Schmit et al. [2015] and Gunár

et al. [2021]).

4.1.1 Importance of Centre-to-Limb Observations

The utilisation of centre-to-limb observations in solar atmosphere ushered in a paradigm shift in the understanding of the solar atmosphere, particularly with respect to the chromosphere. By encompassing the variations observable from the centre to the limb of the solar disc, researchers can instead access three-dimensional perspective, and this multi-angular approach may be instrumental in unpacking the complexities of chromospheric properties and dynamics.

The significance of Mg II h&k lines in this context thus cannot be overstated. As they originate from the chromosphere, these absorption lines act as robust diagnostic tools that permit scrutiny of physical conditions, such as temperature gradients, flow velocities, and magnetic field strengths (Leenaarts et al. [2013b]). The sensitivity of Mg II h&k lines to these variables also adds new constraints on the chromosphere's three-dimensional structure. Unlike prior one-dimensional models, the resulting three-dimensional models can account for variations in chromosphere properties (Leenaarts et al. [2012]), as three-dimensional models are more appropriate for representing the intricate heterogeneity seen in chromospheric conditions.

4.1.2 Previous Studies and Findings Methods

The study of Mg II h&k lines has evolved over time, with researchers adopting various approaches to examine these to better understand the conditions of the solar atmosphere. Previous studies have primarily employed two methods to examine the centre-to-limb variation of Mg II h&k lines, observational techniques and numerical simulations. Observationally, spectrographs mounted on space telescopes, such as IRIS, have thus been used to obtain high-resolution data across the solar disc.

Numerical simulations provide another avenue for understanding centre-to-limb variation behaviours. Radiative transfer codes have thus been used to simulate the Mg II h&k lines under different atmospheric conditions, while state-of-the-art models often incorporate complex physical processes such as Non-Local Thermodynamic Equilibrium (non-LTE) effects, 3D geometry, and, when coupled with MHD calculations, magnetic structures (e.g., Leenaarts et al. [2013a,b]). These simulations offer an insight into the physical processes driving centre-to-limb variation and facilitate the refinement of observational diagnostics.

The studies on the center-to-limb variation of Mg II h&k lines, combining observational techniques with IRIS and numerical simulations, have provided crucial insights into the dynamics of the solar atmosphere. Observations have shown variations in line intensity across different solar regions, revealing the complex atmospheric conditions (e.g. Schmit et al. [2015] and Gunár et al. [2021]). Numerical simulations, considering non-LTE effects and magnetic structures,

have helped explain these variations, shedding light on temperature distribution and magnetic field impacts. These findings deepen our understanding of the solar atmosphere's structure and behaviour, and help interpret temperature gradients, intensity changes, and magnetic field configurations across the solar disc. We expect that the centre-to-limb variation indicates a decrease in intensity due to limb darkening effects and cooler temperatures towards the solar limb, illustrating intricate atmospheric interactions and energy transfer processes within the Sun.

Scientific exploration of the Sun has seen significant advances as the use of tools such as IRIS has progressed, however. One of the most contributions to this field was by [Schmit et al. \[2015\]](#), whose research primarily utilised IRIS to delve into the deeper characteristics of the Mg II h line. Their rigorous analysis identified variations of this line across the solar disc and its various regions, which established a foundational platform for subsequent researchers to build on, based on their unveiling of the intricate nuances of these spectral features in a manner that has shed light on their importance and their multiple implications in the field of solar studies.

Building on this foundational work, [Gunár et al. \[2021\]](#) published a recent study on the centre-to-limb variations of Mg II h&k lines based on the use of a carefully curated set of full-Sun mosaics obtained from IRIS. The study thus provided disc-averaged reference profiles for Mg II h and Mg II k lines, illustrating the ways in which these profiles vary from the solar disc's centre to its limb. They also concluded that these reference profiles should serve as valuable boundary conditions for radiative-transfer models, aiding the study and understanding of various solar structures such as prominences, spicules, and similar features in the chromosphere and corona.

4.2 The Temperature Minimum Region of the Solar Atmosphere

The Sun's atmosphere is a complex and multi-layered structure formed of the photosphere, chromosphere, transition region, and corona, with each layer contributing unique characteristics and behaviours to the overall structure. The temperature minimum region, is located 500 km above the photosphere ([Vernazza et al. \[1981\]](#)) between the photosphere and chromosphere. Despite the obvious intuitive expectation, the Sun's temperature does not consistently decrease as the measurement point moves away from the Sun's "surface" or photosphere, where temperatures average around 5,500 K. Instead, in the temperature minimum region, temperatures dip to approximately between 3,800 and 4,100 K at the limb, and disc centre, respectively, before escalating again, quite dramatically, across the chromosphere and corona to values ranging from tens of thousands to millions of K ([Avrett and Loeser \[2008\]](#)). This perplexing thermal behaviour has led to the temperature minimum region becoming the subject of numerous studies and subject to intense scrutiny, primarily because it serves as a pivotal transitional zone between the relatively

well-understood, cooler photosphere and the much hotter outer layers of the Sun's atmosphere.

4.3 Formation Heights of Mg II Lines for Spectral Feature k_1

The spectral features k_1 and h_1 refer to the outer minima of the profiles in the Mg II h&k lines, respectively. Understanding the formation heights of these spectral features can thus provide insights into the physical properties and dynamics of the regions of the atmosphere in which they form. Both k_1 and h_1 features are usually formed at heights about 500 kilometres above the photosphere (Vernazza et al. [1981]), and the formation of these lines is typically modelled using non-local thermodynamic equilibrium (non-LTE) radiative transfer simulations. Such simulations indicate that formation heights are influenced by multiple factors, including temperature gradients, densities, and the presence of magnetic fields (Carlsson et al. [2016]). Observations from space-based telescopes such as IRIS have provided invaluable data in terms of calibrating and validating these models (De Pontieu et al. [2014]).

One intriguing aspect of the formation heights of Mg II k_1 and h_1 lines is their sensitivity to magnetic fields. In magnetically active regions, such as sunspots and solar flares, formation heights can thus vary considerably. Magnetic fields affect both the temperature and density structure of the chromosphere, thus altering the heights where spectral lines are formed (Carlsson et al. [2016]), which makes the Mg II k_1 and h_1 spectral features useful tools for probing magnetic activity in the chromosphere. Understanding the resulting dynamic effects is thus crucial for the study of various solar phenomena, including chromospheric heating and solar flares, which can be estimated based on these lines' significant variations.

4.4 Data

4.4.1 IRIS Full-Disc Mosaic

On a monthly basis, with the exception of eclipse seasons, IRIS runs an ambitious full-disc survey program that delves into six spectral ranges. These spectral ranges encompass a range of lines such as the Mg II h and k, C II 1334 and 1335, and Si IV 1393 and 1403. This involves the joining of a series of meticulously planned raster scans, each with a different pointing, that collectively span the entirety of the solar disc. This requires 184 pointings, taking up around 18 hours of dedicated observation time (Schmit et al. [2015]). In order to track changes in the instrument's sensitivity during its operational period, full-Sun mosaics are mostly created. To achieve this goal, these observations are compared with data collected at the same time by the Solar EUV Experiment or SORCE/SOLSTICE II, which is carried out on the Thermosphere Ionosphere Mesosphere Energetics and Dynamics (TIMED) spacecraft (Wülser et al. [2018]) and was described by Woods et al. [2005]. The core of IRIS's observational methodology is the

64-step raster scan. This operation uses steps of 2 arcseconds each and 2 s exposure time at each slit position. The spatial region that the resulting raster scan covers is roughly 175 arcseconds in height, which corresponds to the height of the spectral slit, and 128 arcseconds in width, which mirrors the raster's range. At each steps, IRIS captures two distinct perspectives, based on recording both the Far Ultraviolet (FUV) and Near Ultraviolet (NUV) spectra. The exposure durations for these snapshots range between 1 and 2 seconds, and this is a testament to the speed of IRIS's data acquisition capabilities (Schmit et al. [2015]). However, the true value of this work lies in the post-observation data processing. The collected raster scans, each offering a piece of the necessary jigsaw, are reassembled into three-dimensional data cubes after data collection. These data cubes are identified using coordinates (X , Y , λ), where X and Y map the spatial dimensions of the solar disc, and λ extends into the spectral dimension. In essence, these data cubes thus offer a comprehensive snapshot of the entire solar disc, with each dimension capturing a unique facet of the Sun's behavior.

4.4.2 Data Selection and Data Reduction

We utilise high-resolution data from a single IRIS full-Sun mosaic for the Mg II k line, obtained on February 24, 2019, as shown in Fig. 4.1, corresponding to the period of solar minimum, which is the end of the 24th solar cycle. The selected IRIS full-Sun mosaic takes the form of a massive dataset with more than 6×10^6 pixels.

One of the first steps in the data reduction process is the exclusion of bad pixels, that is, those with intensity values that are either zero or negative. Such values are generally considered to be faulty pixels, data transfer issues, or other anomalies, and removing these bad pixels is important, as they can introduce errors and inaccuracies into all subsequent stages of data analysis. The second step is that the sun's disc was divided into 20 concentric annuli based on the sun's radius, as shown in Fig. 4.2. For each of the 20 identified annuli, all the pixel values within that annulus were averaged to help reduce local variations and anomalies and to generate a smoother and more representative line profile. This step also further reduced the data volume, transforming the millions of individual intensity measurements into a set of 20 average values by annulus. Finally, a single line profile was obtained for each annulus, forming the primary data products used in the final analysis.

4.5 Mg II k Line Profiles for 20 Annuli

To study the spatial variations of the Mg II k line across the solar disc, the disc was divided into 20 concentric annuli of equal width, approximately 49 arcseconds, allowing for a comprehensive analysis with consistent spatial resolution. This configuration supported examining the k line's variations, not just at the solar centre or limb but across various intermediate distances. The inner and outer radii for each of these annuli, labelled a-t, are detailed in Table 4.1. A single

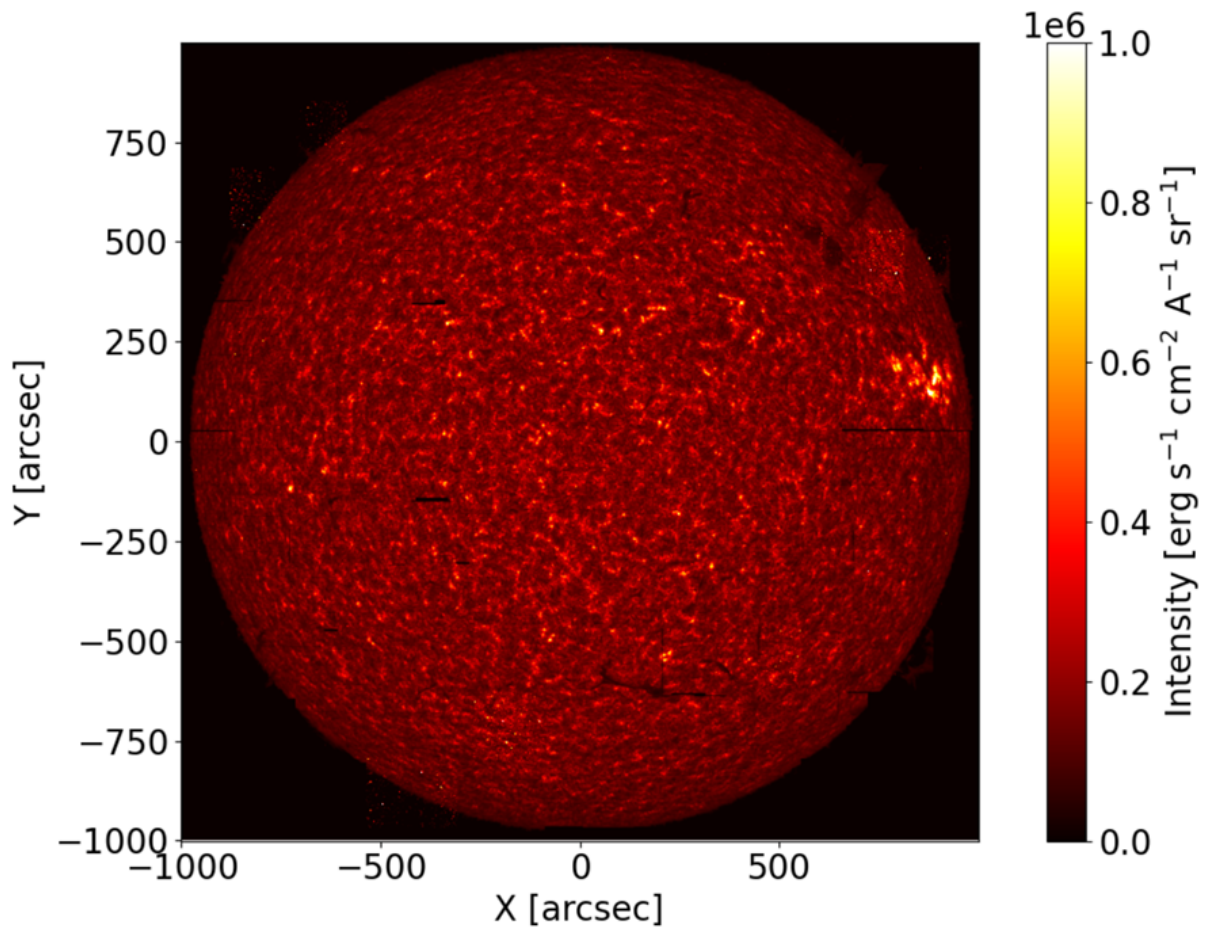


Figure 4.1: The IRIS full-disc mosaic captured on February 24, 2019, which coincided with the solar minimum phase at the end of the 24th solar cycle. This image represents the Mg II k averaged spectral window.

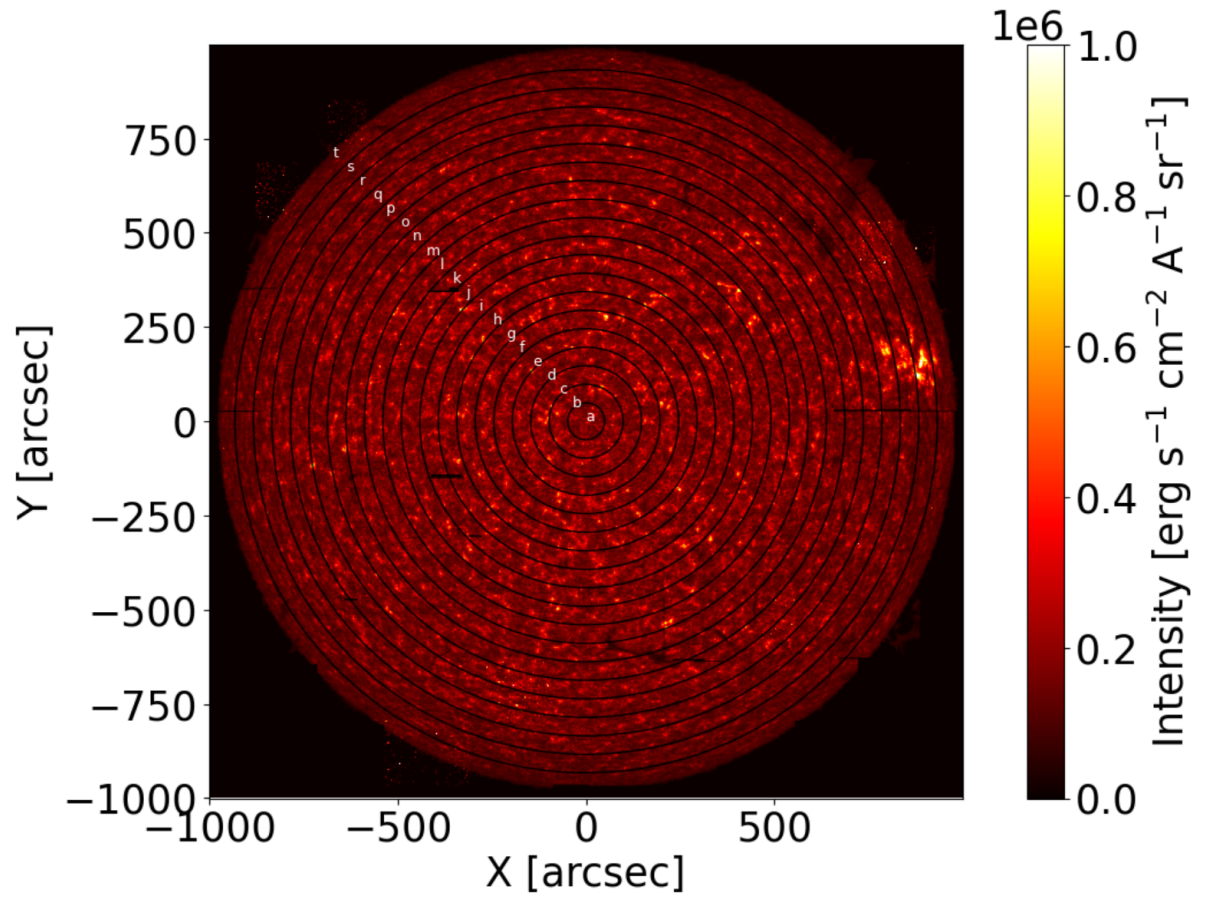


Figure 4.2: The IRIS full-disc mosaic captured on February 24, 2019, divided into a set of circles that delineate 20 distinct zones, each designated with the letters 'a' through 't'.

averaged profile was used for each annulus, as represented in Figs. 4.3 and 4.4. Rather than examining individual spectral lines from various points within an annulus, an averaged profile was computed over the entire annulus to reduce local fluctuations or anomalies that might skew the data.

Table 4.1: A compilation of the inner and outer radii (in arcseconds) for the 20 annuli featured in Fig. 4.2, each of nearly uniform width of approximately 49 arcseconds.

	a	b	c	d	e	f	g	h	i	j
Inner	0	49	98	147	196	245	294	343	392	441
μ_{inn}	1	0.998	0.995	0.989	0.98	0.968	0.954	0.937	0.917	0.893
Outer	49	98	147	196	245	294	343	392	441	491
μ_{out}	0.998	0.995	0.989	0.98	0.968	0.954	0.937	0.917	0.893	0.866
	k	l	m	n	o	p	q	r	s	t
Inner	491	540	589	638	687	736	785	834	883	932
μ_{inn}	0.866	0.835	0.8	0.76	0.7	0.661	0.6	0.527	0.437	0.312
Outer	540	589	638	687	736	785	834	883	932	981
μ_{out}	0.835	0.8	0.76	0.7	0.661	0.6	0.527	0.437	0.312	0

4.6 Centre-to-Limb Variation of Mg II h&k Lines

The current work sought to study the variation of the Mg II k line over the sun's disc based on the angular position on the solar disc (μ) as given by the equation

$$\mu_i = \sqrt{1 - \left(\frac{r_i}{R}\right)^2} \quad (4.1)$$

where R denotes the Sun's radius, and r_i is the radius of the outer annulus.

With this metric in place, the investigation moved to the relationship between μ and the atmospheric properties outlined in Table 4 of Pereira et al. [2013]. These properties span several aspects: the velocity k_2 mid-chromospheric velocity (peak separation), the temperatures (k_2 peak intensities), and the intensity ratio for k_2 .

The line of sight velocity for the k_2 peak separation measures the shift in wavelengths between the peak separation for k_2 and the reference wavelengths at 2796.35 Å. Here, the equation from Pereira et al. [2013]

$$v = \frac{\Delta\lambda}{\lambda_0} c \quad (4.2)$$

where v represents the mid-chromospheric velocity, $\Delta\lambda$ is the difference in wavelength between k_{2v} and k_{2r} , and λ_0 represents the reference wavelength for the Mg II k line at 2796.35 Å.

One of the previous studies conducted by Pereira et al. [2013] focused on correlating velocity shifts observed in photospheric lines with atmospheric vertical velocities at specific heights,

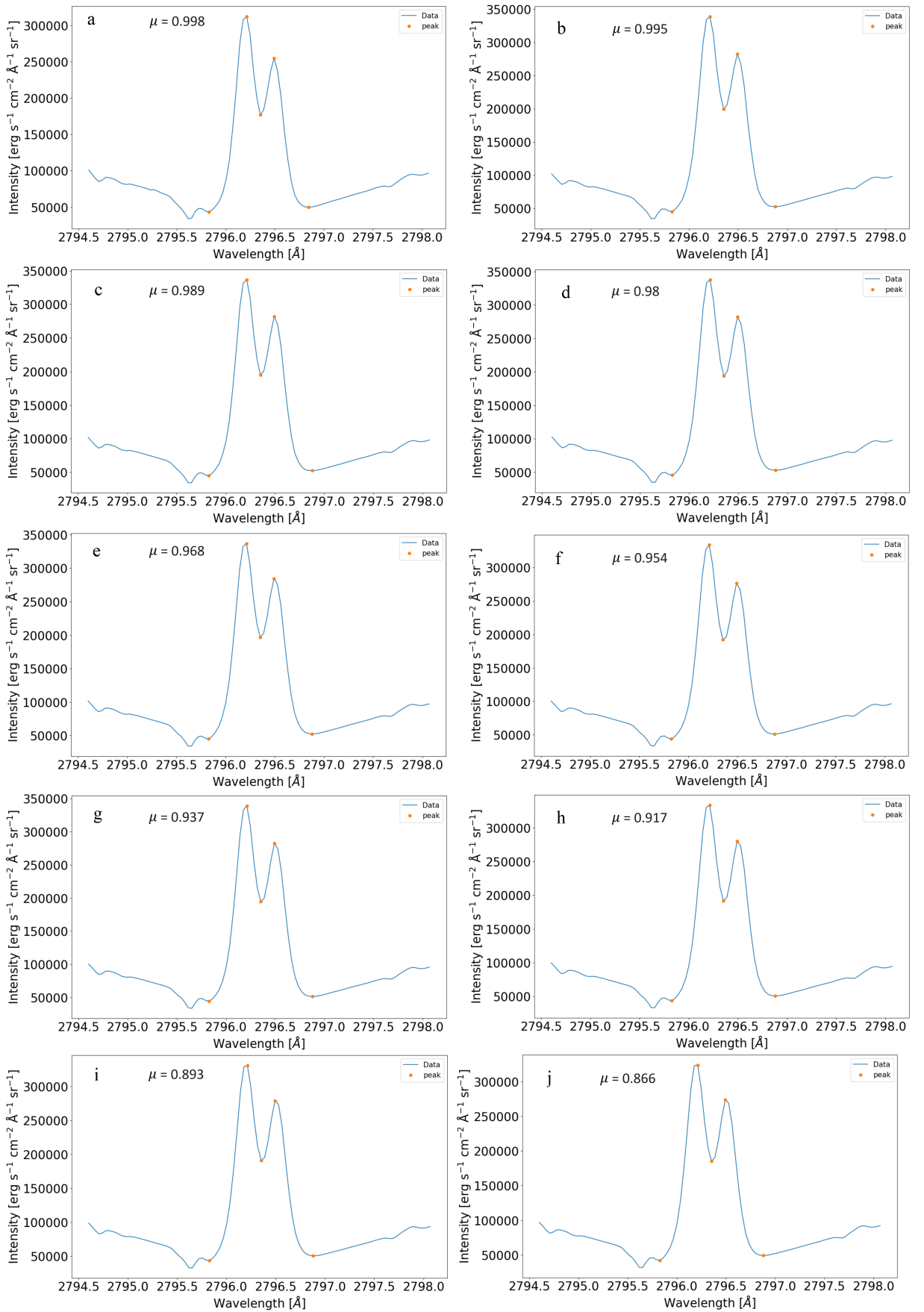


Figure 4.3: Averaged profiles of the Mg II k line for each of the annuli labelled ‘a’ to ‘t’, as illustrated in Fig. 4.2. Moving from left to right, the orange data points represent k_{1v} , k_{2v} , k_3 , k_{2r} , and k_{1r} .

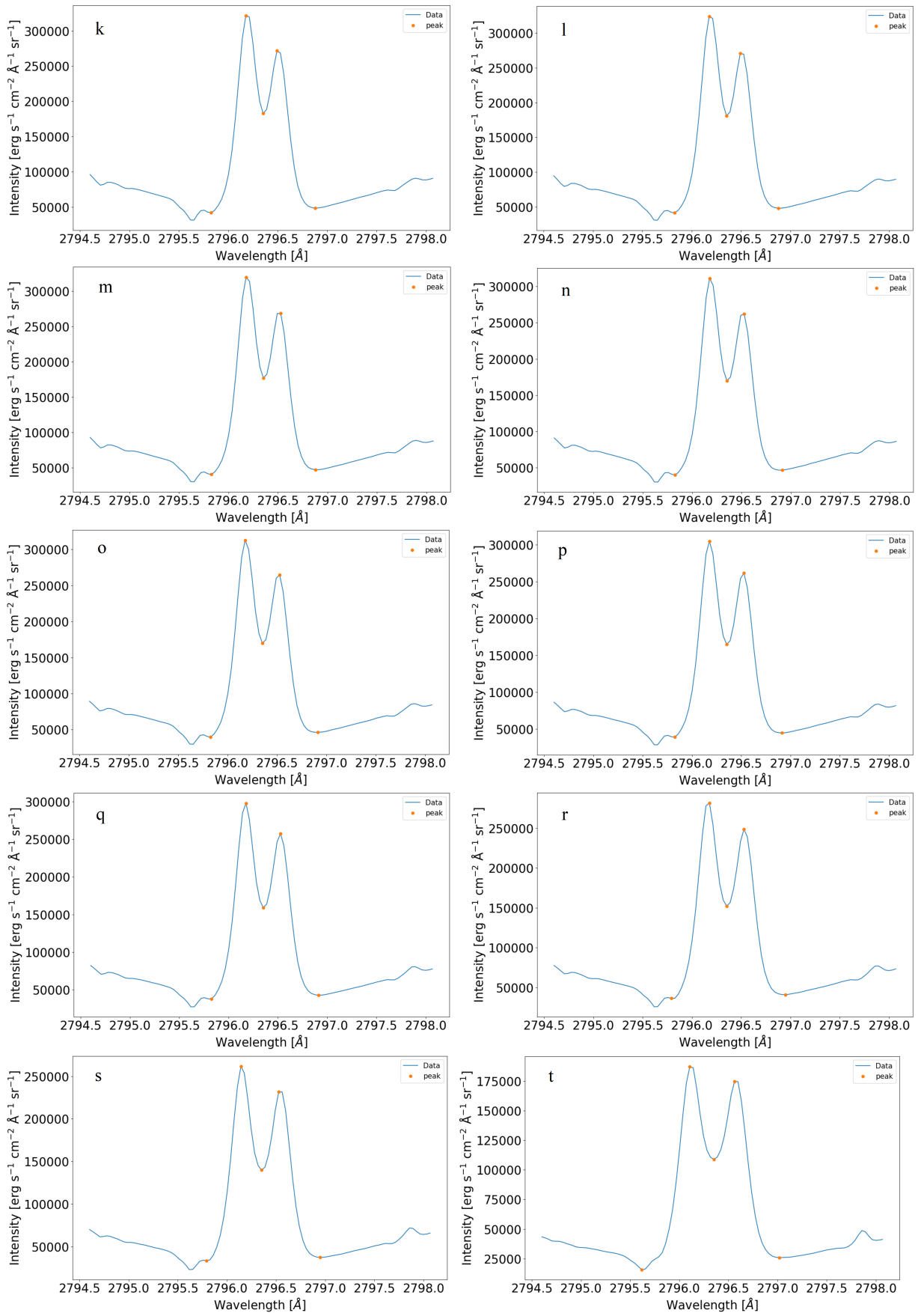


Figure 4.4: As Fig. 4.3.

defined relative to a base height where the optical depth is unity at 500 nm. Photospheric lines were analysed to identify their formation heights, and the lines grouped based on these heights into eight bins, over which their velocity shifts were averaged to obtain better statistical accuracy. The analysis encountered challenges in precisely matching line formation heights to atmospheric velocities due to the corrugated nature of the line formation regions and the influence of line blends at extreme velocities. Results across 37 snapshots showed generally good agreement between observed velocity shifts and atmospheric velocities, despite larger-than-expected shifts attributed to oscillations in the simulation. This variance highlights the complex dynamics influencing velocity measurements at different atmospheric heights and underscores the potential of the methodology, despite its sensitivity to the number of lines analysed and their susceptibility to blending.

With respect to the temperatures gauged using k_2 peak intensities, the method used here was to utilise Planck's function for k_{2v} . This choice to use k_{2v} was supported by its slightly higher intensity as compared to k_{2r} .

The intensity ratio for k_2 can be measured using an equation, as noted by [Pereira et al. \[2013\]](#):

$$R_k = \frac{I_{k2v} - I_{k2r}}{I_{k2v} + I_{k2r}} \quad (4.3)$$

According to [Pereira et al. \[2013\]](#), this ratio offers an insightful way to determine the sign of velocity above the point where $\tau=1$ (at k_2 wavelength), thereby allowing a deeper comprehension of velocity distributions.

The bright grains observed in the Ca II H2v and K2v regions are most pronounced when the layer above their peak formation heights is a downward movement ([Carlsson and Stein \[1997\]](#)). Similar patterns are seen in the Mg II h&k spectral lines, which display more pronounced emission peaks due to their shorter wavelengths and greater opacity. Given the nearly symmetrical nature of line formation around the central wavelength, it is anticipated that a rising motion above the height at which emission peaks form would result in the red peaks being more pronounced than the blue, which would enable the intensity ratio of the blue to red peaks to serve as a tool to assess the mean velocity within the upper layers of the chromosphere ([Leenaarts et al. \[2013b\]](#)).

In addition to the atmospheric properties noted above, the investigation of solar properties was extended to probe the correlation between μ and several other parameters, including line width, total integrated intensities, and the separations between k_1 ($\lambda_{k1r} - \lambda_{k1v}$) and k_2 ($\lambda_{k2r} - \lambda_{k2v}$), as well as the depth at k_3 . Specifically, the D_k equation,

$$D_k = 1 - \frac{2I_{k3}}{I_{k2v} + I_{k2r}} \quad (4.4)$$

as notably utilised in [Schmit et al. \[2015\]](#) was applied to capture the depth of the h_3 line in the solar atmosphere, and they found that the averaged depth at which the h_3 core reverses is negatively correlated with the magnetic field. In this research the aim was to understand how these variables are interconnected and how they contribute to the overall structure of the sun's chromosphere.

4.6.1 Feature Intensities for All Spectral Features

As part of the ongoing investigation into the sun's atmospheric properties, the feature intensities across all spectral features demand further attention. Specifically, the focus of this study was on the centre-to-limb variation of the Mg II k line, as showcased in [Fig. 4.5](#), which references an array of spectral features referred to as k_{1v} , k_{2v} , k_3 , k_{2r} , and k_{1r} . One observation emerging from this dataset is the consistent trend across all these spectral features for intensity to decrease as the observation moves closer to the solar limb. A slight drop in intensity was also observed at the disc's centre, where $\mu = 1$, which suggests that there may be unique conditions in the disc's centre that warrant closer scrutiny. The observed drop is likely due to the selection of an overly small region in annulus "a", resulting in an average that is either noisier or dominated by brighter emissions. [Figure 4.5](#) illustrates also the discernible fluctuations across $\mu = 1$ to $\mu = 0.866$, which represent annuli 'a' through 'j' in [Fig. 4.2](#).

Our findings align closely with the research presented by [Gunár et al. \[2021\]](#), which meticulously examines the centre-to-limb variations in Mg II h&k lines using an extensive collection of full-Sun mosaics sourced from IRIS. Their analysis, particularly illustrated through the juxtaposition of Mg II k profiles across various solar zones, corroborates our observation: both studies observe a consistent trend of diminishing intensity when moving from the solar disc's centre towards its limb. This parallel in outcomes underscores the reliability of the observed phenomenon across different spectral features and datasets.

In [Figure 4.5](#), the Mg II k line exhibits a centre-to-limb intensity decrease (the limb darkening referred to earlier), which is less pronounced for the k_1 spectral features. This slower decrease for k_1 suggests that these wings, formed deeper in the chromosphere, may be more optically thick and thus less sensitive to the viewing angle. The source function's decoupling from the Planck function because of the chromosphere's non-LTE conditions, means that intensity does not directly correlate with temperature, which explains why higher and hotter chromospheric layers do not necessarily appear brighter towards the limb.

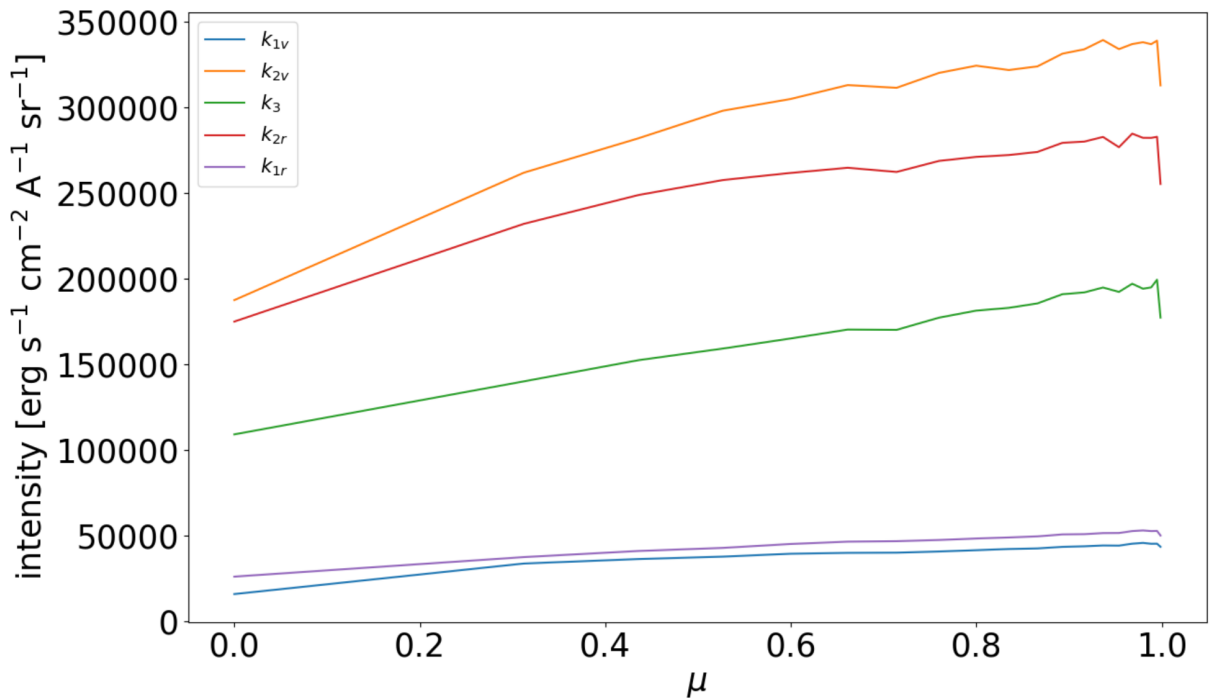


Figure 4.5: Plots demonstrating how the feature intensities for all spectral features are influenced by viewing angle, μ .

4.6.2 Line Width

Alongside exploring the spectral features, this study extended its investigation to the centre-to-limb variation of Mg II k line with respect to line width. The methodology for calculating the line width used is detailed in Sec. 3.5.4. This is presented in Fig. 4.6.

The data reveals a reverse trend in the behaviour of line width as the viewpoint moves from the solar centre to the limb, with the line width appearing to increase as the viewpoint approaches the limb. Remarkably, there is a discernible drop in line width intensity at the disc's centre where $\mu=1$, however. This drop might stem from choosing a region that is too small in annulus "a", which leads to an average characterised by increased noise or dominated by not quiet emissions. Figure 4.6 also shows that the line width values fall within a narrow range, between 0.52 and 0.69 Å, and there is also a slight fluctuation in line width from $\mu = 1$ to $\mu = 0.866$.

The broadening of the Mg II k line from the solar centre to the limb, as depicted in Fig. 4.6, is predominantly influenced by opacity broadening, where the line's optical thickness increases due to the longer path length of observation through the atmosphere at the limb.

The left panel of Fig. 4.7 shows the findings related to k_1 separation, which range between 1 and 1.4 Å. These values cluster into five specific groups: The first group contains only annulus $\mu = 0.998$; the second represents annuli $\mu = 0.995$ to $\mu = 0.76$; the third is annuli $\mu = 0.7$ to $\mu = 0.6$; the fourth encompasses annuli $\mu = 0.437$ and $\mu = 0.312$; and the fifth is solely annulus

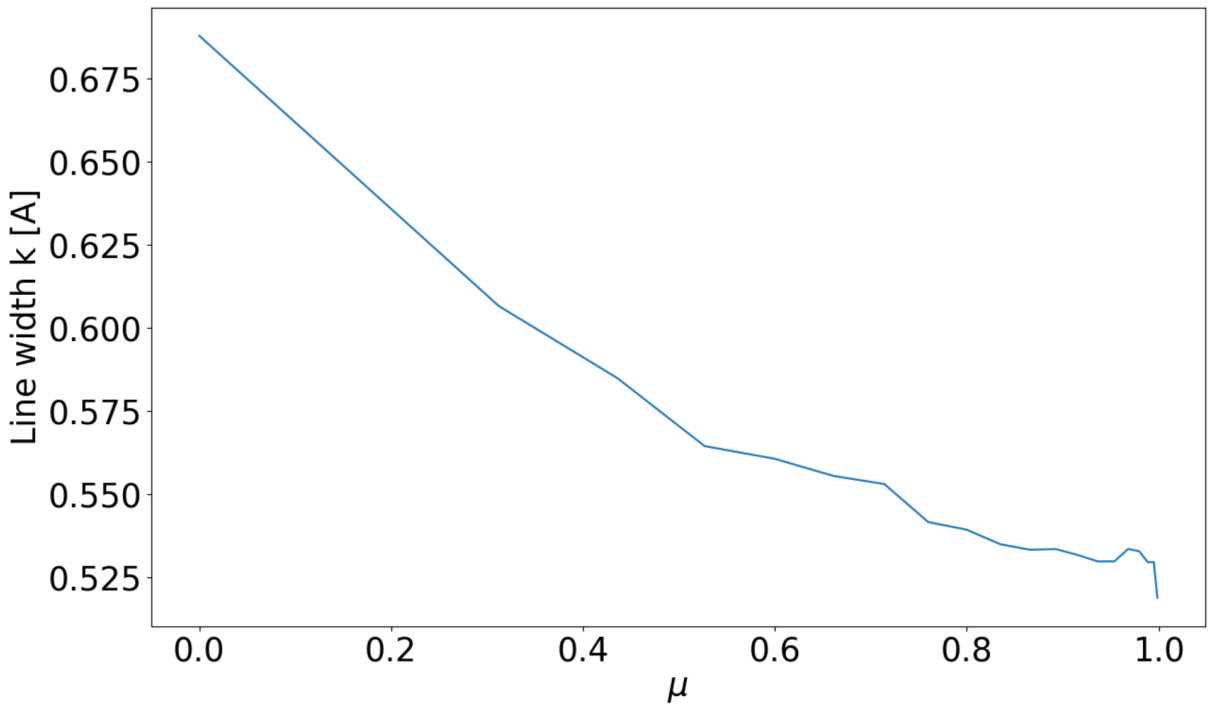


Figure 4.6: Variation in line width across different positions on the sun's disc (μ) for all profiles presented in Figs. 4.3 and 4.4.

$\mu = 0$, as shown in Fig. 4.2. We assume this is due to the spectral resolution of the instrument and the discretisation of wavelength. All annuli within a group show identical separation values, implying homogeneity within these groups. As the viewpoint moves closer to the limb, the difference in the wavelengths tends to increase, highlighting a strong correlation with the angle μ .

The right panel of Fig. 4.7 illustrates into the k_2 separation, characterised by values ranging from 0.28 to 0.46 Å. As with k_1 , these also form five distinguishable groups, though there are a different number of annuli within each group. Again, as observed in k_1 , the differences in the wavelengths within each group are identical, indicating consistency in solar atmospheric behaviours for this parameter. Once again, as the viewpoint transitions toward the limb, the k_2 separation values rise, revealing a sustained correlation with μ .

4.6.3 Total Integrated Intensities

In addition to the examination of line width and other spectral features, this research also studies the centre-to-limb variation for the Mg II k line with a specific focus on total integrated intensities. Figure 4.8 shows that a strong correlation emerged between the angular position μ on the solar disc and the total integrated intensities. Specifically, the total integrated intensities increase as the viewpoint moves closer to the sun's limb. As with line width and other spectral features, a drop is observable in total integrated intensities at $\mu=1$. Finally, Fig. 4.8 also reveals noticeable

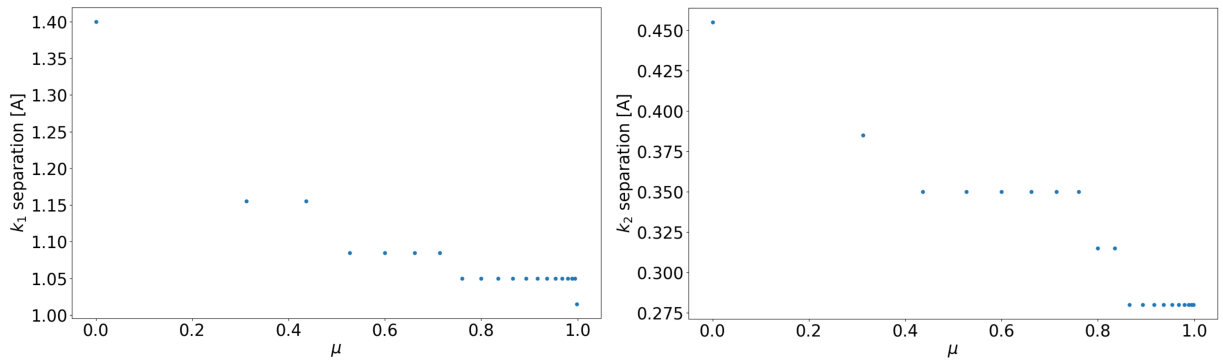


Figure 4.7: As Fig. 4.6, where the left panel represents the k_1 separation while the right panel represents the k_2 separation.

fluctuations starting from the annulus labelled $\mu = 1$ to $\mu = 0.866$.

4.6.4 Temperatures

The analysis of centre-to-limb radiation temperature changes in the Mg II k line for k_{1v} , and k_{2v} features adds another parameter to the study of the solar chromosphere. The methodologies for calculating these temperatures were outlined in Sec. 3.5.1. In Figure 4.9, the left panel is dedicated to the temperatures for k_{1v} , which are formed approximately 500 km above the photosphere, as referred in Sec. 4.3. These radiation temperatures lie within the range of 3,950 to 4,350 K. The right panel is dedicated to the temperatures for k_{2v} , which is formed in the mid-chromosphere, which range between 4,850 and 5,200 K.

Across both panels, a strong correlation was observed between the angular position μ and the temperatures for k_{1v} and k_{2v} . Overall, temperatures decrease as the viewing angle moves towards the limb. There is a slight drop in temperatures for k_{1v} and a more pronounced drop for k_{2v} at $\mu=1$. Finally, Figure 4.9 illustrates the temperature fluctuations starting from $\mu = 1$ to $\mu = 0.866$ that parallel the variability previously noted in line widths.

The decrease in radiation temperature for both k_{1v} and k_{2v} features as a function of μ towards the limb, observed in Fig. 4.9, is indicative of the complex interplay between the chromosphere's thermal structure and the geometry involved in solar observation. While it is true that the k_{2v} feature forms higher in the chromosphere where temperatures are generally higher than the temperature minimum, the observed temperature decrease towards the limb can be attributed to several factors. Firstly, the angle of observation affects the path length through the chromosphere, and thus the light we observe comes from different heights and at different angles. As μ decreases, the line of sight through the chromosphere becomes more oblique, meaning we are observing through more of the cooler upper layers and less of the hotter lower layers, leading to a net decrease in observed temperature. Moreover, the assumption of LTE becomes less valid at these greater heights and more oblique angles. In non-LTE conditions, the intensity

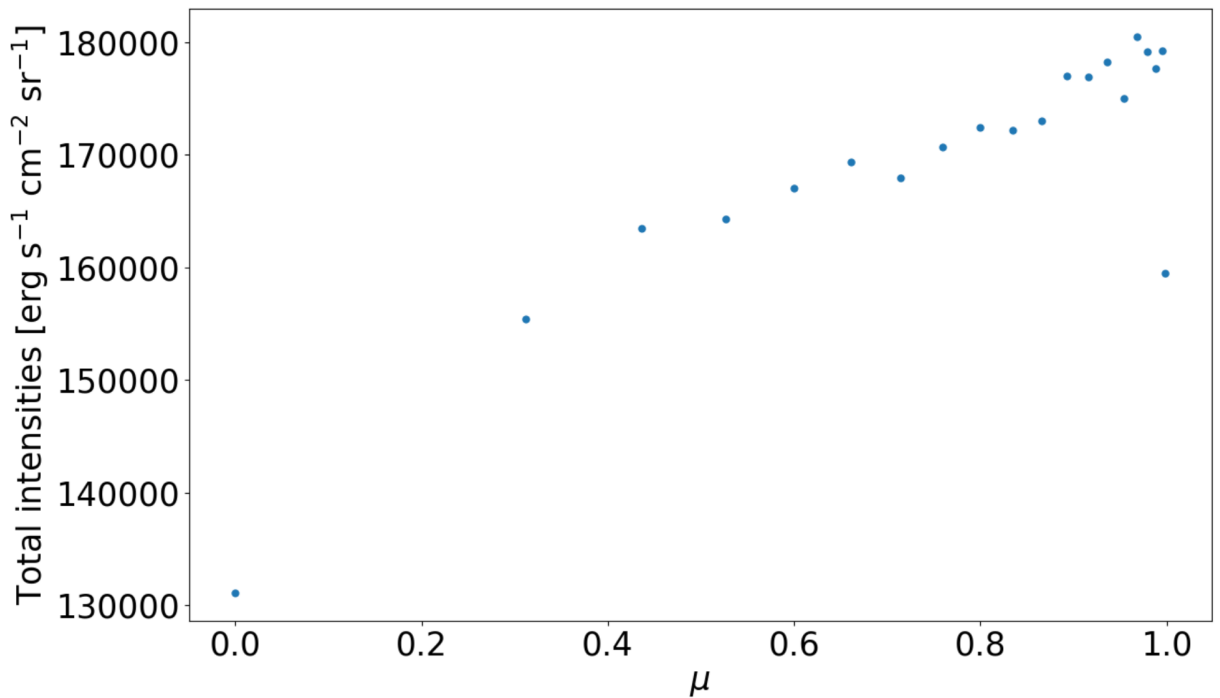
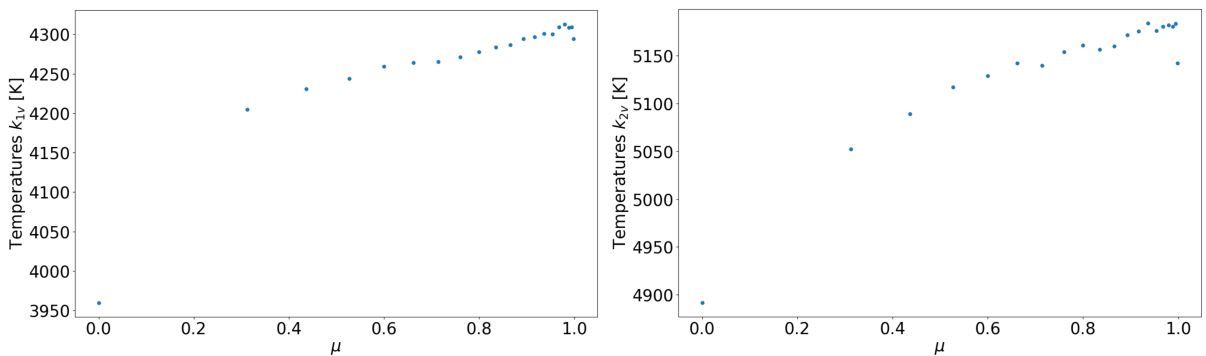


Figure 4.8: As Fig. 4.6 for total integrated intensities.

Figure 4.9: As Fig. 4.6, but representing temperatures for k_{1v} , and k_{2v} .

of radiation does not directly translate to local gas temperature, making it challenging to infer temperature from k_{2v} intensity for lower μ 's. Instead, the radiation we detect is increasingly influenced by scattering processes, rather than the local temperature. Therefore, the decrease in inferred temperatures towards the limb in the observed Mg II k line features is a result of both the observational geometry and the departure from LTE conditions at higher altitudes in the chromosphere.

4.6.5 Velocities

To support ongoing research on solar atmospheric properties, this study also investigates the centre-to-limb variations in the Mg II k Line, focusing on two important parameters: the velocities of k_2 separation and the intensity ratio of k_2 .

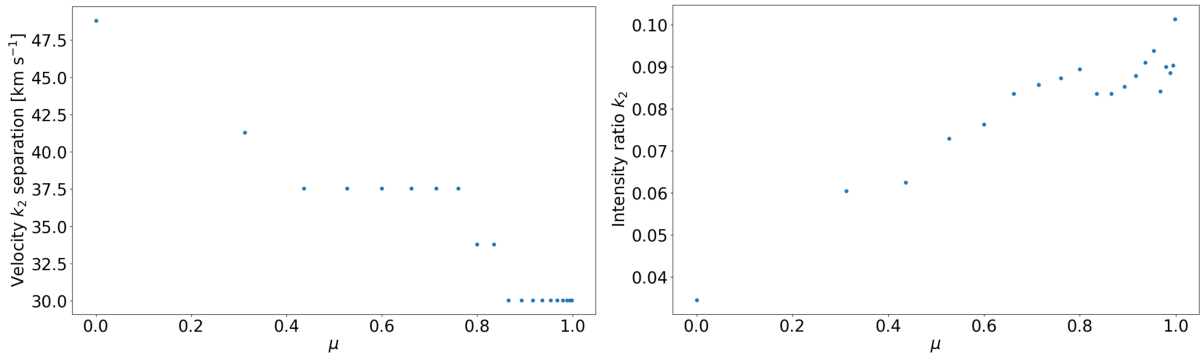


Figure 4.10: As in Fig. 4.6, the left panel represents the velocities of k_2 separation while the right panel represents the intensity ratio of the blue and red peaks.

Figure 4.10 presents the relevant findings in two panels. The left panel illustrates the velocities of k_2 separation, essentially quantifying the shifts in wavelengths between peak separation for k_2 and the corresponding reference wavelength at 2796.35 Å. The difference in wavelength positions between two emission peaks provides us with a measure of the mid-chromospheric velocity gradient (refer to Table 4 presented in Pereira et al. [2013]). The plot shows that the velocities for k_2 separation fall within a range of 30 to 49 km s⁻¹ (positive velocities correspond to upflows).

Interestingly, the data points in the left panel can be classified into five distinct groups, each representing a series of annuli on the solar disc. The first group represents the annuli from $\mu = 0.995$ to $\mu = 0.866$; the second encompasses the annuli $\mu = 0.835$ and $\mu = 0.8$; the third includes all annuli from $\mu = 0.76$ to $\mu = 0.437$; while the fourth is solely the annulus $\mu = 0.312$, and the fifth is the annulus $\mu = 0$. We believe this may result from the instrument's spectral resolution and wavelength discretisation. All annuli within a given group exhibit the same velocities, and as the viewpoint moves towards the solar limb, these velocities display a positive correlation with angle μ , increasing consistently.

The right panel of Fig. 4.10 deals with the intensity ratio for k_2 , which is vital for determining the sign of the velocity above the point where $\tau=1$ (at k_2 wavelength). As with the k_2 separation velocities, a strong correlation can be observed between μ and the intensity ratio for k_2 , though in this case, the intensity ratio for k_2 decreases as the viewpoint moves towards the limb. Some fluctuations in the intensity ratio for k_2 from annulus $\mu = 0.995$ to annulus $\mu = 0.835$ may also be observed.

4.6.6 Depth k_3

This study also investigated the average reversal depth of the k_3 core, as shown in Fig. 4.11, which illustrates the strong correlation between the angle μ and the depth of k_3 . More specifi-

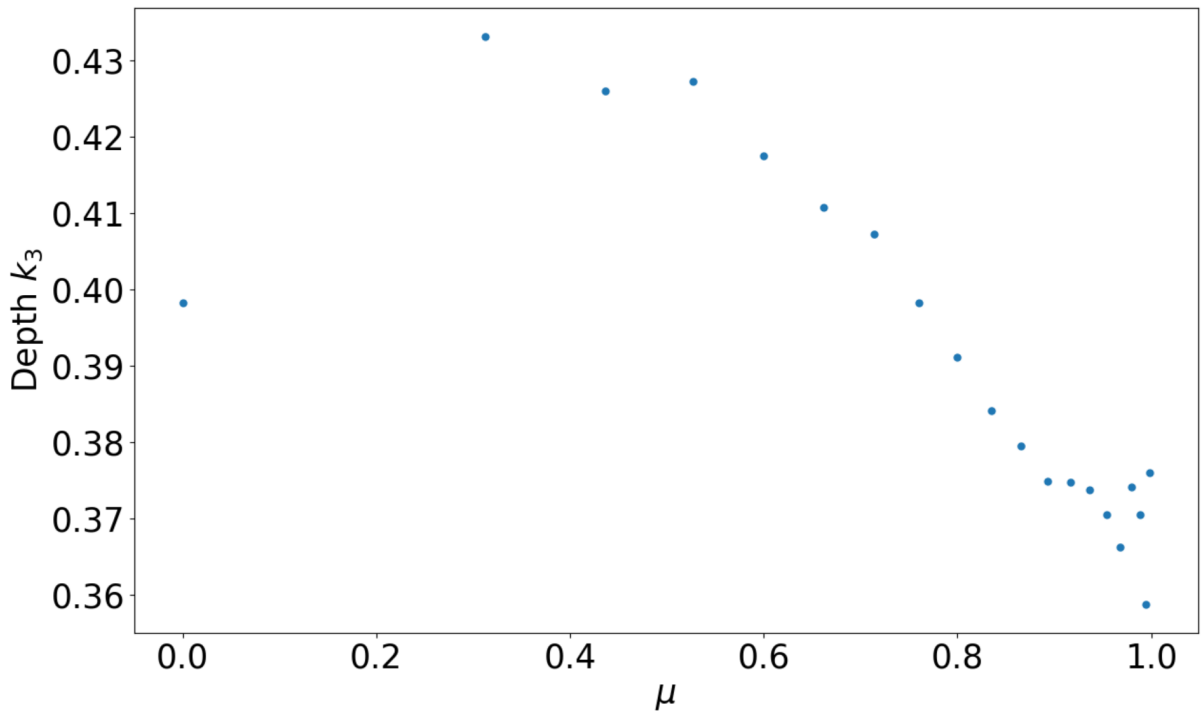


Figure 4.11: As Fig. 4.6, based on the average reversal depth of the k_3 core

cally, as the viewpoint moves towards the limb of the solar disc, the k_3 depth increases congruent with the trends observed for other spectral features; this thus confirms the robustness of the relationship between viewing angle and atmospheric depth. However, related observations also generate some more confusing findings, including fluctuations in the k_3 depth starting from $\mu = 0.995$ to $\mu = 0.893$.

4.7 Discussion

In this study, variations in the Mg II k line across the solar disk were investigated by correlating the angular position with various atmospheric properties. Specifically, the k_2 mid-chromospheric velocity (peak separation), radiation temperatures indicated by k_{1v} and k_{2v} , the k_2 intensity ratio, line width, and total integrated intensities were investigated alongside the k_1 and k_2 separations and the depth at k_3 .

In the analysis illustrated in Fig. 4.5, a uniform trend emerged across all spectral features, namely k_{1v} , k_{2v} , k_3 , k_{2r} , and k_{1r} , with the intensity decreasing as the viewpoint approaches the limb of the sun. This finding is consistent with the results from Schmit et al. [2015], which demonstrated negative centre-to-limb trends in the intensities of h_1 , h_2 , and h_3 . However, there are differences between the current data and that used by Schmit et al. [2015]. The current approach involved averaging all pixels within an annulus, while Schmit et al. [2015] focused on the variations of the Mg II h line across different, structurally distinct regions of the Sun. These

different approaches may potentially result in different implications for each study. In addition, while this work investigated the correlations between the intensities of all spectral features in the Mg II k line and the angular μ , Schmit et al. [2015] limited their study to the correlations between μ and h_{1v} , h_{2v} , and h_3 .

In Figure 4.7, a notable correlation between μ and both separation k_1 and separation k_2 can be observed. As the viewpoint moves closer to the sun's limb, the separation for both k_1 and k_2 increases: the range of difference in wavelengths for separation k_1 is between 1 and 1.4 Å, while for separation k_2 , it falls between 0.28 and 0.46 Å. These observations are consistent with those presented by Schmit et al. [2015], which both strengthens the validity of the current observations. Our findings also align with those of Gunár et al. [2021], who observed that the widths of the profiles increase closer to the solar limb. In their study, they used 12 IRIS full-Sun mosaics and filtered out brighter regions to mitigate the impact of local variations attributed to on-disc solar features and to attain reduced levels of uncertainty.

Figure 4.9 shows a strong correlation between μ and the radiation temperatures for the spectral features k_{1v} , and k_{2v} , such that as the viewpoint moves closer to the sun's limb, the temperatures for these features decrease. The right panel clearly shows that the radiation temperatures for k_{2v} range between 4,850 and 5,200 K, lower than might be expected for temperatures in the mid chromosphere, however, which, according to Vernazza et al. [1981], should be between approximately 6,000 and 7,000 K. The left panel shows that the radiation temperatures for k_{1v} lie in the range of 3,950 to 4,350 K. These features are formed in the lower chromosphere, approximately 500 km above the photosphere, and the results overall align closely with the findings of Vernazza et al. [1981], who suggested that minimum atmospheric temperatures at 500 km above the photosphere should be between 4,100 and 4,500 K. The current observations could thus indicate the minimum temperature region of the solar atmosphere, an assumption corroborated by the work of Avrett and Loeser [2008], which indicated that minimum solar atmospheric temperatures lie between 3,800 and 4,100 K.

Figure 4.10 illustrates the intricacies of the centre-to-limb variations in the Mg II k line, with a particular focus on the velocities of k_2 separation and the intensity ratio for k_2 . The findings reveal a robust correlation between the increase in the velocities for k_2 separation and the viewpoint approaching the limb of the sun, whereas the intensity ratio for k_2 exhibits a decline with the same movement. The left panel of Fig. 4.10 details the observations of velocities for k_2 separation, which can be observed to lie within a range of 30 to 49 km s^{-1} . These findings thus show agreement with the results presented by Pereira et al. [2013], where velocities were seen to range between 5 and 45 km s^{-1} . The slight deviation in the current observations from the earlier set can be attributed to the limitations of the current dataset, which focused on only

20 profiles to represent the average of all pixels within each annulus depicted in Fig. 4.2. As shown within the right panel, investigation into the intensity ratio revealed values exclusively in the positive domain, specifically between 0.03 and 0.11. This again falls within those identified by Pereira et al. [2013], who specified a range of between -1 and 1, with minor differences again attributable to the limited focus on the 20 profiles representing the average for all pixels in each annulus. The intensity ratio for k_2 is particularly vital for interpreting velocities above $z(\tau=1)$. According to research by Leenaarts et al. [2013b], a stronger blue peak corresponds to down-flowing material above the peak formation height, whereas a stronger red peak suggests upflows.

Figure 4.11, highlights a correlation between the angular position on the solar disc and the depth of k_3 . Specifically, the depth of the central core increases as the viewpoint moves towards the solar limb. The depth values for the relevant observations lie between 0.36 and 0.43, well within the range of 0 to 0.8 presented by Schmit et al. [2015]. The minor differences between the current results and those previous results can thus be attributed to limitations in the current dataset. The methodology we adopted entailed averaging pixels within a given annulus, whereas Schmit et al. [2015] looked at how the Mg II h line changed over different Sun structural regions.

All figures exhibit a remarkable similarity that warrants closer examination: the fluctuations observed across annuli 'a' to 'j'. These variations seem to stem from their location within the region spanning from ± 30 degrees on the solar disc, corresponding to μ values ranging from 1 to 0.866. Here, μ is calculated using the equation $\mu = \cos(\theta)$. These fluctuations could be the result of many factors. Firstly, intrinsic variability in the chromospheric conditions, such as changes in temperature, density, or magnetic field strength, can cause fluctuations in the observed intensity ratio. Additionally, instrumental effects such as noise, calibration errors, or variations in sensitivity across different annuli may also contribute to these fluctuations. Furthermore, atmospheric turbulence or other dynamic processes in the solar atmosphere could introduce temporal or spatial variations in the intensity ratio, again leading to the fluctuations in the observations.

4.8 Summary and Conclusions

A high-resolution, single IRIS full-Sun mosaic for the Mg II k line, captured on February 24, 2019, was used. The sun's disc was then divided into 20 concentric annuli, and the pixel values within each annulus were averaged to reduce the final data volume, remove local variations, and make the data easier to analyse. The data reduction process thus delivered a set of 20 average line profiles which were the primary data products used in the final analysis.

The study showed the relationships between μ (the viewing angle on the solar disc) and various solar atmospheric properties. There was a strong correlation between μ and feature in-

tensities for all spectral features, total integrated intensities, and temperatures at the k_{1v} , and k_{2v} , as well as with the intensity ratio, k_2 : all of these properties reduced as the viewing angle moved closer to the solar limb. The results also showed a strong correlation between μ and several other sets of properties: line width, k_1 separation, k_2 separation, velocities at k_2 separation, and the depth at k_3 . Unlike the first group of properties, however, these parameters demonstrated increases as the viewing angle moved towards the limb.

For instance, this work determined a uniform trend of decreasing intensity in spectral features as the focus approaches the sun's limb, consistent with [Schmit et al. \[2015\]](#). Furthermore, a notable correlation between μ and separations (k_1 and k_2), temperatures (k_{1v} , k_{2v}), velocities for k_2 separation, and the depth, k_3 was observed.

Chapter 5

Conclusion

5.1 Conclusion

In this thesis, we have investigated the temporal and spatial variations of Mg II h&k lines in the solar atmosphere in order to better understand the varying physical conditions where these lines are formed and to assess their impact on the chromosphere. The investigation commenced with the first chapter emphasising how the study of Mg II h&k lines over time has reshaped our strategy towards decoding the complex structures and movements of the solar chromosphere. This transformation in understanding began with foundational research by [Durand et al. \[1949\]](#), followed by significant findings by [Lemaire and Skumanich \[1973\]](#), and was further facilitated by the invaluable data amassed by space missions like OSO-8, Skylab, and IRIS.

In Chapter 2, we introduced a novel method designed for automatically identifying the positions of the Mg II h&k spectral line features, which are k_{1v} , k_{2v} , k_3 , k_{2r} , k_{1r} , as well as their counterparts in the h line, h_{1v} , h_{2v} , h_3 , h_{2r} , and h_{1r} . To gauge the precision and capability of this algorithm, we created synthetic data using a nine-parameter double Gaussian model, encompassing roughly 630,000 profiles. We demonstrated that the algorithm is able to accurately derive the positions in wavelength and intensity of the five spectral features for a wide range of h and k line profiles, as long as they contain a central reversal and two peaks.

A preliminary analysis conducted on a single IRIS raster file has the potential to extract a wealth of information from the intricate Mg II line profile shapes by analysing their essential features. The dataset under consideration, which amasses around 1.5×10^6 MB, represent IRIS observations of the solar disc's centre spanning roughly eight years.

The specific focus on the quiet Sun, particularly at the solar disc centre, stems from its crucial role as a fundamental reference point for comprehending solar behaviour and variability. Daily disc centre rasters afford a unique opportunity to observe the Sun with exceptional spatial resolu-

tion over extended periods, enabling us to monitor changes in solar features including magnetic fields, granulation patterns, and chromospheric structures. This longitudinal study facilitates the exploration of short-term and long-term variations in solar activity and dynamics, yielding valuable insights into the underlying physical mechanisms governing the Sun's behaviour. Moreover, the investigation of Mg II lines is of paramount importance in unravelling the complex processes within the quiet Sun, especially at the disc centre. Serving as sensitive diagnostic tools, these spectral lines allow us to probe the chromosphere where they originate, providing insights into variations in temperature, velocity, and intensity over time. Consequently, the study of the quiet Sun at the disc centre, coupled with observations of Mg II lines, offers a potent avenue for unravelling the dynamic behaviour of the solar chromosphere and understanding the fundamental physical processes driving solar variability.

In Chapter 3, our exploration delved into the temporal variation of the averaged flux of all Mg II h&k features spanning the years 2015 to 2022. This timeline notably coincides with the concluding phase of the 24th solar cycle and the beginning of the 25th solar cycle. Additionally, we probed into the relationship among radiation temperatures, the total integrated intensities, and the line widths and their association with the feature intensities of all Mg II h&k lines.

Through this examination, it was ascertained that there exists a robust correlation between the temperature and the k_3 & k_{2v} intensities. However, the correlation involving k_{1r} & k_{1v} intensities was found to have more variance. A well-defined correlation was observed between the total integrated intensity and the feature intensities for k_{2v} , k_3 , and k_{2r} . The line width did not exhibit any significant relationship with k_{1v} & k_{1r} , but displayed an inverse association with k_{2v} , k_3 , and k_{2r} intensities. Lastly, upon studying the temporal changes in Mg II h&k lines over the transition from the 24th to the 25th solar cycles, the data indicated that the average flux remained relatively stable throughout this period.

In Chapter 4, the primary objective of this study has been to investigate the center-to-limb variations in spectral line characteristics through the use of mosaic data. Our technique has been applied to the entire disc of the Sun in order to achieve this research goal. The study utilised a high-resolution, single mosaic of the full-Sun in the Mg II k line, which was acquired on February 24, 2019, using the IRIS instrument. The disc of the sun was partitioned into 20 concentric annular regions, and the average pixel values inside each annulus were computed in order to decrease the overall data volume, eliminate localised changes, and facilitate the analysis of the data. The procedure of data reduction resulted in a collection of 20 average line profiles, which served as the main data products utilised in the final analysis.

The study examined the correlations between the viewing angle on the solar disc (μ) and

certain solar atmospheric parameters. A significant correlation was observed between μ and the feature intensities for all spectral features, total integrated intensities, and temperatures at the positions k_{1v} , and k_{2v} . Additionally, a correlation was found between μ and the intensity ratio k_2 . Notably, all of these properties exhibited a decrease as the viewing angle approached the solar limb. The findings additionally demonstrated a strong correlation between the parameter mu and many other sets of characteristics, line width, separation of k_1 , separation of k_2 , velocities at the separation of k_2 , and the depth at k_3 . In contrast to the initial set of attributes, these parameters exhibited increments as the viewing angle approached the limb.

5.2 Perspectives

As we reflect on the findings and implications of this study, there are many questions that require further research and investigation. The following perspectives aim to delineate potential directions, unanswered questions, and emergent themes that can guide subsequent studies and expand the horizons of our understanding in this field.

In Chapter 2, a novel method was introduced to determine the positions of the Mg II h&k spectral line features. This algorithm determines both the wavelength and intensity positions of the five spectral features across a broad spectrum of h and k line profiles, provided they encompass a central reversal by two peaks. However, it would be better to develop it to be able to handle all line profiles of different shapes, e.g., profiles with just one peak or with three or more peaks. A pressing priority is to make this algorithm publicly accessible, particularly for those keen on double-peak profiles, by integrating it into the Python library. One limitation of our current algorithm is its fixed division of the side profile into five segments based on the location of the outer minimum in the wings, emission peaks, and central absorption core. This fixed segmentation approach may lead to the exclusion of potentially useful files. Hence, there is a compelling need to enhance the algorithm's flexibility in defining these parts, ensuring that each profile is partitioned into five unique parts regardless of variations in profile shapes or wavelength shifts. This flexibility will mitigate the impact of shifted profiles towards shorter or longer wavelengths, ensuring a more comprehensive and accurate analysis.

In Chapter 3, our exploration delved into the temporal variation of the averaged flux of all Mg II h&k features spanning the years 2015 to 2022. In this study, solar phenomena in the chromosphere, e.g., network, internetwork, and plage, were not taken into account because the average intensity was taken for each raster file. Therefore, it is good to expand this study to include these structurally distinct regions of the solar atmosphere and investigate their temporal variation for all Mg II h&k features during the period.

In Chapter 4, we employed a high-resolution, single mosaic of the full-Sun captured in the Mg II k line on February 24, 2019, using the IRIS instrument. The aim was to explore the centre-to-limb variations in spectral line characteristics by analysing mosaic data. However, it is suggested that future research endeavours expand upon this study by incorporating several mosaics from various years spanning the period from 2015 to 2024. This expansion would enable a comprehensive investigation into the spatial variation of physical properties such as temperature, intensity, and line width. Additionally, there is a need to examine the temporal changes occurring during the 24th and 25th solar cycles to gain deeper insights into the evolving dynamics of the solar atmosphere over time.

In the course of the recent research, constraints in time permitted an exploration of only a subset of the abundant data available, with a primary focus on the IRIS dataset. The potential wealth of information in the HMI and AIA datasets, integral components of the Solar Dynamics Observatory (SDO), remained untapped. Recognising this limitation, an essential avenue for future research would be integrating the analyses from IRIS data with the datasets of AIA and HMI. Notably, the IRIS mosaics FITS files already contain data from these instruments that is fully co-aligned and complements nicely the IRIS data. By doing so, the aim is to gain a more profound understanding of the variations present between distinct magnetic features. The goal is to find significant differences between e.g. active region pixels and the averaged properties extracted from the rest of the analyses. For instance, by selecting the highest magnetic field intensity values in HMI, a selection criterion could involve isolating only those pixels displaying heightened magnetic field in HMI and simultaneously exhibiting high intensity in one of the AIA channels. The specific AIA channel to be employed for this purpose would require careful deliberation. Once these pixels are meticulously chosen, the subsequent step would involve leveraging them for an in-depth analysis of the IRIS data.

An imperative future goal entails conducting an in-depth comparison between non-LTE radiative transfer simulations and our findings. The amalgamation of these models with our observational dataset is paramount for achieving a comprehensive understanding of the solar chromosphere. Additionally, contextualising the analyses facilitated by our tool, which adeptly handles large datasets, within these simulations is crucial. Given the intricate formation processes of spectral lines, directly inferring temperature structures or velocity fields from line shapes is challenging. Hence, accurate elucidation of these line profiles necessitates reliance on the results from the models.

One of the future goals is also prominence modelling, in which we would explore the complex dynamics of solar prominences by comparing observational data with numerical simula-

tions. It would look into how prominences form, their shape, and the structural features seen at different wavelengths, like H-alpha, UV, and EUV. It would also look at how they change and evolve over time, including oscillations, eruptions, and lifecycles. Additionally, various magnetic configurations and plasma properties associated with prominences will be examined, validated numerical simulations through spectroscopic and imaging diagnostics will be conducted, and future directions for advancing prominence modelling techniques and enhancing observational capabilities will be discussed to further our understanding of these solar features.

Bibliography

- G. Artzner, R. M. Bonnet, J. C. Vial, A. Jouchoux, J. Leibacher, A. Vidal-Madjar, and P. Lemaire. The LPSP experiment on OSO-8. I - Instrumentation, description of operations, laboratory calibrations and pre-launch performances. *Space Science Instrumentation*, 3:131–161, May 1977.
- Martin Asplund, Nicolas Grevesse, A. Jacques Sauval, and Pat Scott. The Chemical Composition of the Sun. *ARA&A*, 47(1):481–522, September 2009. doi: 10.1146/annurev.astro.46.060407.145222.
- E. H. Avrett. Two-Component Modeling of the Solar IR CO Lines. In Jeffrey R. Kuhn and Matthew J. Penn, editors, *Infrared tools for solar astrophysics: What's next?*, pages 303–311, January 1995.
- E. H. Avrett and R. Loeser. Line transfer in static and expanding spherical atmospheres. In *Methods in Radiative Transfer*, pages 341–379. 1984.
- Eugene H. Avrett and Rudolf Loeser. Models of the Solar Chromosphere and Transition Region from SUMER and HRTS Observations: Formation of the Extreme-Ultraviolet Spectrum of Hydrogen, Carbon, and Oxygen. *ApJS*, 175(1):229–276, March 2008. doi: 10.1086/523671.
- K. Barczynski, H. Peter, L. P. Chitta, and S. K. Solanki. Emission of solar chromospheric and transition region features related to the underlying magnetic field. *A&A*, 619:A5, October 2018. doi: 10.1051/0004-6361/201731650.
- B. Bates, D. J. Bradley, C. D. McKeith, and N. E. McKeith. Fabry-Perot Interferograms of the Solar Mg II Doublet and XUV Solar Images obtained during a Stabilized Skylark Rocket Flight. *Nature*, 224(5215):161–163, October 1969. doi: 10.1038/224161a0.
- Pål Brekke. *Our Explosive Sun*. 2012. doi: 10.1007/978-1-4614-0571-9.
- David H. Brooks, Harry P. Warren, and Peter R. Young. EUV Spectral Line Formation and the Temperature Structure of Active Region Fan Loops: Observations with Hinode/EIS and SDO/AIA. *ApJ*, 730(2):85, April 2011. doi: 10.1088/0004-637X/730/2/85.

- GE Brueckner, RA Howard, MJ Koomen, CM Korendyke, DJ Michels, JD Moses, DG Socker, KP Dere, PL Lamy, A Llebaria, et al. The large angle spectroscopic coronagraph (lasco) visible light coronal imaging and spectroscopy. *The SOHO mission*, pages 357–402, 1995.
- Mats Carlsson and R. F. Stein. Dynamic Hydrogen Ionization. *ApJ*, 572(1):626–635, June 2002. doi: 10.1086/340293.
- Mats Carlsson and Robert F. Stein. Non-LTE Radiating Acoustic Shocks and CA II K2V Bright Points. *ApJ*, 397:L59, September 1992. doi: 10.1086/186544.
- Mats Carlsson and Robert F. Stein. Formation of Solar Calcium H and K Bright Grains. *ApJ*, 481(1):500–514, May 1997. doi: 10.1086/304043.
- Mats Carlsson, Viggo H. Hansteen, Boris V. Gudiksen, Jorrit Leenaarts, and Bart De Pontieu. A publicly available simulation of an enhanced network region of the Sun. *A&A*, 585:A4, January 2016. doi: 10.1051/0004-6361/201527226.
- Bradley W. Carroll and Dale A. Ostlie. *An introduction to modern astrophysics, Second Edition*. 2017.
- G. Cauzzi, K. P. Reardon, H. Uitenbroek, F. Cavallini, A. Falchi, R. Falciani, K. Janssen, T. Rimmelme, A. Vecchio, and F. Wöger. The solar chromosphere at high resolution with IBIS. I. New insights from the Ca II 854.2 nm line. *A&A*, 480(2):515–526, March 2008. doi: 10.1051/0004-6361:20078642.
- S. R. Cranmer and A. A. van Ballegoijen. On the Generation, Propagation, and Reflection of Alfvén Waves from the Solar Photosphere to the Distant Heliosphere. *ApJS*, 156(2):265–293, February 2005. doi: 10.1086/426507.
- Steven R. Cranmer. Coronal Holes. *Living Reviews in Solar Physics*, 6(1):3, September 2009. doi: 10.12942/lrsp-2009-3.
- B. De Pontieu, A. M. Title, J. R. Lemen, G. D. Kushner, D. J. Akin, B. Allard, T. Berger, P. Boerner, M. Cheung, C. Chou, J. F. Drake, D. W. Duncan, S. Freeland, G. F. Heyman, C. Hoffman, N. E. Hurlburt, R. W. Lindgren, D. Mathur, R. Rehse, D. Sabolish, R. Seguin, C. J. Schrijver, T. D. Tarbell, J. P. Wülser, C. J. Wolfson, C. Yanari, J. Mudge, N. Nguyen-Phuc, R. Timmons, R. van Bezooijen, I. Weingrod, R. Brookner, G. Butcher, B. Dougherty, J. Eder, V. Knagenhjelm, S. Larsen, D. Mansir, L. Phan, P. Boyle, P. N. Cheimets, E. E. DeLuca, L. Golub, R. Gates, E. Hertz, S. McKillop, S. Park, T. Perry, W. A. Podgorski, K. Reeves, S. Saar, P. Testa, H. Tian, M. Weber, C. Dunn, S. Eccles, S. A. Jaeggli, C. C. Kankelborg, K. Mashburn, N. Pust, L. Springer, R. Carvalho, L. Kleint, J. Marmie, E. Mazmanian, T. M. D. Pereira, S. Sawyer, J. Strong, S. P. Worden, M. Carlsson, V. H. Hansteen, J. Leenaarts, M. Wiesmann, J. Aloise, K. C. Chu, R. I. Bush, P. H. Scherrer, P. Brekke,

- J. Martinez-Sykora, B. W. Lites, S. W. McIntosh, H. Uitenbroek, T. J. Okamoto, M. A. Gumm, G. Aufer, P. Jerram, P. Pool, and N. Waltham. The Interface Region Imaging Spectrograph (IRIS). *Sol. Phys.*, 289(7):2733–2779, July 2014. doi: 10.1007/s11207-014-0485-y.
- G. A. Doschek and U. Feldman. High-resolution spectra of the solar Mg II h and k lines from Skylab. *ApJS*, 35:471–482, December 1977. doi: 10.1086/190489.
- E. Durand, J. J. Oberly, and R. Tousey. Analysis of the First Rocket Ultraviolet Solar Spectra. *ApJ*, 109:1, January 1949. doi: 10.1086/145099.
- Oddbjørn Engvold. Description and Classification of Prominences. In Jean-Claude Vial and Oddbjørn Engvold, editors, *Solar Prominences*, volume 415 of *Astrophysics and Space Science Library*, page 31, January 2015.
- Oddbjørn Engvold, Tadashi Hirayama, Jean Louis Leroy, Eric R. Priest, and Einar Tandberg-Hanssen. Hvar Reference Atmosphere of Quiescent Prominences. In Vladimir Ruzdjak and Einar Tandberg-Hanssen, editors, *IAU Colloq. 117: Dynamics of Quiescent Prominences*, volume 363, page 294. 1990. doi: 10.1007/BFb0025709.
- J. M. Fontenla, Jeffrey L. Linsky, Jesse Garrison, Kevin France, A. Buccino, Pablo Mauas, Mariela Vieytes, and Lucianne M. Walkowicz. Semi-empirical Modeling of the Photosphere, Chromosphere, Transition Region, and Corona of the M-dwarf Host Star GJ 832. *ApJ*, 830(2):154, October 2016. doi: 10.3847/0004-637X/830/2/154.
- P. Foukal, C. Fröhlich, H. Spruit, and T. M. L. Wigley. Variations in solar luminosity and their effect on the Earth’s climate. *Nature*, 443(7108):161–166, September 2006. doi: 10.1038/nature05072.
- Zoe A Frank, Richard A Shine, Theodore D Tarbell, Kenneth P Topka, Goran Scharmer, Wolfgang Schmidt, et al. On the magnetic and velocity field geometry of simple sunspots. *Astrophysical Journal, Part 1 (ISSN 0004-637X)*, vol. 403, no. 2, p. 780-796., 403:780–796, 1993.
- W. D. Gonzalez, J. A. Joselyn, Y. Kamide, H. W. Kroehl, G. Rostoker, B. T. Tsurutani, and V. M. Vasyliunas. What is a geomagnetic storm? *J. Geophys. Res.*, 99(A4):5771–5792, April 1994. doi: 10.1029/93JA02867.
- Nat Gopalswamy. Properties of Interplanetary Coronal Mass Ejections. *Space Sci. Rev.*, 124(1-4):145–168, June 2006. doi: 10.1007/s11214-006-9102-1.
- Pierre Gouttebroze. Solar Atmospheric Dynamics. III. The Effect of Acoustic Waves on the MG II K Line Profile. *ApJ*, 337:536, February 1989. doi: 10.1086/167122.

- M. Gošić, L. R. Bellot Rubio, D. Orozco Suárez, Y. Katsukawa, and J. C. del Toro Iniesta. The Solar Internetwork. I. Contribution to the Network Magnetic Flux. *ApJ*, 797(1):49, December 2014. doi: 10.1088/0004-637X/797/1/49.
- M. Gošić, J. de la Cruz Rodríguez, B. De Pontieu, L. R. Bellot Rubio, M. Carlsson, S. Esteban Pozuelo, A. Ortiz, and V. Polito. Chromospheric Heating due to Cancellation of Quiet Sun Internetwork Fields. *ApJ*, 857(1):48, April 2018. doi: 10.3847/1538-4357/aab1f0.
- Stanislav Gunár, Július Koza, Pavol Schwartz, Petr Heinzel, and Wenjuan Liu. Quiet-Sun Mg II h and k Line Profiles Derived from IRIS Full-Sun Mosaics. I. Reference Profiles and Center-to-limb Variation. *ApJS*, 255(1):16, July 2021. doi: 10.3847/1538-4365/ac07ab.
- Stanislav Gunár, Petr Heinzel, Július Koza, and Pavol Schwartz. Large Impact of the Mg II h and k Incident Radiation Change on Results of Radiative Transfer Models and the Importance of Dynamics. *ApJ*, 934(2):133, August 2022. doi: 10.3847/1538-4357/ac7397.
- David H. Hathaway. The Solar Cycle. *Living Reviews in Solar Physics*, 7(1):1, December 2010. doi: 10.12942/lrsp-2010-1.
- W. Henze and J. O. Stenflo. Polarimetry in the Mg II h and k lines. *Sol. Phys.*, 111(2):243–254, September 1987. doi: 10.1007/BF00148517.
- Ivan Hubeny and Dimitri Mihalas. *Theory of stellar atmospheres: An introduction to astrophysical non-equilibrium quantitative spectroscopic analysis*, volume 26. Princeton University Press, 2014.
- S. Ježič, R. Susino, P. Heinzel, E. Dzifčáková, A. Bemporad, and U. Anzer. Hot prominence detected in the core of a coronal mass ejection. II. Analysis of the C III line detected by SOHO/UVCS. *A&A*, 607:A80, November 2017. doi: 10.1051/0004-6361/201731364.
- D. B. Jess, R. J. Morton, G. Verth, V. Fedun, S. D. T. Grant, and I. Giagkiozis. Multiwavelength Studies of MHD Waves in the Solar Chromosphere. An Overview of Recent Results. *Space Sci. Rev.*, 190(1-4):103–161, July 2015. doi: 10.1007/s11214-015-0141-3.
- Jeremy T. Kerr, Alana Pindar, Paul Galpern, Laurence Packer, Simon G. Potts, Stuart M. Roberts, Pierre Rasmont, Oliver Schweiger, Sheila R. Colla, Leif L. Richardson, David L. Wagner, Lawrence F. Gall, Derek S. Sikes, and Alberto Pantoja. Climate change impacts on bumblebees converge across continents. *Science*, 349(6244):177–180, July 2015. doi: 10.1126/science.aaa7031.
- J. L. Kohl and W. H. Parkinson. The Mg II h and k lines. I. Absolute center and limb measurements of the solar profiles. *ApJ*, 205:599–611, April 1976. doi: 10.1086/154317.

- T. Kosugi, K. Matsuzaki, T. Sakao, T. Shimizu, Y. Sone, S. Tachikawa, T. Hashimoto, K. Minesugi, A. Ohnishi, T. Yamada, S. Tsuneta, H. Hara, K. Ichimoto, Y. Suematsu, M. Shimojo, T. Watanabe, S. Shimada, J. M. Davis, L. D. Hill, J. K. Owens, A. M. Title, J. L. Culhane, L. K. Harra, G. A. Doschek, and L. Golub. The Hinode (Solar-B) Mission: An Overview. *Sol. Phys.*, 243(1):3–17, June 2007. doi: 10.1007/s11207-007-9014-6.
- J. Kraśkiewicz, K. Murawski, A. Solov’ev, and A. K. Srivastava. On the Asymmetric Longitudinal Oscillations of a Pikelner’s Model Prominence. *Sol. Phys.*, 291(2):429–444, February 2016. doi: 10.1007/s11207-016-0850-0.
- N. Labrosse, P. Heinzel, J. C. Vial, T. Kucera, S. Parenti, S. Gunár, B. Schmieder, and G. Kilper. Physics of Solar Prominences: I—Spectral Diagnostics and Non-LTE Modelling. *Space Sci. Rev.*, 151(4):243–332, April 2010. doi: 10.1007/s11214-010-9630-6.
- J. Leenaarts, M. Carlsson, and L. Rouppe van der Voort. The Formation of the H α Line in the Solar Chromosphere. *ApJ*, 749(2):136, April 2012. doi: 10.1088/0004-637X/749/2/136.
- J. Leenaarts, T. M. D. Pereira, M. Carlsson, H. Uitenbroek, and B. De Pontieu. The Formation of IRIS Diagnostics. I. A Quintessential Model Atom of Mg II and General Formation Properties of the Mg II h&k Lines. *ApJ*, 772(2):89, August 2013a. doi: 10.1088/0004-637X/772/2/89.
- J. Leenaarts, T. M. D. Pereira, M. Carlsson, H. Uitenbroek, and B. De Pontieu. The Formation of IRIS Diagnostics. II. The Formation of the Mg II h&k Lines in the Solar Atmosphere. *ApJ*, 772(2):90, August 2013b. doi: 10.1088/0004-637X/772/2/90.
- P. Lemaire and A. Skumanich. Magnesium II Doublet Profiles of Chromospheric Inhomogeneities at the Center of the Solar Disk. *A&A*, 22:61, January 1973.
- James R. Lemen, Alan M. Title, David J. Akin, Paul F. Boerner, Catherine Chou, Jerry F. Drake, Dexter W. Duncan, Christopher G. Edwards, Frank M. Friedlaender, Gary F. Heyman, Neal E. Hurlburt, Noah L. Katz, Gary D. Kushner, Michael Levay, Russell W. Lindgren, Dnyanesh P. Mathur, Edward L. McFeaters, Sarah Mitchell, Roger A. Rehse, Carolus J. Schrijver, Larry A. Springer, Robert A. Stern, Theodore D. Tarbell, Jean-Pierre Wuelser, C. Jacob Wolfson, Carl Yanari, Jay A. Bookbinder, Peter N. Cheimets, David Caldwell, Edward E. Deluca, Richard Gates, Leon Golub, Sang Park, William A. Podgorski, Rock I. Bush, Philip H. Scherrer, Mark A. Gummin, Peter Smith, Gary Auken, Paul Jerram, Peter Pool, Regina Soufli, David L. Windt, Sarah Beardsley, Matthew Clapp, James Lang, and Nicholas Waltham. The Atmospheric Imaging Assembly (AIA) on the Solar Dynamics Observatory (SDO). *Sol. Phys.*, 275(1-2):17–40, January 2012. doi: 10.1007/s11207-011-9776-8.
- P. J. Levens and N. Labrosse. Modelling of Mg II lines in solar prominences. *A&A*, 625:A30, May 2019. doi: 10.1051/0004-6361/201833132.

- KJ Li, W Feng, and FY Li. Predicting the maximum amplitude of solar cycle 25 and its timing. *Journal of Atmospheric and Solar-Terrestrial Physics*, 135:72–76, 2015.
- W. C. Livingston and J. Harvey. A New Component of Solar Magnetism - The Inner Network Fields. In *Bulletin of the American Astronomical Society*, volume 7, page 346, March 1975.
- D. H. Mackay, J. T. Karpen, J. L. Ballester, B. Schmieder, and G. Aulanier. Physics of Solar Prominences: II—Magnetic Structure and Dynamics. *Space Sci. Rev.*, 151(4):333–399, April 2010. doi: 10.1007/s11214-010-9628-0.
- Dimitri Mihalas. Stellar atmospheres. *San Francisco: WH Freeman*, 1978.
- R. W. Milkey and D. Mihalas. Resonance line transfer with partial redistribution: II. The solar Mg II lines. *ApJ*, 192:769–776, September 1974. doi: 10.1086/153115.
- J. S. Morrill, K. P. Dere, and C. M. Korendyke. The Sources of Solar Ultraviolet Variability between 2765 and 2885 Å: Mg I, Mg II, Si I, and Continuum. *ApJ*, 557(2):854–863, August 2001. doi: 10.1086/321683.
- JS Morrill and CM Korendyke. High-resolution center-to-limb variation of the quiet solar spectrum near mg ii. *The Astrophysical Journal*, 687(1):646, 2008.
- D. I. Nagirner. Formation of Spectral Lines when There is Partial Frequency Redistribution. *Astrophysics*, 26(1):90–115, January 1987. doi: 10.1007/BF01005403.
- Susanna Parenti and Jean-Claude Vial. On the nature of the prominence - corona transition region. In Brigitte Schmieder, Jean-Marie Malherbe, and S. T. Wu, editors, *Nature of Prominences and their Role in Space Weather*, volume 300, pages 69–78, January 2014. doi: 10.1017/S1743921313010764.
- A. W. Peat, N. Labrosse, B. Schmieder, and K. Barczynski. Solar prominence diagnostics from non-LTE modelling of Mg II h&k line profiles. *A&A*, 653:A5, September 2021. doi: 10.1051/0004-6361/202140907.
- T. M. D. Pereira, J. Leenaarts, B. De Pontieu, M. Carlsson, and H. Uitenbroek. The Formation of IRIS Diagnostics. III. Near-ultraviolet Spectra and Images. *ApJ*, 778(2):143, December 2013. doi: 10.1088/0004-637X/778/2/143.
- Tiago M. D. Pereira, Mats Carlsson, Bart De Pontieu, and Viggo Hansteen. The Formation of IRIS Diagnostics. IV. The Mg II Triplet Lines as a New Diagnostic for Lower Chromospheric Heating. *ApJ*, 806(1):14, June 2015. doi: 10.1088/0004-637X/806/1/14.
- Tiago MD Pereira, Scott W McIntosh, Bart De Pontieu, Viggo Hansteen, Mats Carlsson, Paul Boerner, and Wei Liu. A users guide to iris data retrieval reduction & analysis. *LMSAL*, 2018.

- A. K. Pierce and C. D. Slaughter. Solar limb darkening. I: $\lambda\lambda$ (3033 - 7297). *Sol. Phys.*, 51(1):25–41, January 1977. doi: 10.1007/BF00240442.
- Amrita Prasad, Soumya Roy, Arindam Sarkar, Subhash Chandra Panja, and Sankar Narayan Patra. Prediction of solar cycle 25 using deep learning based long short-term memory forecasting technique. *Advances in Space Research*, 69(1):798–813, January 2022. doi: 10.1016/j.asr.2021.10.047.
- Eric Priest. *Magnetohydrodynamics of the Sun*. 2014. doi: 10.1017/CBO9781139020732.
- Guiping Ruan, Brigitte Schmieder, Pierre Mein, Nicole Mein, Nicolas Labrosse, Stanislav Gunár, and Yao Chen. On the Dynamic Nature of a Quiescent Prominence Observed by IRIS and MSDP Spectrographs. *ApJ*, 865(2):123, October 2018. doi: 10.3847/1538-4357/aada08.
- J. Sánchez Almeida. The Magnetism of the Very Quiet Sun. In T. Sakurai and T. Sekii, editors, *The Solar-B Mission and the Forefront of Solar Physics*, volume 325 of *Astronomical Society of the Pacific Conference Series*, page 115, December 2004. doi: 10.48550/arXiv.astro-ph/0404053.
- A. Savitzky and M. J. E. Golay. Smoothing and differentiation of data by simplified least squares procedures. *Analytical Chemistry*, 36:1627–1639, January 1964. doi: 10.1021/ac60214a047.
- Göran B. Scharmer, Boris V. Gudiksen, Dan Kiselman, Mats G. Löfdahl, and Luc H. M. Rouppe van der Voort. Dark cores in sunspot penumbral filaments. *Nature*, 420(6912):151–153, November 2002. doi: 10.1038/nature01173.
- Judith Schlagnitweit, Steven W Morgan, Martin Nausner, Norbert Müller, and Hervé Desvaux. Non-linear signal detection improvement by radiation damping in single-pulse nmr spectra. *ChemPhysChem*, 13(2):482–487, 2012.
- R. Schlichenmaier, K. Jahn, and H. U. Schmidt. Magnetic flux tubes evolving in sunspots. A model for the penumbral fine structure and the Evershed flow. *A&A*, 337:897–910, September 1998. doi: 10.48550/arXiv.astro-ph/9807036.
- B. Schmieder, G. Aulanier, and B. Vršnak. Flare-CME Models: An Observational Perspective (Invited Review). *Sol. Phys.*, 290(12):3457–3486, December 2015. doi: 10.1007/s11207-015-0712-1.
- D. Schmit, P. Bryans, B. De Pontieu, S. McIntosh, J. Leenaarts, and M. Carlsson. Observed Variability of the Solar Mg II h Spectral Line. *ApJ*, 811(2):127, October 2015. doi: 10.1088/0004-637X/811/2/127.
- M. Schwarzschild. On the scale of photospheric convection in red giants and supergiants. *ApJ*, 195:137–144, January 1975. doi: 10.1086/153313.

- Alexander I Shapiro, Hardi Peter, and Sami K Solanki. The sun's atmosphere. In *The Sun as a Guide to Stellar Physics*, pages 59–85. Elsevier, 2019.
- R. A. Shine and J. L. Linsky. Physical Properties of Solar Chromospheric Plages. II: Chromospheric Plage Models. *Sol. Phys.*, 39(1):49–77, November 1974. doi: 10.1007/BF00154970.
- Sami K. Solanki. Sunspots: An overview. *A&A Rev.*, 11(2-3):153–286, January 2003. doi: 10.1007/s00159-003-0018-4.
- A. K. Srivastava, J. L. Ballester, P. S. Cally, M. Carlsson, M. Goossens, D. B. Jess, E. Khomenko, M. Mathioudakis, K. Murawski, and T. V. Zaqarashvili. Chromospheric Heating by Magnetohydrodynamic Waves and Instabilities. *Journal of Geophysical Research (Space Physics)*, 126(6):e029097, June 2021. doi: 10.1029/2020JA029097.
- E. Staath and P. Lemaire. High resolution profiles of the MG II H and MG II K lines. *A&A*, 295:517–528, March 1995.
- K. T. Strong, A. O. Benz, B. R. Dennis, J. W. Leibacher, R. Mewe, A. I. Poland, J. Schrijver, G. Simnett, Jr. Smith, J. B., and J. Sylwester. A Multiwavelength Study of a Double Impulsive Flare. *Sol. Phys.*, 91(2):325–344, April 1984. doi: 10.1007/BF00146303.
- Andrii V. Sukhorukov and Jorrit Leenaarts. Partial redistribution in 3D non-LTE radiative transfer in solar-atmosphere models. *A&A*, 597:A46, January 2017. doi: 10.1051/0004-6361/201629086.
- E. Tandberg-Hanssen. Books-Received - the Nature of Solar Prominences. *Science*, 269:111, July 1995.
- John H. Thomas and Nigel O. Weiss. Fine Structure in Sunspots. *ARA&A*, 42(1):517–548, September 2004. doi: 10.1146/annurev.astro.42.010803.115226.
- W. T. Thompson and N. L. Reginald. The Radiometric and Pointing Calibration of SECCHI COR1 on STEREO. *Sol. Phys.*, 250(2):443–454, August 2008. doi: 10.1007/s11207-008-9228-2.
- H. Tian, E. E. DeLuca, S. R. Cranmer, B. De Pontieu, H. Peter, J. Martínez-Sykora, L. Golub, S. McKillop, K. K. Reeves, M. P. Miralles, P. McCauley, S. Saar, P. Testa, M. Weber, N. Murphy, J. Lemen, A. Title, P. Boerner, N. Hurlburt, T. D. Tarbell, J. P. Wuelser, L. Kleint, C. Kankelborg, S. Jaeggli, M. Carlsson, V. Hansteen, and S. W. McIntosh. Prevalence of small-scale jets from the networks of the solar transition region and chromosphere. *Science*, 346(6207):1255711, October 2014. doi: 10.1126/science.1255711.

- Javier Trujillo Bueno, Jiří Štěpán, and Roberto Casini. The Hanle Effect of the Hydrogen Ly α Line for Probing the Magnetism of the Solar Transition Region. *ApJ*, 738(1):L11, September 2011. doi: 10.1088/2041-8205/738/1/L11.
- H. Uitenbroek. THE SOLAR Mg II h AND k LINES - Observations and Radiative Transfer Modeling. *Sol. Phys.*, 172(1-2):109–116, May 1997. doi: 10.1023/A:1004981412889.
- H. Uitenbroek. Multilevel Radiative Transfer with Partial Frequency Redistribution. *ApJ*, 557(1):389–398, August 2001. doi: 10.1086/321659.
- Lidia van Driel-Gesztelyi and Lucie May Green. Evolution of Active Regions. *Living Reviews in Solar Physics*, 12(1):1, September 2015. doi: 10.1007/lrsp-2015-1.
- J. E. Vernazza, E. H. Avrett, and R. Loeser. Structure of the solar chromosphere. III. Models of the EUV brightness components of the quiet sun. *ApJS*, 45:635–725, April 1981. doi: 10.1086/190731.
- J-C Vial. The prominence-corona interface. In *Dynamics of Quiescent Prominences: Proceedings of the No. 117 Colloquium of the International Astronomical Union Hvar, SR Croatia, Yugoslavia 1989*, pages 106–119. Springer, 2005.
- Haimin Wang. On the Relationship Between Magnetic Fields and Supergranule Velocity Fields. *Sol. Phys.*, 117(2):343–358, September 1988. doi: 10.1007/BF00147252.
- David F. Webb and Timothy A. Howard. Coronal Mass Ejections: Observations. *Living Reviews in Solar Physics*, 9(1):3, June 2012. doi: 10.12942/lrsp-2012-3.
- Edward West, Jonathan Cirtain, Ken Kobayashi, John Davis, Allen Gary, and Mitzi Adams. MgII observations using the MSFC solar ultraviolet magnetograph. In Silvano Fineschi and Judy Fennelly, editors, *Solar Physics and Space Weather Instrumentation IV*, volume 8148 of *Society of Photo-Optical Instrumentation Engineers (SPIE) Conference Series*, page 81480F, October 2011. doi: 10.1117/12.894022.
- Thomas N. Woods, Francis G. Eparvier, Scott M. Bailey, Phillip C. Chamberlin, Judith Lean, Gary J. Rottman, Stanley C. Solomon, W. Kent Tobiska, and Donald L. Woodraska. Solar EUV Experiment (SEE): Mission overview and first results. *Journal of Geophysical Research (Space Physics)*, 110(A1):A01312, January 2005. doi: 10.1029/2004JA010765.
- J. P. Wülser, S. Jaeggli, B. De Pontieu, T. Tarbell, P. Boerner, S. Freeland, W. Liu, R. Timmons, S. Brannon, C. Kankelborg, C. Madsen, S. McKillop, J. Prchlik, S. Saar, N. Schanche, P. Testa, P. Bryans, and M. Wiesmann. Instrument Calibration of the Interface Region Imaging Spectrograph (IRIS) Mission. *Sol. Phys.*, 293(11):149, November 2018. doi: 10.1007/s11207-018-1364-8.

- G. P. Zank, L. L. Zhao, L. Adhikari, D. Telloni, J. C. Kasper, and S. D. Bale. Turbulence transport in the solar corona: Theory, modeling, and Parker Solar Probe. *Physics of Plasmas*, 28(8):080501, August 2021. doi: 10.1063/5.0055692.
- P. Zhang, É. Buchlin, and J. C. Vial. Launch of a CME-associated eruptive prominence as observed with IRIS and ancillary instruments. *A&A*, 624:A72, April 2019. doi: 10.1051/0004-6361/201834259.
- H. Zirin. Evolution of weak solar magnetic fields. *Australian Journal of Physics*, 38:961–969, January 1985. doi: 10.1071/PH850961.
- H. Zirin. Book-Review - Astrophysics of the Sun. *Science*, 242:1586, December 1988.